The population of X-ray supernova remnants in the Large Magellanic Cloud

P. Maggi, F. Haberl, P. J. Kavanagh, M. Sasaki, L. M. Bozzetto, M. D. Filipović, G. Vasilopoulos, W. Pietsch, S. D. Points, Y.-H. Chu, et al.

A&A 585, A162 (2016)
DOI: 10.1051/0004-6361/201526932

Astronomy & Astrophysics

The population of X-ray supernova remnants in the Large Magellanic Cloud⋆

P. Maggi[1,2], F. Haberl[1], P. J. Kavanagh[3], M. Sasaki[3], L. M. Bozzetto[4], M. D. Filipović[4], G. Vasilopoulos[1], W. Pietsch[1], S. D. Points[5], Y.-H. Chu[6], J. Dickel[7], M. Ehle[8], R. Williams[9], and J. Greiner[1]

[1] Max-Planck-Institut für extraterrestrische Physik, Postfach 1312, Giessenbachstr., 85741 Garching, Germany
e-mail: pierre.maggi@cea.fr
[2] Laboratoire AIM, CEA-IRFU/CNRS/Université Paris Diderot, Service d'Astrophysique, CEA Saclay, 91191 Gif-sur-Yvette, France
[3] Institut für Astronomie und Astrophysik Tübingen, Universität Tübingen, Sand 1, 72076 Tübingen, Germany
[4] University of Western Sydney, Locked Bag 1797, Penrith South DC, NSW 1797, Australia
[5] Cerro Tololo Inter-American Observatory, National Optical Astronomy Observatory, Cassilla 603 La Serena, Chile
[6] Institute of Astronomy and Astrophysics, Academia Sinica, No.1, Sec. 4, Roosevelt Rd, 10617 Taipei, Taiwan, Republic of China
[7] Physics and Astronomy Department, University of New Mexico, MSC 07-4220, Albuquerque, NM 87131, USA
[8] *XMM-Newton* Science Operations Centre, ESA/ESAC, PO Box 78, 28691 Villanueva de la Cañada, Madrid, Spain
[9] Columbus State University Coca-Cola Space Science Center, 701 Front Avenue, Colombus, GA 31901, USA

Received 10 July 2015 / Accepted 28 September 2015

ABSTRACT

Aims. We present a comprehensive X-ray study of the population of supernova remnants (SNRs) in the Large Magellanic Cloud (LMC). Using primarily *XMM-Newton* observations, we conduct a systematic spectral analysis of LMC SNRs to gain new insight into their evolution and the interplay with their host galaxy.

Methods. We combined all the archival *XMM-Newton* observations of the LMC with those of our Very Large Programme LMC survey. We produced X-ray images and spectra of 51 SNRs, out of a list of 59 objects compiled from the literature and augmented with newly found objects. Using a careful modelling of the background, we consistently analysed all the X-ray spectra and measure temperatures, luminosities, and chemical compositions. The locations of SNRs are compared to the distributions of stars, cold gas, and warm gas in the LMC, and we investigated the connection between the SNRs and their local environment, characterised by various star formation histories. We tentatively typed all LMC SNRs, in order to constrain the ratio of core-collapse to type Ia SN rates in the LMC. We also compared the column densities derived from X-ray spectra to H I maps, thus probing the three-dimensional structure of the LMC.

Results. This work provides the first homogeneous catalogue of the X-ray spectral properties of SNRs in the LMC. It offers a complete census of LMC remnants whose X-ray emission exhibits Fe K lines (13% of the sample), or reveals the contribution from hot supernova ejecta (39%), which both give clues to the progenitor types. The abundances of O, Ne, Mg, Si, and Fe in the hot phase of the LMC interstellar medium are found to be between 0.2 and 0.5 times the solar values with a lower abundance ratio [α/Fe] than in the Milky Way. The current ratio of core-collapse to type Ia SN rates in the LMC is constrained to $N_{\rm CC}/N_{\rm Ia} = 1.35(^{+0.11}_{-0.24})$, which is lower than in local SN surveys and galaxy clusters. Our comparison of the X-ray luminosity functions of SNRs in Local Group galaxies (LMC, SMC, M31, and M33) reveals an intriguing excess of bright objects in the LMC. Finally, we confirm that 30 Doradus and the LMC Bar are offset from the main disc of the LMC to the far and near sides, respectively.

Key words. ISM: supernova remnants – Magellanic Clouds – ISM: abundances – supernovae: general – stars: formation – X-rays: ISM

1. Introduction

Supernova remnants (SNRs) are the imprints of stars that died in supernova (SN) explosions on the interstellar medium (ISM). SNRs return nucleosynthesis products to the ISM, enriching and mixing it with freshly produced heavy elements. A core-collapse (CC) SN is the explosion of a massive star, and it produces large quantities of α-group elements (e.g. O, Ne, Mg, Si, S). Thermonuclear (or type Ia) SNe mark the disruption of a carbon-oxygen white dwarf (WD) that reached the Chandrasekhar limit, although recent models suggest that sub-Chandrasekhar WDs may also explode as type Ia SNe (Sim et al. 2010; van Kerkwijk et al. 2010; Woosley & Kasen 2011). The thermonuclear burning front in a type Ia SN incinerates most of the progenitor to Fe-group elements. Despite the essential role of type Ia SNe in cosmology as standard candles, leading to the discovery that the expansion of the Universe is accelerating (Riess et al. 1998; Perlmutter et al. 1999), the exact nature of the progenitor system as either a white dwarf accreting from a companion or a merger of two white dwarves is still hotly debated (see Maoz & Mannucci 2012, for a review).

SNe of either type instantaneously release a tremendous amount of kinetic energy ($\sim 10^{51}$ erg) in the ISM and consequently have a profound and long-lasting impact on their surrounding environment. SN ejecta are launched to velocities in

⋆ Based on observations obtained with *XMM-Newton*, an ESA science mission with instruments and contributions directly funded by ESA Member States and NASA.

excess of 10^4 km s^{-1}, producing shock waves that heat the ISM and ejecta up to X-ray emitting temperatures ($>10^6$ K). SNe are the main source of energy for the ISM, in the form of kinetic energy and turbulence (e.g. Mac Low & Klessen 2004, and references therein) or in the form of cosmic rays that are accelerated at SNR shock fronts.

X-ray observations are a powerful tool for studying SNRs (see e.g. the review of Vink 2012). While some SNRs exhibit non-thermal X-ray emission, originating in synchrotron-emitting electrons accelerated up to 100 TeV (see Koyama et al. 1995; Rho et al. 2002; Bamba et al. 2005, and references therein), most X-ray emitting SNRs have thermal spectra dominated by highly ionised species of C, N, O, Ne, Mg, Si, S, and Fe. At the typical electron temperatures of SNR shocks ($kT \sim 0.2$–5 keV), all these astrophysically abundant elements have emission lines in the range accessible to X-ray space observatories. Thus, the thermal X-ray spectrum of an SNR encrypts precious information about the temperature, ionisation state, and chemical composition of the hot plasma (Slane 2014). This, in turn, provides clues to the evolutionary state of the remnant, ambient density (of the inter- or circum-stellar medium), age, explosion energy, and the type of supernova progenitor. The distribution of these parameters, the impact of the environment on them, and their interrelations (e.g. temperature vs. size/age, luminosity vs. ambient density) are valuable information to understand the evolution of SNRs and their role in the hydrodynamical and chemical evolution of galaxies.

Furthermore, SNRs are observable for a few tens of thousands of years. Thus, even though SNe are rare events in a galaxy (typically one per century or less), there will be tens or hundreds of SNRs for us to access. In our own Galaxy, the Milky Way (MW), 294 SNRs are known (Green 2014). However, studies of Galactic SNRs are plagued by the large distance uncertainties towards sources in the Galactic plane. In addition, many important X-ray lines of O, Ne, Mg, and Fe are emitted at energies $kT < 2$ keV and are readily absorbed by the high column densities in front of Galactic sources.

On the other hand, the Large Magellanic Cloud (LMC), our closest neighbour galaxy, offers an ideal laboratory for such (X-ray) studies: First, the distance towards the LMC is relatively small (50 kpc, Pietrzyński et al. 2013) and very well studied (de Grijs et al. 2014). Second, the moderate inclination angle (between 25° and 40°, e.g. van der Marel & Kallivayalil 2014) and the small line-of-sight depth of the LMC (between 0.3 kpc and 1.5 kpc, van der Marel et al. 2002) mean that we can assume all LMC sources to be at a very similar distance. Third, the interstellar absorption by gas in the foreground is much smaller towards the LMC ($N_{\rm H} < 10^{21}$ cm^{-2}) than towards the Galactic plane ($N_{\rm H} > 10^{22}$ cm^{-2}), allowing detection of photons even in the soft X-ray regime, below 1 keV. Finally, a wealth of data is available for the LMC, allowing for easier detection and multi-wavelength analysis of SNRs. For all these reasons, we aim to discover and study the *complete* sample of SNRs in the LMC.

While several studies exist analysing the sample of LMC remnants as a whole (see references in Sect. 3.1), they focus either on surveys with a particular instrument (at a particular wavelength, e.g. infrared or ultraviolet), or on some specific aspects (e.g. the size distribution of SNRs). In X-rays, Long et al. (1981) used the *Einstein* survey of the LMC to detect 26 SNRs. Later, Williams et al. (1999a) compiled a list of 37 SNRs, amongst which they studied the X-ray morphology of 31 objects with ROSAT. Since 2000, more than twenty new remnants were discovered or confirmed, primarily through *XMM-Newton* observations. However, the X-ray spectral analyses of LMC SNRs were presented in a wide collection of individual papers with little consistency in the instruments, spectral models, and analysis methods used. Furthermore, several known SNRs were observed for the first time with modern X-ray instrumentation during our *XMM-Newton* LMC survey (see Sect. 2.1) and their spectral properties are as yet unpublished (see Sect. 5.1 and Appendix D). Because of these limitations, it is not feasible to study the spectral properties of the whole population of LMC remnants with a mere survey of the available literature.

The main ambition of this work is to alleviate these limitations and provide for the first time an up-to-date study of the X-ray emission of LMC SNRs, using primarily *XMM-Newton* observations. To that end, we performed a systematic and homogeneous X-ray spectral analysis of *all* LMC SNRs for which *XMM-Newton* data are available. This allows meaningful comparisons of remnants at various evolutionary stages, and provides a complete census of various spectral features, such as Fe K or SN ejecta emission. In turn, SNRs are used as probes of their surroundings, thanks to which one can derive the chemical abundances in the hot phase of the LMC ISM, and compare those to abundances measured in older populations (globular clusters and red giant stars).

In addition, we take advantage of the availability of star formation history (SFH) maps of the LMC, based on spatially resolved stellar photometry, to investigate the connection between LMC SNRs and their local environment, characterised by different SFHs. Doing so, we devise a method to tentatively type all LMC SNRs, which can then be used to retrieve the ratio of core-collapse to type Ia SN rates in the LMC. Then, via their X-ray luminosity function, we compare SNR populations in galaxies of the Local Group (M31, M33, LMC, SMC), which have different metallicities and SFHs. Finally, we study the spatial distribution of SNRs in the LMC with respect to cool gas, star-forming regions, and stars.

This work is organised as follows: We start in Sect. 2 by presenting the X-ray observations and their processing, along with supplementary data. In Sect. 3, we compile a complete, clean sample of LMC SNRs which is used throughout the rest of the paper. The details of our data analysis methods are given in Sect. 4. The following Sections present the results of the systematic spectral analysis of LMC SNRs (Sect. 5), the SNR typing and measurement of the ratio of core-collapse to type Ia SN rates (Sect. 6), the comparative study of the X-ray luminosity functions of Local Group SNRs (Sect. 7), and the spatial distribution of SNRs in the LMC (Sect. 8). Finally, we summarise our findings and offer our conclusions in Sect. 9.

2. Observations and data reduction

2.1. XMM-Newton observations of the LMC

The *XMM-Newton* space observatory (Jansen et al. 2001; Lumb et al. 2012) was placed in a 48 h highly eccentric orbit by an Ariane-V on 1999 December 10. It carries three identical X-ray telescopes, each consisting of 58 gold-coated nested Wolter-I mirrors with a focal length of 7.5 m. Three CCD imaging cameras are placed at the focal points of each telescope. Two of them have Metal Oxide Semi-conductor (MOS) CCD arrays (Turner et al. 2001) and the third uses pn-CCDs (Strüder et al. 2001). Together, they form the European Photon Imaging Camera (EPIC). Other instruments are the two Reflection Grating Spectrometers (RGS, den Herder et al. 2001) for high-resolution spectroscopy of bright on-axis point sources, and the optical monitor (OM, Mason et al. 2001), a 30 cm

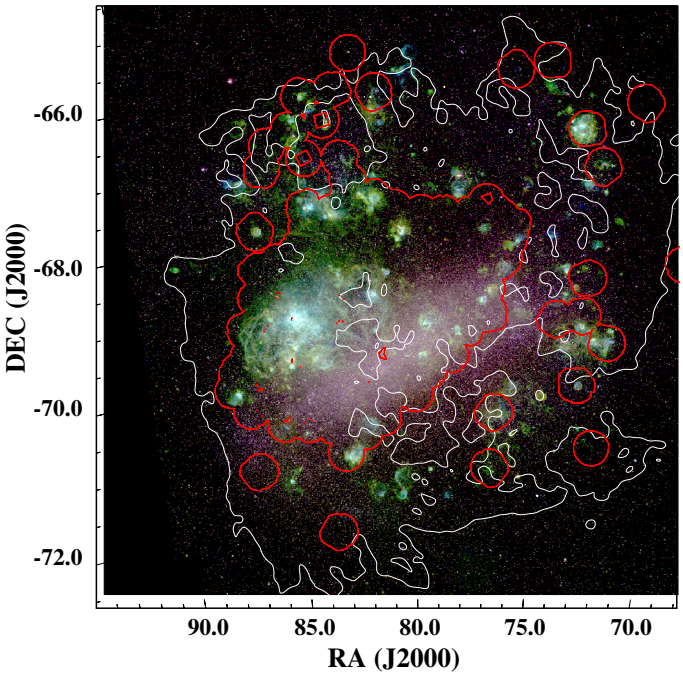

Fig. 1. The LMC in the light of [S II] (red), Hα (green), and [O III] (blue), all data from MCELS (see Sect. 2.3). The red contours delineates the coverage of the LMC with *XMM-Newton*, combining archival data and observations of our large survey (see Sect. 2.1). The white contours outline a LMC H I column density of 1×10^{21} cm^{-2} (data from Kim et al. 2003).

Ritchey-Chrétien telescope observing simultaneously the central field of view in optical and ultraviolet light. However, data from RGS and OM were not used in this work.

About 200 *XMM-Newton* observations of the LMC were performed since the "first light" image of the observatory, of the 30 Doradus region (Dennerl et al. 2001). In most cases, one specific object is placed at the focus of the telescopes (regular or "target of opportunity" observations). Some fields were observed several times, yielding very deep exposures. For instance, the SNR N132D is used as a calibration source and regularly observed; also SN 1987A is frequently monitored (Heng et al. 2008; Maggi et al. 2012b). In these two regions, the combined exposure reaches 10^6 s. We have also carried out dedicated *XMM-Newton* observations of SNR candidates found in ROSAT, radio, and optical data (Grondin et al. 2012; Bozzetto et al. 2014; Kavanagh et al. 2015b).

Other programmes are raster surveys: the most ambitious such project was the survey of the LMC, proposed as a Very Large Programme (VLP) for *XMM-Newton* (PI: Frank Haberl). The survey comprises 70 pointings chosen to fill the gaps between all existing observations. This provides a contiguous field in the central region of the LMC, a strategy similar to the *XMM-Newton* survey of the SMC (Haberl et al. 2012b; Sturm 2012; Sturm et al. 2013). The LMC coverage with *XMM-Newton*, including both the 70 observations of that survey *and* the archival data, is shown in Fig. 1 on an optical image of the galaxy. Because the LMC is closer and has a larger extent on the sky than the SMC, all the observations combined still cover less than half of the total extent of the galaxy.

2.2. Data reduction

The processing of all available *XMM-Newton* data in the LMC region, and those of the VLP survey in particular, was done with the data reduction pipeline developed in our research group over several years. This pipeline was already used for the surveys of M31 (Pietsch et al. 2005; Stiele et al. 2011) and M33 (Pietsch et al. 2004; Misanovic et al. 2006). It was then enhanced for the analysis of the SMC survey by Richard Sturm (2012). The data reduction pipeline is similar in essence to that used for the *XMM-Newton* Serendipitous Source Catalogue (Watson et al. 2009), with the advantage of a better spatial accuracy (thanks to astrometric boresight corrections), and dedicated source screenings and cross-identifications. It is a collection of tasks from the *XMM-Newton* Science Analysis Software[1], organised in `bash` scripts, together with other tools, in particular the FITS-file manipulation tasks of the `FTOOLS` package[2] (Blackburn 1995). We summarise below the important steps of the pipeline.

Preparing the data: to point to the Current Calibration Files (CCFs) corresponding to each observation, a CCF index file (CIF) is created with the SAS task `cifbuild`. Then, using the task `odfingest`, the ODF summary file is extended with data extracted from the instrument housekeeping datasets. The instrument mode is also determined based on the CIF.

Creating event lists: the meta-tasks `epchain` and `emchain` produce EPIC-pn and MOS event lists, respectively. Raw events are first extracted from each exposure and CCD chip. Bad pixels are flagged. In the case of EPIC-pn, the task `eproject` corrects shifts in the energy scale of some pixels induced by high-energy particles hitting the detector while the offset map is calculated. Raw events are then assigned pattern and detector position information. EPIC-pn events are corrected for gain variation and charge transfer inefficiency (CTI). The calibrated events are (tangentially) projected on the sky using the task `attcalc` and an attitude history file (AHF), which records the attitude of the spacecraft during the observation. The AHF is created by the task `atthkgen` that is automatically ran before the main chain (unless the AHF already exists). EPIC-pn event times are randomised within their read-out frame. Finally, event lists from all CCDs are merged in the final list by `evlistcomb`.

Time filtering: times that are useful for analysis are known as good time intervals (GTIs). In particular, periods of high background must be filtered out. The pipeline identifies the background-GTIs as times when the count rate in the (7−15) keV band is below a threshold of 8×10^{-3} cts s^{-1} arcmin^{-2} and 2.5×10^{-3} cts s^{-1} arcmin^{-2} for EPIC-pn and EPIC-MOS, respectively. Soft proton flares affect all detectors, so only the GTIs *common* to pn and MOS are used. When one instrument starts earlier or observes longer, this interval is added to the GTIs. For instance, EPIC-pn calculates an offset map before an exposure. Thus, pn exposures usually start later than those of MOS, but these times should not be vetoed, unless the background in MOS is above the threshold.

Images creation: the pipeline then produces images from the calibrated, cleaned, and background-filtered event lists. The

[1] SAS, `http://xmm.esac.esa.int/sas/`
[2] `http://heasarc.gsfc.nasa.gov/ftools/`

image pixels have a size of 2″ × 2″. All single to quadruple-pixel (PATTERN = 0 to 12) events with FLAG = 0 from the MOS detectors are used. From the pn detector single and double-pixel events (PATTERN = 0 to 4) with (FLAG && 0xf0000) = 0 (including events next to bad pixels or bad columns) are used. Below 500 eV, only single-pixel events are selected to avoid the higher detector noise contribution from the double-pixel events. Exposure maps taking into account the telescope vignetting (which is energy-dependent) are created with the task eexpmap. Images and exposure maps are extracted in various energy bands for all three cameras. Out-of-time (OoT) images are created from the EPIC-pn OoT event lists, scaled by the corresponding OoT fraction $f_{\rm OoT}$[3], and subtracted from the source+background images. MOS and pn images are then merged, smoothed with a 10″ full width at half maximum (FWHM) Gaussian kernel, and finally divided by the vignetted exposure maps.

Detector-background images are also created, by using *XMM-Newton* filter wheel closed (hereafter FWC) data, obtained with the detectors shielded from astrophysical and soft-proton backgrounds by a 1.05 mm-thick aluminium filter. FWC data are collected several times per year, and the merged event lists of these observations are made available by the *XMM-Newton* Science Operations Centre[4]. The detector corners are always shielded from the X-ray telescopes, and the count rate in the corners is used to estimate the contribution of the instrumental background $f_{\rm FWC}$ to the science image. The FWC image is scaled by $f_{\rm FWC}$ and removed from the science image to create the background-subtracted image.

Source detection: X-ray source detection is performed simultaneously using source+background images in all available energy bands of all three instruments with the SAS meta-task edetectchain. Although this work is concerned with SNRs, i.e. extended sources, detecting point sources is highly desirable: it allows us to excise unrelated point sources from spectral extraction regions and to look for central compact objects or pulsar wind nebulae inside SNRs.

Fine-tuning for SNRs: several scripts for the analysis of the LMC SNRs were produced. For imaging purposes, all observations of an SNR are combined to produce an image centred on the source. The smoothing of the images (using the SAS task asmooth) is performed both in constant and adaptive mode. In the latter, the task calculates a library of Gaussian kernels such that the resulting images reached a minimum (Poissonian) signal-to-noise ratio of 5 everywhere. Regions of good statistics (e.g. bright sources) will be smoothed with a 10″ FWHM kernel (the chosen minimum value), whereas fainter regions (diffuse emission, rims of the field of view) will be smoothed with wider kernels. The (minimum) kernel size for (adaptive) smoothing was chosen depending on the available data and brightness of the SNR under investigation. Moderately bright and faint SNRs (i.e. most of the sample) have smoothing kernel sizes of $\gtrsim$10″ or $\gtrsim$20″. The bright objects and SNRs in very deep fields (e.g. the field around SNR 1987A) only need shallow smoothing (kernels $\gtrsim$3″ or $\gtrsim$6″).

Images were produced in a set of energy bands tailored to the thermal spectrum of SNRs: A soft band from 0.3 keV to 0.7 keV includes strong lines from oxygen; a medium band from 0.7 keV to 1.1 keV comprises Fe L-shell lines as well as Lyα lines from Ne IX and Ne X; and a hard band (1.1−4.2 keV) which includes lines from Mg, Si, S, Ca, Ar, and possibly non-thermal continuum. Thus, the composite images of SNRs provide a visual evaluation of their temperature: evolved objects with a relatively cool plasma (0.2 keV $\lesssim kT \lesssim$ 0.4 keV) are most prominent in the soft band, those with higher temperatures (0.4 keV $\lesssim kT \lesssim$ 1 keV) in the medium band. Only (young) SNRs with a much hotter component or a non-thermal continuum will have significant emission in the hard band as well.

2.3. Supplementary data

Various non-X-ray data were used to supplement the *XMM-Newton* observations. They allow us to assess e.g. the relation between the population of SNRs and large scale structure of the LMC (Sect. 8), or to evaluate doubtful candidates in the sample compilation (Sect. 3). Here, we present those data briefly.

Optical data: the Magellanic Clouds Emission Line Survey (MCELS, e.g. Smith et al. 2000) was carried out at the Cerro Tololo Inter-American Observatory (CTIO). It is a spatially complete, flux-limited survey with the 0.6/0.9 m Curtis Schmidt telescope of the University of Michigan. A 8° × 8° region centred on the LMC was imaged with three narrow-band filters [S II]$\lambda\lambda$6716, 6731 Å, Hα[5], and [O III]λ5007 Å. Observations with green and red broad-band filters centred at 5130 Å and 6850 Å were obtained to subtract stellar continua. The pixel size of the mosaicked data is 2″ × 2″.

For optical photometry, we used results of the Magellanic Clouds Photometric Survey (MCPS, Zaritsky et al. 2004), a *UBVI* survey of 24 million stars in the central ∼64 deg^2 of the LMC down to $V \sim$ 20−21 mag (depending on crowding). Additionally, we used optical images (red continuum and Hα) from the Southern H-Alpha Sky Survey Atlas (SHASSA Gaustad et al. 2001).

Radio: the neutral hydrogen (H I) content and structure of the LMC has been studied (at 21 cm) by Staveley-Smith et al. (2003) and Kim et al. (2003). The former used data from the 64-m single-dish Parkes radio-telescope, sensitive to large-scale structures (200 pc to 10 kpc). They show the distribution of H I in a well-defined disc and three "arms" interpreted as tidal features. Several H I holes (the largest ones) are associated to supergiant shells (SGS). In Kim et al. (2003), the Parkes data are merged with data from the Australia Telescope Compact Array (ATCA) interferometer, which provides a view of the smaller structures (15 pc to 500 pc). The resulting map (which we used in this work) reveal the clumpiness of the H I distribution, or in their words, "the filamentary, bubbly, and flocculent structures of the ISM in the LMC". Finally, the molecular content of the LMC is assessed by the ∼30 deg^2 survey with the NANTEN telescope in the ^{12}CO (J = 1−0) line (Fukui et al. 2008), from which we borrowed the velocity-integrated CO map.

Star formation history map of the LMC: the first studies of the LMC's stellar content in the 1960s suggested a different SFH than for the Milky Way (Hodge 1960, 1961). Most of the early studies used age-dating of LMC clusters. The most striking

[3] Values taken from the *XMM-Newton* Users Handbook.

[4] http://xmm2.esac.esa.int/external/xmm_sw_cal/background/filter_closed/

[5] The Hα filter included the [N II]$\lambda\lambda$6548, 6584 Å doublet in its bandpass.

feature they revealed was the "Age Gap", i.e. the lack of clusters between ages of ∼5 Gyr and ∼12 Gyr (e.g. Da Costa 1991). Studies of *field star* populations (e.g. with HST, Holtzman et al. 1999; Smecker-Hane et al. 2002) reveal essentially the same results, i.e. a dearth of star formation between an initial burst (≳12 Gyr) and a second episode 4−5 Gyr ago.

The first truly global analysis of the LMC's SFH was conducted by Harris & Zaritsky (2009). They used the results from the MCPS to perform colour–magnitude diagram fitting. They obtained a reconstruction of the star formation rate (SFR, in $M_\odot$ yr^{-1}) in 13 time bins and four metallicity bins, for 1380 cells, most of them having a size of $12' \times 12'$. Although poorly sensitive to old ages because the survey does not reach the main-sequence turn-off (MSTO) in the crowded fields[6], the SFH obtained is extremely useful to study the recent and intermediate-age star formation episodes, and to compare the integrated SFH of small- and medium-scale regions. We used the SFH map to compare the local stellar populations around LMC SNRs in Sect. 6.

3. Compiling a complete sample of LMC SNRs

Obtaining a complete and clean census of LMC remnants is a complex task, for several reasons:

- *Classification*: different authors may use different criteria to classify an object as a definite SNR.
- *Literature size*: with the exception of the early studies, the discovery of most new objects was reported in separate papers, building up a vast literature.
- *Nomenclature*: an additional problem related to the previous point is the inconsistencies in the naming convention for LMC SNRs. The common names of many remnants used in the literature, especially those discovered first, are an unruly collection of various surveys and catalogues in specific wavelengths. Some are referred to after the H II complex within which they are located (e.g. "SNR in N44"), or worse, a nearby H II region (e.g. DEM L109, though it is most likely unrelated to the remnant). Other names use B1950 coordinates, with little to no consistency in the coordinates convention. Consequently, some objects were mistakenly listed twice in SNR compilations (Sect. 3.2).

To bypass these shortcomings, we performed a complete literature survey to build a list of LMC SNRs, combining all papers that either i) report the discovery or classification of one or more SNRs; ii) give a list of LMC SNRs; or iii) present new candidates (Sect. 3.1). The list is then cleaned from the wrongly identified or misclassified objects (Sect. 3.2). Unconfirmed candidates, particularly in light of new X-ray observations, are also removed. For the naming of all SNRs in the Magellanic Clouds, we made use of the acronym "MCSNR", which was pre-registered to the International Astronomical Union by R. Williams et al., who maintain the Magellanic Cloud Supernova Remnants online database[7]. This ensures a consistent and general naming system. Therefore, all SNRs are assigned the identifier "MCSNR JHHMM+DDMM", although we also retained the old "common names" from the literature for easy cross-identifications.

3.1. Literature survey

The first extragalactic supernova remnants were found in the LMC in the 1960s. Combining Parkes observations with Hα photographs, Mathewson et al. (1963) first identified N49 as an SNR, to which Westerlund & Mathewson (1966) soon added N63A and N132D. Less than ten years later, Mathewson & Clarke (1973), using the same method, had already discovered 12 new SNRs[8]. The survey with *Einstein* allowed Long et al. (1981) to list 26 SNRs detected in X-rays, confirming many previously suggested candidates (based on optical or radio data). Mathewson et al. (1983) provided a catalogue of 25 SNRs with radio, optical, and X-ray results. With more observations, Mills et al. (1984) and Mathewson et al. (1984, 1985) increased the size of the sample to 32.

In the 1990s, several new SNRs were discovered with ROSAT pointed observations (Chu et al. 1993, 2000; Smith et al. 1994), sometimes aided by optical spectroscopy (Chu et al. 1995, 1997). Since then, about twenty new remnants were discovered or confirmed in a collection of papers. Some discoveries stemmed from new radio observations (e.g. Bozzetto et al. 2012a,b; de Horta et al. 2012). The majority, though, used *XMM-Newton* observations, either optically selected candidates (Klimek et al. 2010), ROSAT-selected candidates (Grondin et al. 2012; Bozzetto et al. 2014, Kavanagh et al., in prep.), or serendipitously observed during the LMC VLP survey (Maggi et al. 2012a, 2014) or other programmes (Warth et al. 2014).

Several groups compiled lists of SNRs in the (Large) Magellanic Cloud(s), the purpose being to analyse some of their global properties. Filipovic et al. (1998) used Parkes surveys to study the radio spectral index and luminosityy distribution of 34 confirmed and 24 probable LMC SNRs. Williams et al. (1999a) were the first to study the X-ray morphology of all known LMC SNRs at that time. They showed ROSAT images for 31 out of their list of 37 SNRs. Blair et al. (2006, hereafter BGS06) compiled a sample of 39 SNRs in the LMC which was observed with the Far Ultraviolet Spectroscopic Explorer (FUSE) satellite. The goal was to study UV emission from SNRs, in particular in the light of highly ionised oxygen (O VI λ1032). A sample of 52 confirmed and 20 candidate radio-selected SNRs was observed spectroscopically in Payne et al. (2008), but the exact list was not given. Instead, they reported the results for the 25 objects which were detected. Desai et al. (2010) studied the triggering of star formation by SNRs. To that end, they examined the young stellar objects and molecular clouds associated to LMC SNRs. Their census resulted in a list of 45 objects. A total of 54 SNRs was used by Badenes et al. (2010, hereafter BMD10) to study their size distribution. The difference in numbers stems from their including objects from unpublished sources (i.e. online catalogues). Seok et al. (2008, 2013) combined AKARI and *Spitzer* observatories to survey the infrared emission of LMC SNRs. They presented a list of 47 SNRs, warning that some sources in BMD10 still needed confirmation.

3.2. Cleaning the sample: objects not included

To build the final list of LMC SNRs, we combined objects from the older catalogues (Mathewson & Clarke 1973; Long et al. 1981; Mathewson et al. 1983, 1984, 1985) with those reported in individual studies since then. We also included all sources present in the various compilations described in the previous

[6] In the Bar the old (≳4 Gyr) SFH is constrained to match that obtained with HST.

[7] MCSNR, http://www.mcsnr.org/Default.aspx

[8] Counting the two distinct shells they identified in N135 (the remnants to be known as DEM L316A and DEM L316B) and including the two objects in the 30 Doradus region that they identified as candidates.

Section. After removing all multiple occurrences of the same object, we "cleaned" the sample, searching for:

- *Misclassification*: the object is something else than an SNR, e.g. a superbubble. The X-ray properties of non-SNR extended sources that can be found in the field of the LMC were described in Maggi et al. (2014).
- *Unconfirmed candidates:* new data obtained since the classification as an SNR/candidate argue against this interpretation. This includes mainly candidates observed with *XMM-Newton* for the first time in our VLP survey. The absence of coincident X-ray emission strongly disfavours an SNR nature, unless radio and optical emission typical of SNRs is found.
- *Misidentification:* spurious source due to confusion (of the coordinates or nomenclature) in the literature.

Below, we describe the objects erroneously classified as SNRs or candidates and the evidence motivating the decision. These objects are listed in Table 1 and were not included in our final sample.

[BGS2006b] J0449−693: this object was observed in the UV by Blair et al. (2006) and in optical by Payne et al. (2008), although the latter used a different location, further to the south-east than the former. None of these studies gave conclusive evidence of an SNR nature (no UV lines detected, moderate [S II]/Hα ratio). Klimek et al. (2010) used MCELS and *XMM-Newton* to identify the true SNR in that region, that they named SNR0449−6921, now registered as [BMD2010] SNR J0449.3−6920 in Simbad. The X-ray emission originates from an optical shell clearly distinct from the position given for [BGS2006b] J0449−693. In BMD10, both sources are listed, although only [BMD2010] SNR J0449.3−6920 (SNR0449−6921) is the true source. This is an example of a misidentification due to coordinate confusion.

LHA 120−N 185: Blair et al. (2006) could not detect UV emission from this source (that they incorrectly listed as SNR 0453-672). It was not included in the compilations from Desai et al. (2010) and Seok et al. (2013). Only BMD10 classified the source as an SNR. X-ray emission is detected, surrounded by the large, bright optical shell N 185. However, the nature of the source remains uncertain. Most likely, N 185 is actually a superbubble, and not the remnant of a single supernova (Zhang et al. 2014; Reyes-Iturbide et al. 2014).

SNR J051327−691119: this source is located north-westwards of SNR B0513−692 (which has the name MCSNR J0513−6912 in our list). Bojičić et al. (2007) present the optical and radio observations of this region, identifying the large (4.1′ × 3.3′) shell of MCSNR J0513−6912. They detected a strong unresolved radio source at its north-western edge, that they classified as an unrelated H II region or background galaxy (GH 6−2, see references in Bojičić et al. 2007).

In addition, they observed a faint optical shell seen in both MCELS [S II] and AAO/UKST deep Hα images. Follow-up optical spectroscopy revealed distinct, higher [S II]/Hα ratios from this faint shell, prompting (Bojičić et al. 2007) to classify this shell as a new candidate SNR, J051327−691119. This region was covered by the *XMM-Newton* survey, revealing in details the X-ray emission of MCSNR J0513−6912 (Sect. 5, Appendix D & F). On the other hand, the candidate J051327−691119 lacks any X-ray feature. The small extent of the source (40″ diameter in Hα) would suggest a young, X-ray bright SNR, easily detectable in observations of the *XMM-Newton* survey. With only weak optical evidence, a confused field in the radio, and a stringent non-detection in X-rays, one is forced to conclude that J051327−691119 is *not* an SNR.

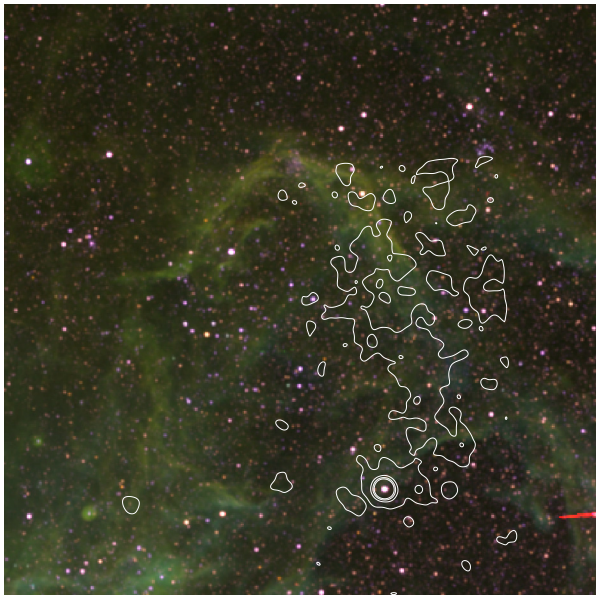

Fig. 2. The rejected SNR candidate in DEM L203 in optical lines ([S II] (red), Hα (green), and [O III] (blue), data from MCELS), with soft X-ray contours (from *XMM-Newton*) overlaid in white. The image spans 20′ across. The bright star seen in X-rays (lower right corner) is the Galactic star HD 269602.

LHA 120−N 204: it is only listed as an SNR in the compilation of BMD10. It was selected from the radio observations of Payne et al. (2008) where it appeared for the first time in the literature. Therefore, it was selected from radio catalogues. The "SNR" lies within the large (diameter of 14′) optical shell N 204, although a size of 1′ was given in Payne et al. (2008). The field 61 of the *XMM-Newton* survey covered this region, detecting no extended X-ray emission. With the small size of this source, bright emission is expected. Instead, an X-ray point source is detected in projection in N 204, which correlates with a mid-IR selected AGN (MQS J052749.08−703641.7, Kozłowski et al. 2012). The background AGN is most likely the origin of the radio emission which led to the misclassification of the target as an SNR candidate.

[BMD2010] SNR J0529.1−6833: the classification as an SNR candidate (in the MCSNR online database) stems from the detection of radio emission correlating with the large optical shell DEM L203. This object is however in the compilation of "confirmed" SNRs of BMD10. Again, X-ray observations can shed light on the nature of the source. DEM L203 has no X-ray counterpart in the ROSAT catalogue. More importantly, *XMM-Newton* covered the object on three occasions during the LMC survey. Combining ∼35 ks of EPIC data, only unrelated large-scale diffuse emission is detected, without any correlation with the optical shell, as shown in Fig. 2. A very old age, as indicated by the large extent, might explain the lack of X-ray emission, although *XMM-Newton* can and did detect the largest

Table 1. LMC objects erroneously classified as SNRs or candidates, not included in the final sample.

Name	Alternative name	Category	Ref. code
[BGS2006b] J0449−693	B0450−6927	Wrong identification	BGS06
LHA 120−N 185	N185	Wrong classification (superbubble)	PWF08
SNR J051327−691119	DEM L109	Unconfirmed candidate	BFP07
LHA 120−N 204	B0528−7038	Wrong identification	PWF08
[BMD2010] SNR J0529.1−6833	DEM L203	Unconfirmed candidate	BMD10
RX J0533.5−6855	X-ray arc around RX J053335−6854.9	Unconfirmed candidate	LCG04
30 DOR C	[BGS2006b] J0536−692	Wrong classification (superbubble)	MFT85
SNR B0538−69.3	[BGS2006b] J0538−693	Unconfirmed candidate	MFD84

Notes. See text in Sect. 3.2 for a description of each object. Reference codes: MFD84: Mathewson et al. (1984); MFT85: Mathewson et al. (1985); LCG04: Lowry et al. (2004); BGS06: Blair et al. (2006); BFP07: Bojičić et al. (2007); PFW08: Payne et al. (2008); BMD10: Badenes et al. (2010).

SNRs, such as MCSNR J0450−7050 (5.7′ diameter, Cajko et al. 2009) or J0506−6541 (6.8′ Klimek et al. 2010). Furthermore, the MCELS image reveals no clear enhanced [S II] emission, and the source was not spectroscopically observed by Payne et al. (2008). In light of this and the absence of X-ray emission, we do not confirm the classification of this object as an SNR and did not include it in the final sample.

RX J0533.5−6855: Lowry et al. (2004) used ROSAT to study the X-ray diffuse emission around the point source RX J053335−6854.9 (referenced as RX J0533.5−6855 in Simbad) and concluded that the X-ray arc seen was a large SNR candidate; they classified the X-ray point source as a dwarf M2-M3 star in the Solar neighbourhood. This region was covered in the *XMM-Newton* survey. The diffuse emission detected with ROSAT is found to be part of larger scale structures from the hot phase of the LMC ISM. There is *no* large SNR around RX J0533.5−6855.

30 DOR C: this is a large shell seen in X-rays with a non-thermal spectrum (Bamba et al. 2004; Kavanagh et al. 2015a). Its nature as a superbubble rather than a standard SNR was already recognised by Mathewson et al. (1985). It was however listed as an SNR in Blair et al. (2006, with the identifier [BGS2006b] J0536−692) and BMD10, as [BMD2010] SNR J0536.2−6912. Interestingly, there *is* an SNR (in projection) in 30 DOR C (MCSNR J0536−6913, Kavanagh et al. 2015a), but it was revealed only later and is most likely distinct from the non-thermal shell.

SNR B0538−69.3: the first classification as an SNR dates back to Mathewson et al. (1984), based on radio and weak optical evidence. BMD10 included that source with the wrong J2000 coordinates. Blair et al. (2006) used the correct position but did not detect UV emission from the object. B0538−69.3 is unusually bright in radio (Miroslav Filipović 2014, personal communication) considering the general lack of X-ray and optical emission. Mathewson et al. (1984) noted that the absence of X-ray emission might be due to the high $N_{\rm H}$ towards this region of the LMC. However, other SNRs are found in that region (e.g. MCSNR J0536−6913, DEM L299, the Honeycomb nebula), so a negative result with *XMM-Newton* is puzzling. This objects remains at best an SNR *candidate*.

3.3. The final sample

Our compilation results in a list of 59 definite SNRs. In Table C.1 we list the final sample of LMC SNRs used in this work. Basic information is given for each object: MCSNR identifier and old name, position, X-ray data available, and reference. In addition, we added columns with X-ray results: X-ray luminosity (Sect. 5 and 7), X-ray size (Sect. 4.1), and $N_{\rm H}$ fraction (Sect. 8). Finally, we give for each SNR the values of the two metrics used to assess the local stellar environment described in Sect. 6. See text in Appendix C for detailed description of each column.

This work focuses on the X-ray emission of LMC SNRs. Therefore, there are only confirmed SNRs in the final sample (no candidate). The resulting list provides the most complete sample of SNRs in the LMC, *as far as X-rays are concerned*: *XMM-Newton* observations exist for 51 SNRs out of the list of 59 SNRs defined here. Out of the eight objects without *XMM-Newton* data available, three were covered with *Chandra*, and two only by ROSAT. Only three objects have not any X-ray information available (yet), though their radio and optical properties warrant their classifications as SNR. In Sect. 7 and Sect. 9, we discuss the total number of LMC SNRs and the overall completeness of the sample.

4. Data analysis

4.1. X-ray imaging

For each SNR, we combined the smoothed images in the soft, medium, and hard bands (obtained as described in Sect. 2.2) into X-ray composite images. These are shown in Appendix F. The same images are used to obtain X-ray contours to help in defining regions for spectral extraction (Sect. 4.2.2).

The study of the size distribution of SNRs provides clues to small-scale structures in galaxies and the energy and matter cycles in the ISM. The sample of LMC SNRs (at various levels of completeness) has been already used for such studies (e.g. Mathewson et al. 1983, BMD10). An SNR can appear to have different sizes depending on the wavelength (e.g. a larger radius in radio than in X-rays), or can have an asymmetric morphology that complicates the definition of its "size". To help future studies of the size distribution, we provide in this work the *maximal* extent of each SNR in X-rays, which we measured from the X-ray images and contours. The values are listed in Table C.1. The size distribution of LMC remnants, combining measurements at various wavelengths, is presented and discussed in Bozzetto et al. (in prep.).

4.2. X-ray spectra

4.2.1. Analysis method

SNRs are *extended* X-ray sources, and many of those in our sample have a low surface-brightness. Consequently, the analysis of their spectra is challenging. A careful treatment of the background, both instrumental and astrophysical, is utterly important in order to obtain meaningful fits and extract the purest possible information from the source. It is not desirable to simply subtract a background spectrum extracted from a nearby region, because of the different responses and background contributions associated to different regions, and because of the resulting loss in the statistical quality of the source spectrum. An alternative method, which we used in this work, is to extract a nearby background spectrum, define a (physically motivated) model for the background and simultaneously fit the source and background spectra. Below, we explain the method in detail. Our account of the background is detailed in Appendix A. The only source for which a different method was used is SNR 1987A, as described in Sect. 5.3.

The spectral-fitting package XSPEC (Arnaud 1996) version 12.8.0m was used to perform the spectral analysis. Unless otherwise stated, spectra were rebinned with a minimum of 25 counts to allow the use of the χ^2-statistic. Interstellar absorption was reproduced by two photoelectric absorption components (`phabs` and `vphabs` in XSPEC, where the previx "v" indicates that abundances can vary), one with a column density $N_{\rm H\ Gal}$ and solar abundances for the foreground Galactic absorption, and another one with $N_{\rm H\ LMC}$ and LMC elemental abundances (Russell & Dopita 1992) for absorption within the LMC. Cross-sections for photoelectric absorption were set to those of Balucinska-Church & McCammon (1992). The foreground column density $N_{\rm H\ Gal}$ at the location of each analysed source is taken (and fixed) from the H I maps of Dickey & Lockman (1990, available online on the HEASARC pages[9]).

For the analysis of one extended source, two different regions are defined: i) a source spectrum extraction region (hereafter `SRC` region); and ii) a background spectrum extraction region (hereafter `BG` region). Two spectra are extracted per instrument (pn, MOS1, and MOS2) from each region, one from the event list of the science observation, the second from the FWC data. The FWC spectra must be extracted at the same *detector* position as in the science observation, because of the strong position-dependency of the instrumental background for both pn and MOS. The `SRC` and `BG` regions are best defined in World Coordinates System (WCS, i.e. sky position[10]). Therefore, we first project the FWC data at the same sky position as the science observation, using its attitude history file and the SAS task `attcalc`. One can then use the same extraction regions to select FWC spectra.

The four spectra are fitted simultaneously over the 0.3 keV−12 keV range. The instrumental background model is constrained by the FWC data, and included (with tied parameters) in the spectra from the science observation. The science spectrum in the `BG` region therefore allows the parameters of the astrophysical X-ray background (AXB) to be determined. It is assumed that the temperature of the thermal components and the surface brightness of the thermal and non-thermal components do not vary significantly between the `SRC` and `BG` regions. Thus, the appropriate temperature and normalisation parameters are linked. All background components are then accounted for, and one can explore the intrinsic emission from the source using several emission models (Sect. 4.2.3).

Regarding which instruments are used, several configurations are possible, depending on the data present. Ideally, one would use all EPIC instruments (pn+MOS1+MOS2) together. However, our analysis method requires FWC data. Those are available for all read-out modes of pn, but only for the full-frame mode of MOS, limiting the use of MOS data in some cases (e.g. MOS in Small Window mode). It also happens that the SNR is outside the MOS field of view, if it is too far off-axis or on one of the damaged chips of MOS1 (Abbey et al. 2006). In these cases only the pn spectrum is used for analysis. The contrary (only MOS spectra available) occurs in rare cases.

About 80% of the SNRs in the sample were observed only once. A few were observed twice in overlapping survey observations; the deep field centred on SNR 1987A contains four SNRs in total, and a plethora of *XMM-Newton* data are at hand for those. To keep the analysis the same for most sources, we restricted the number of observations analysed simultaneously to two for the latter cases. If more than two observations are available, we selected the two deepest datasets (i.e. longest flare-filtered exposure times) for analysis. Finally, N132D is a calibration target and frequently observed. It is however too bright for the full-frame mode; only Small Window and Large Window modes have been used and thus we only used the deepest pn dataset.

It was found more efficient to pre-fit the instrumental and astrophysical background of each SNR. That is, we first fitted the (FWC + AXB) EPIC-pn spectra alone and FWC MOS spectra alone. If the pre-fitting of the background components was satisfactory, their best-fit parameters were used as starting points in the final fit, which includes the SNR emission model. Doing so speeds up the process of analysing the SNR spectrum alone. It also helps, by visual examination of the background fits, to identify problematic cases, as described in Appendix A.

4.2.2. Extraction of the spectra

The first step of the analysis is to extract spectra for each SNR of the sample, as well as corresponding background spectra from nearby regions (using the same observation). Due to the spread in morphology and size of the SNRs, unequal properties of their background (diffuse emission and point source crowding), and their varying location on the EPIC detectors, `SRC` and `BG` regions cannot be created automatically. Therefore, extraction regions were manually defined for each SNR. For the `SRC` region, the constraint was simply to include all the remnant's emission and exclude unrelated point sources that might be located in projection. We used the contours taken from the X-ray image (see Sect. 4.1), combining all observations of each remnant, to identify the boundaries of the SNR emission. If the morphology of the object requires it, an arbitrary shape (polygonal region) is used instead of a circle or ellipse.

The `BG` regions are chosen from different locations on the pn and MOS detectors if needed, in order to be on the same CCD chip as (most of) the SNR emission. In most cases where the remnant was the target of the observation (i.e. was observed on-axis), the same `BG` region defined for pn can also be used for MOS data, because of the chip configuration of the latter with one central chip and six peripheral chips. Detected point sources are also excluded from the `BG` regions.

[9] `http://heasarc.gsfc.nasa.gov/cgi-bin/Tools/w3nh/w3nh.pl`

[10] This is more practical, in particular when several observations of a source with different pointings exist.

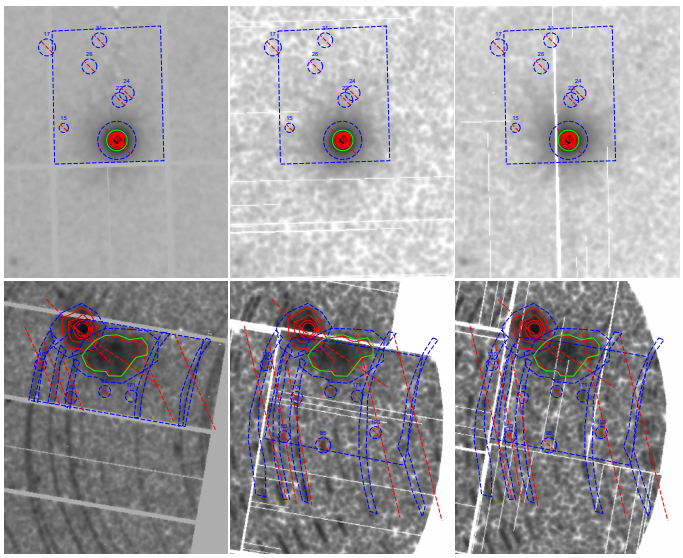

Fig. 3. *Top*: extraction regions used to extract spectra of MCSNR J0519−6902 from EPIC pn, MOS1, and MOS2 detectors (*left to right*). For the scale, we remind the reader that pn chips are 4.4′-wide. The X-ray contours (in red) are used to outline the boundary of the remnant emission and set the radius of the circular SRC region (in green). The BG regions are shown by the blue dashed rectangle. The barred blue circles show detected point sources and a "buffer" area around the SRC region. Those are excluded from the BG region. *Bottom*: same for MCSNR J0547−6943, outlined by the green polygonal region. The barred blue arcs are excluded to avoid single-reflections from LMC X-1.

Two examples are shown in Fig. 3. In the simple case (that of MCSNR J0519−6902), we used a circular SRC region and the same BG regions for all EPIC detectors. In the more complex case of MCSNR J0547−6943 (or DEM L316B), we used a polygonal SRC region; the BG region is narrower for pn than for MOS to fit on a single CCD chip. In addition to point sources, we excluded arc-shaped regions which are affected by instrumental artefacts (single-reflections from LMC X-1). Extraction regions for all LMC SNRs analysed in this work are shown in Appendix F.

Because of the telescope vignetting, the effective area is not constant across the extent of SNRs. To take this into account, all spectra (source and background) are extracted from *vignetting-weighted* event lists. These are created with the SAS task `evigweight`, applied on the calibrated event lists produced by our data reduction pipeline (as described in Sect. 2.2). It assigns a weight to each event of energy E_j at detector coordinates $(detx_j, dety_j)$, which is the inverse of the ratio of the effective area at that position to the central effective area (at the same energy):

$$w_j = \frac{A_{0,0}(E_j)}{A_{detx_j,dety_j}(E_j)}. \quad (1)$$

The corrected event lists are equivalent to that obtained with a flat instrument. For spectral analysis, a flat response file with the on-axis effective area must then be used[11]. Instrumental background spectra were extracted from FWC data at the same detector position as the SRC and BG regions following the method described above.

[11] The extraction radii for the three smallest SNRs (except SNR 1987A which is handled as a point source) result in PSF losses less than 15%.

4.2.3. Spectral models

The model of the SNR emission is built iteratively, in increasing order of complexity. First, a one-component collisional ionisation equilibrium (CIE) model (*vapec* in XSPEC) is tried. The elemental abundances are initially set to the values measured by Russell & Dopita (1992). Their abundance of silicon is highly uncertain, however, and therefore we use an initial value of half solar for Si. Analysis of the residuals and goodness-of-fit reveals if and how the model can be improved, by either thawing some elemental abundances, or switching to a non-equilibrium ionisation (NEI) model (*vpshock* in XSPEC). Abundance effects are manifest when all lines from one element are over- or underestimated compared to the continuum or other elements, while the signatures of NEI are in the residuals from different ions of the same element (e.g. relative strengths of O VII/O VIII lines). We evaluate the significance of the fit improvements (if any) with F-tests. We refer to these one-component models as "1T" (one temperature).

A second component is added if needed; those are the "2T" SNRs. Again we start with CIE, then assess whether there is need for NEI or free abundances in the second component. For several SNRs, the analysis of X-ray colour images already hints at the presence of two components, with e.g. a different temperature, $N_{\rm H}$, or abundance pattern. This iterative process is done until a satisfactory fit is achieved, at which point 90% C.L. errors are computed for all free parameters. More complicated models may be applied/needed for a handful of SNRs, particularly amongst the brightest ones. These cases are presented in Sects. 5.2 and 5.3.

5. The X-ray spectral properties of LMC SNRs

5.1. General properties

Out of the sample of 59 SNRs and 51 with *XMM-Newton* data available, 45 are fitted with 1T or 2T models, while 6, amongst the brightest, are fitted with more complex models (see Sects. 5.2 and 5.3). Six previously known SNRs have been covered by our VLP survey, giving the opportunity to study their spectra with *XMM-Newton* for the first time. Among these, MCSNR J0534−6955 and J0547−7025 were observed with *Chandra* (Hendrick et al. 2003). Reyes-Iturbide et al. (2008) analysed only MOS data of MCSNR J0518−6939 from an archival observation, while we now have EPIC-pn data. We show the *XMM-Newton* spectra from these SNRs in Appendix D.

The results of the spectral analysis for the 1T/2T sample are given in Appendix E (Table E.1). All relevant parameters are listed with their 90% C.L. uncertainties: the fitted LMC absorption column density (Col. 2), plasma temperature kT (3), ionisation age τ (4), emission measure EM (5), and abundances (6). When a second component is used, its parameters are given in Cols. (7)−(11). The first component is the one with higher EM. The quality of the fits are evaluated by the χ^2/ν of Col. (12), where ν is the number of degrees of freedom. The reduced χ^2 values ($\chi^2_{\rm red}$) are also listed in Col. (12). The median $\chi^2_{\rm red}$ is 1.16. 90% of the fitted objects have a reduced χ^2 less than 1.4.

In 32 cases, the SNR is fitted with, or the available data only require, a one component model. Amongst these, 9 do not show significant NEI effects and are fitted with a CIE model. Using a NEI model for these did not result in a statistically significant improvement, neither in the goodness-of-fit sense, nor in terms of residuals. Moreover, the ionisation ages τ in these cases are high and poorly constrained. Therefore we list the CEI model

parameters. In the 23 remaining "1T" objects, better fits are obtained with an NEI model. The plasma temperature for the "1T SNRs" clusters in the 0.25 keV−0.45 keV range. The highest values of temperature (above 1 keV) are associated with the smallest ionisation ages. In at least some cases, this could be an artefact of the analysis due to insufficient data. The ionisation age τ of this sample is broadly distributed around a median value of 1.7×10^{11} s cm^{-3}.

There are 13 SNRs in the 2T sample. Two objects are fitted with two CIE component models (MCSNR J0530−7008 and J0517−6759). The rest was fitted with two NEI components, although for three SNRs the ionisation age of one of the components was unconstrained and on the high end ($\tau \gtrsim 10^{13}$ s cm^{-3}), indicating a plasma close to or in CIE. The median τ of the main component (i.e. that with higher emission measure) for the 2T sample is slightly higher ($5-7 \times 10^{11}$ s cm^{-3}) than that of the 1T sample, but low number statistics preclude a direct comparison. The temperature distribution is bimodal: one component has a median temperature of $kT = 0.31$ keV, the second a higher median of 0.8 keV. In several cases the high-kT component also requires a different abundance pattern, revealing SN ejecta (Sect. 5.5).

For nine SNRs, the data did not require or allow elemental abundances to be fitted. For a few cases, this happens because the spectrum is contaminated by a bright pulsar (N157B and MCSNR J0540−6920), or by LMC X-1 (MCSNR J0540−6944), and the thermal emission is not well separated by *XMM-Newton*. The other SNRs fitted with abundances from Russell & Dopita (1992, RD92 in Table E.1) are relatively faint. The limited available data therefore prevent the use of free abundances in the fits.

Oxygen and iron are the main contributors to the 0.5 keV−2 keV X-ray emission for the relevant plasma temperatures. Consequently, they are the first elements for which abundances can be fitted. Out of the 45 1T/2T SNRs, 35 have at least free O and Fe abundances. Neon and magnesium also have prominent lines routinely detected below 2 keV, and their abundances were fitted in 33 and 30 SNRs, respectively. Silicon is detected and its abundance fitted, in 23 SNRs. This subset has a higher median temperature ($kT \sim 0.6$ keV) than the whole sample, as expected. Indeed, Si emission becomes prominent for higher temperatures than, say, O, Ne, or Fe. While obvious and fitted in all the brightest SNRs, which are younger/hotter, lines of sulphur are not detected in most 1T/2T SNRs. Only a handful (MCSNR J0534−6955, J0547−7025, N63A) allow to fit the S abundances. All have plasma temperatures in excess of 0.8 keV. The fitted abundance patterns can be used to type the supernova progenitor, if ejecta are detected (Sect. 5.5), or to measure metallicity of the LMC ISM (Sect. 5.6).

5.2. The analysis of the brightest SNRs

For six of the brightest SNRs, the simple 1T/2T models approach was clearly insufficient to satisfactorily model the spectra. This is expected, because on the one hand, the exquisite statistical quality of these spectra imply that even a two-component model is not adequate to reproduce the complex multi-phase structure in these objects. On the other hand, the very young SNRs, in addition to a small ambient medium contribution, are dominated by ejecta. Because of stratification of the ejecta heated by the reverse shock, elements synthesised at different radii in the SN explosion can have distinct spectral properties.

All the "bright SNR" sample was observed in individual *XMM-Newton* and *Chandra* pointings. Detailed results are published in several papers (references are given below), with which our results were never at odds. Here, we used multi-temperature empirical models to reproduce the spatially integrated spectra. Thus, we can i) derive accurate X-ray fluxes, so that the luminosity function (Sect. 7) is complete at the bright end, ii) measure the properties of the Fe K emission, if present (see Sect. 5.4), and iii) obtain spectral properties (e.g. $N_{\rm H}$, kT, τ) for statistical studies and comparison of their distributions for various sub-samples (Sect. 7). The adopted models are described below. The spectral parameters are given in Table E.2 and Table E.3.

DEM L71 (MCSNR J0505−6753): DEM L71 is a notorious type Ia SNR, owing to the detection of iron-rich ejecta (e.g. Hughes et al. 1995). van der Heyden et al. (2003) presented the *XMM-Newton* EPIC and RGS results for this remnant, and Hughes et al. (2003) those obtained with *Chandra* observations. Different conditions are measured in the shell and central regions. It is then unsurprising that a 2T model as used for other SNRs did not produce acceptable fits. Instead, we obtained satisfactory results with three components: Two components ("Fe-low kT" and "Fe-high kT") had Si, S, and Fe (the main nucleosynthesis products of Ia SNe) freed and common to the two components, while other metals were set to zero. These components account for the ejecta-rich emission, as well as the Si, S, and Fe contribution of the ISM. A third component, with O, Ne, and Mg abundances free and Si, S, Fe set to zero, accounts for the bulk of ISM emission.

In addition, Fe K emission is clearly detected, pointing to the presence of very hot ejecta ($kT > 2$ keV). The statistical weight of this feature remains small. Therefore, instead of adding another thermal component, we modelled the line with a Gaussian. The parameters of the Fe K line are used in comparison with other SNRs in Sect. 5.4. The ejecta components have best-fit temperatures of ∼0.4 keV and ∼0.9 keV (Table E.2). The ionisation age of the cooler component is twice that of the hotter one. The ISM component has a temperature of $kT = 0.46$ keV, the same as measured with *Chandra* (Hughes et al. 2003), and in between the two temperatures used for the shell emission by van der Heyden et al. (2003).

N103B (MCSNR J0509−6844): the spectrum of N103B is remarkable because of the numerous lines from highly ionised metals: Si XII and Si XIV, S XV and (marginally) S XVI, Ar XVII, and Ca XIX. A strong Fe K blend is also detected. We fit the spectrum with the same three-temperature model as for DEM L71. One component had abundances fixed to RD92, accounting for the ISM emission. Two components with different kT and τ were used to reproduce the (dominating) ejecta emission. All relevant elements (O, Ne, Mg, Si, S, Ar, Ca, and Fe) were freed, but common to both components. A Gaussian was also included to fit the Fe K feature.

With this model, the spectrum of N103B is well reproduced across the whole 0.3 keV−8 keV band. The results are comparable to those of van der Heyden et al. (2002, focusing on *XMM-Newton* data) and Lewis et al. (2003, with *Chandra*), especially regarding: i) the column density $N_{\rm H} \sim 3 \times 10^{21}$ cm^{-2}; ii) the presence of one high ionisation age component (at $kT \sim 0.7$ keV) and a hotter (1.6 keV) underionised component. Because the Fe K blend is modelled separately with a Gaussian, the fitted temperature of the hottest component is lower than in the previous references; iii) high abundances of S, Ar, and Ca.

N132D (MCSNR J0525−6938): Behar et al. (2001) presented the *XMM-Newton* observations of N132D from the Performance Verification programme. Results of the *Chandra* ACIS-S observations can be found in Borkowski et al. (2007). Both instruments spatially resolve the SNR into regions with different spectral properties. Therefore, though a three-temperature model can reproduce the main features of the spectrum (thus allowing us to accurately measure the integrated flux of the remnant), strong residual structures are seen between 0.5 keV and 1 keV, where the strongest variations are observed (lines of O, Ne, Fe).

The best fit is obtained with a cool (∼0.5 keV) component with abundances close to the normal LMC values (i.e. it represents a blast wave component) that dominates the soft emission (below 1.5 keV). A second component with $kT \sim 1$ keV is characterised by enriched levels of O, Ne, and Mg, as well as a higher column density ($\sim 10^{22}$ cm^{-2}). This component thus describes the bulk of the ejecta emission, and accounts for most of the Si and S emission. Finally, the presence of highly ionised iron is evident from the 6.69 keV line (see Table 2), corresponding to the Kα energy of Fe XXV. This indicates a third, very hot component (∼5 keV). In this component only Fe, Ar, and Ca are included. The two latter elements improve the residuals around 3.1 keV (Ar XVII), and 3.9/4.1 keV (Ca XIX and Ca XX). These K lines were already mentioned in the early *XMM-Newton* results (Behar et al. 2001).

0519−69.0 (MCSNR J0519−6902): the SNR was observed early in the *Chandra* and *XMM-Newton* missions. In addition, the LMC survey covered the source, at an off-axis angle of ∼9′, adding 23 ks and 27 ks to the existing 8 ks and 46 ks of full-frame pn and MOS data, respectively. Spectra from the two observations were fitted simultaneously. 0519−69.0 exhibits strong lines of Si, S, Ar, and Ca, as well as prominent Fe L and K blends. To reproduce the spectra we used the multi-component approach of Kosenko et al. (2010), who extensively studied the *XMM-Newton* and *Chandra* data.

First, one NEI component with LMC abundances accounts for circumstellar medium (CSM) or ISM emission. Then, one NEI component for each (group of) element(s) having detected lines: oxygen, silicon and sulphur, argon and calcium, and iron. In the latter case two NEI components with distinct parameters are used, as the spectrum evidently includes both medium temperature and very hot iron. Due to the low count rate, and therefore statistical weight, of the Fe K blend, the hot iron component was driven to fit lower energy lines instead. To alleviate this issue we fitted the high-energy part of the spectrum separately with this component, then froze the best-fitting parameters in the global fits. Residuals around 0.72 keV (lines of Fe XVII) were fitted with an additional Gaussian line.

0509−67.5 (MCSNR J0509−6731): *XMM-Newton* observed the SNR for ≈40 ks in 2000, with pn operated in Large Window mode. This dataset is presented in Kosenko et al. (2008), while Warren & Hughes (2004) reported the spectral and imaging analysis of a *Chandra* observation. Finally, Badenes et al. (2008) attempted to reproduce spectra from both instruments using a grid of hydrodynamical models and an X-ray emission code. Inconsistencies between pn and MOS spectra were found, with lines in the pn spectrum (red-)shifted relative to those in MOS spectra by about 1%. This is likely a gain issue of the pn instrument. We discarded spectra from the MOS instruments, as they were operated in Small Window mode, for which no FWC data are available. To get the spectral model to match the observed energies of atomic lines, we freed the "redshift" parameter available in XSPEC models, which allows an ad hoc change of the energy scale. Satisfying results were obtained for a shift of ≈1%, which is the measured pn/MOS discrepancy Kosenko et al. (2008).

As for J0519−6902, lines from heavy elements are prominent, and we used a multi-component model. Si, S, and Ar were grouped in a NEI component, and shared the same temperature and ionisation age. Another NEI component modelled the continuum+lines emission from the CSM/ISM. No Si, S, Ar, or Ca were included in this component. Iron was included in two NEI components, one with a medium temperature (∼1.4 keV) and a high-kT one (∼11 keV) that reproduces the strong Fe K line. The latter component also includes calcium. Even with this model, residuals remained around Fe lines (0.72 keV and 1.22 keV), which we fitted with two Gaussian lines. The very high temperature of the second Fe component is atypical for SNRs, but was also suggested in *Chandra* data by Warren & Hughes (2004). The SNR exhibits a high-energy continuum tail, which previous studies tried to reproduce with non-thermal models. This tail can also be reproduced with the Bremsstrahlung continuum of a high-kT thermal model, driving our fit to temperatures above 10 keV. Furthermore, we already noted the energy shift issue of the pn spectra, that results in a small centroid energy of the Fe K line for a given fitted kT. Given this caveats, it remains unclear whether the 11 keV plasma is physical.

5.3. Update on the monitoring of SNR 1987A

SN 1987A, the nearest supernova in almost 400 years, was discovered in the LMC on 23 February 1987. It is exceptional in many ways and has been extensively studied ever since. We have the unique opportunity to follow the early evolution of a supernova *remnant* (hence the use of the identifier "SNR 1987A"[12]). Results from the many existing *XMM-Newton* observations of SNR 1987A are presented in Haberl et al. (2006), Heng et al. (2008), and Sturm et al. (2010). Maggi et al. (2012b, hereafter M12) analysed data from the 2007–2011 monitoring, focusing on the rapid evolution of the X-ray light curve and the properties and evolution of the Fe K lines, which were detected unambiguously for the first time. However, the spectral parameters (except fluxes and Fe K line properties) were not given in M12. We take advantage of this work to give these detailed results, and include an unpublished observations (ObsID 0690510101) performed on December 2012, after M12 was released.

All spectra from SNR 1987A were extracted from a circular region centred on the source, with a radius of 25″. The use of spatially integrated spectra is dictated by the small radius of the source (still less than 1″, Helder et al. 2013), which is completely unresolved by *XMM-Newton*. The background spectra were extracted from a nearby point-source-free region common to all observations. Only single-pixel events (PATTERN = 0) from the pn detector were selected. Contrary to all other SNRs in this work, the background spectra were not modelled but *subtracted* from the source spectra. We used the same three-component plane-parallel shock model as in M12, with one fixed-temperature component ($kT = 1.15$ keV) and free abundances of N, O, Ne, Mg, Si, S, and Fe. EPIC-pn spectra from all seven epochs of the monitoring are fitted simultaneously between 0.2 keV and 10 keV, with common abundances and

[12] In our nomenclature SNR 1987A is also given the name MCSNR J0535−6916.

Table 2. Fe K line properties of LMC SNRs.

MCSNR	Alt. name	type	Energy centroid (eV)		Line luminosity (10^{42} ph s^{-1})	
			XMM-Newton	*Suzaku*	*XMM-Newton*	*Suzaku*
J0509−6731	B0509−675	Ia	6432^{+29}_{-27}	6425^{+14}_{-15}	0.87 ± 0.21	0.96 ± 0.12
J0505−6753	DEM L71	Ia	6494 ± 58	–	$0.26^{+0.08}_{-0.09}$	–
J0509−6844	N103B	Ia	6514^{+31}_{-32}	6545 ± 6	5.10 ± 0.87	6.43 ± 0.30
J0519−6902	B0519−690	Ia	6543^{+28}_{-31}	6498^{+6}_{-8}	1.71 ± 0.45	2.78 ± 0.15
J0526−6605	N49	CC	–	6628^{+29}_{-26}	$<4.75^{a}$	0.54 ± 0.12
J0535−6916	SNR 1987A[b]	CC	6635 ± 70	6646^{+55}_{-54}	0.64 ± 0.18	0.57 ± 0.24
J0535−6602	N63A	CC	6683^{+88}_{-99}	6647^{+16}_{-17}	$2.36^{+1.03}_{-1.08}$	2.57 ± 0.36
J0525−6938	N132D	CC	6685^{+15}_{-14}	6656 ± 9	4.58 ± 0.58	5.47 ± 0.51

Notes. *Suzaku* results are from Yamaguchi et al. (2014). [(a)] 3σ upper limit. [(b)] The quoted numbers are average values over the last six epochs, and the uncertainties are the rms scatter. Note that we found the energy centroid to evolve rapidly at recent epochs (see Sect. 5.3).

$N_{\mathrm{H\ LMC}}$. To characterise the Fe K line, we performed separate fits in the range (5–8) keV on the *non-rebinned* spectra using the C-statistic (Cash 1979). We used a Bremsstrahlung model for the continuum and a Gaussian for the Fe K line complex.

The simultaneous (broad-band) fit was satisfactory, with $\chi^2 = 5114.2$ for 4109 degrees of freedom (reduced $\chi^2_r = 1.24$). Spectral results are the same as in M12. We give the best-fit parameters for all seven epochs in Table E.3. We list soft (0.5 keV−2 keV) and hard (3 keV−10 keV) X-ray fluxes at all epochs, with 3σ uncertainties (99.73% confidence level, C. L.) in Table E.3. Echoing the findings of M12, we see that the soft X-ray flux keeps increasing after the 25th anniversary of SNR 1987A. Since 2011, however, the rate of increase has dropped below 10% per year, showing that subsequent observations of SNR 1987A with *XMM-Newton* are highly desirable to follow the evolution of the X-ray flux and to identify the turnover point.

The central energy, σ-width, total photon flux and equivalent width (EW) of the Fe K feature are also listed in Table E.3. Up to December 2011 the results are the same as in M12. The new data point (December 2012) reveals a line with roughly the same flux but a significantly higher central energy ($6.78^{+0.06}_{-0.05}$ keV) than previously (6.60 ± 0.01 keV, averaging the earlier measurements). This hardening likely indicates an increased contribution from highly ionised iron (Fe XXVI) that prior to 2012 was either absent (as iron was in lower ionisation stages) or too weak to be detected. With the resolution of pn and the statistics in our hand, it is not possible to resolve the K-shell lines from various Fe ions, which will become possible with next-generation X-ray calorimeters onboard Astro-H (Takahashi et al. 2012) or Athena (Barret et al. 2013).

5.4. Fe K emission from LMC SNRs

Yamaguchi et al. (2014) used *Suzaku* to systematically search for Fe K emission from Galactic and LMC SNRs. Fe Kα emission was detected in 23 SNRs, including seven remnants in the LMC. Their essential finding is that the centroid energy of the Fe K emission, determined by the ionisation state of iron, is a powerful tool for distinguishing progenitor types. Indeed, the Fe K emission of type Ia remnants is significantly less ionised than in CC-SNRs. Furthermore, there is a positive correlation between the Fe Kα line luminosity and centroid energy *within each progenitor group*.

Because the Fe K blend is a promising typing tool, we extended the search for Fe K emission of Yamaguchi et al. (2014) to all LMC SNRs observed with *XMM-Newton*. Compared to the *Suzaku* sample, the coverage is more complete (i.e. more SNRs observed) and more sensitive (the EPIC-pn effective area is slightly higher than that of *Suzaku*'s XIS, even combining all detectors), and Fe K can potentially be detected from more SNRs.

In Table 2, we give the results for all LMC SNRs with detected Fe K emission, ranked by increasing centroid energy. The *XMM-Newton* and *Suzaku* results are consistent within the uncertainties. Strikingly, we found Fe K emission undetected with *Suzaku* for only one source, DEM L71. Its line luminosity is smaller than from any other LMC remnant. Likely, this fact and the smaller effective area of XIS explain why it was undetected in the 100 ks-long *Suzaku* observation of the remnant (Hiroya Yamaguchi 2014, personal communication). Furthermore, the second faintest Fe K line from LMC SNRs is found in N49. With *XMM-Newton* one does not formally detect the line. Including a Gaussian at the energy measured with *Suzaku*, the *XMM-Newton* spectrum allows a line flux an order of magnitude above that actually detected. This is only a statistical issue. Indeed, there are less than 10 ks of EPIC-pn data available, which is no match to the 158 ks spent by *Suzaku* on N49 when detecting the Fe K line.

The properties of the Fe K emission from DEM L71 fit well with its type Ia nature. Furthermore, Yamaguchi et al. (2014, their Fig. 1, right) used simple (one-dimensional) theoretical models of type Ia SNe exploding in uniform ambient media of various densities to predict the luminosity and energy of the line. Even with this simplistic approach, they are able to reproduce all the parameter space spanned by type Ia SNRs. In this context, the location of DEM L71 in the Fe K luminosity-energy diagram is well reproduced by a delayed-detonation model with a rather high explosion energy (1.4×10^{51} erg, DDTa in Badenes et al. 2003, 2005), in an ambient medium of density $\rho = 2 \times 10^{-24}$ g cm^{-3}, at age between 2000 yr and 5000 yr. This is in line with the measured density and age of DEM L71 (van der Heyden et al. 2003; Ghavamian et al. 2003). Furthermore, the DDTa model predicts a silicon-to-iron mass ratio of 0.08, close to that measured in X-rays (~0.15, Hughes et al. 2003; van der Heyden et al. 2003). Since the hot, Kα-emitting iron was previously overlooked, the $M_{\mathrm{Si}}/M_{\mathrm{Fe}}$ ratio should be even lower, closer to the prediction of the DDTa model.

The dearth of Fe K-emitting remnants, aside from the combined *XMM-Newton*/*Suzaku* sample (eight objects), is somehow expected. Indeed, most of the SNRs have plasma temperatures less than 1 keV (Sect. 5.1), which is too low to excite iron K-shell electrons, so that no emission is expected. MCSNR J0547−6973 is one case where a hotter spectral component ($kT \sim 2.2$ keV) is present but no Fe K emission is detected, likely because the emission measure of that component is too low, so that it is not detectable with current instruments. Even if a spectrally unresolved hot iron component exists in more LMC remnants, a further issue is again detectability. The LMC SNRs of Yamaguchi et al. (2014) have hard X-ray (2 keV−8 keV) luminosities above 10^{35} erg s^{-1}. There are only two other SNRs in the LMC above this level, MCSNR J0540−6920 and N157B, which are powered by a bright pulsar and pulsar wind nebula, respectively.

Despite these observational difficulties, it is very likely that the sample of LMC Fe K-emitting remnants (of Yamaguchi et al. 2014, plus DEM L71) is complete, because all young SNRs ($\lesssim$5000 yr old) are now known and observed in X-rays. Translating the fraction of remnants with Fe K emission in the LMC ($\approx$13%) to the Galactic population (294 objects, Green 2014), we expect more than 40 such sources in the Milky Way. This number is a lower limit, since fainter line fluxes than in the LMC can be reached. Yamaguchi et al. (2014) list 16 Galactic SNRs detected, out of 56 objects observed with *Suzaku* (Ferrand & Safi-Harb 2012, online database[13]). About 80 more SNRs were observed and detected with *Chandra* or *XMM-Newton*, and 150 have not been covered in X-rays. A systematic analysis of all X-ray-detected SNRs and new/deeper observations of promising candidates with more sensitive instruments (e.g. *XMM-Newton* vs. *Chandra*, future missions such as Athena) will provide a better census of Fe K lines in SNRs. This will allow us to type more remnants and to study the pre-SN evolution of their progenitors.

5.5. Detection of SN ejecta

When SN ejecta give an observable contribution to the X-ray emission of an SNR, the fitted abundances, or rather the fitted *abundance ratios*, will reflect the nucleosynthesis yields of either thermonuclear or CC SNe. To identify SNRs with detected ejecta and the origin thereof, we computed abundance ratios X/Fe, where X is O, Ne, Mg, or Si. The ratios are normalised with respect to $(X/Fe)_{LMC}$, the corresponding ratios with the LMC abundances (from Russell & Dopita 1992). As CC-SNRs produce large amounts of light-Z elements and little iron, high $(X/Fe)/(X/Fe)_{LMC}$ ratios (in excess of one) indicate a massive star progenitor. On the contrary, the main product of thermonuclear SNe is iron, and ejecta in type Ia SNRs (if detected), are expected to have $(X/Fe)/(X/Fe)_{LMC} \ll 1$.

In Fig. 4, the abundance ratio diagrams of all SNRs with corresponding fitted abundances are shown. The samples of SNRs with a secured CC or type Ia classification (as described in Appendix B) are marked. Evidently, many of the known CC SNRs are located in regions of super-LMC X/Fe. The known type Ia SNRs are unsurprisingly in the $(X/Fe)/(X/Fe)_{LMC} \ll 1$ regions of the diagrams, because in most cases it is this very iron-enhancement that was used to classify them.

Several sources without previous classification are located in the high- and low-ratio regions of the diagrams. For typing purpose, we assign "high X/Fe" and "low X/Fe" flags to these objects, using the following scheme: For each element X, we plot the cumulative distribution of the ratio $(X/Fe)/(X/Fe)_{LMC}$.

[13] http://www.physics.umanitoba.ca/snr/SNRcat/

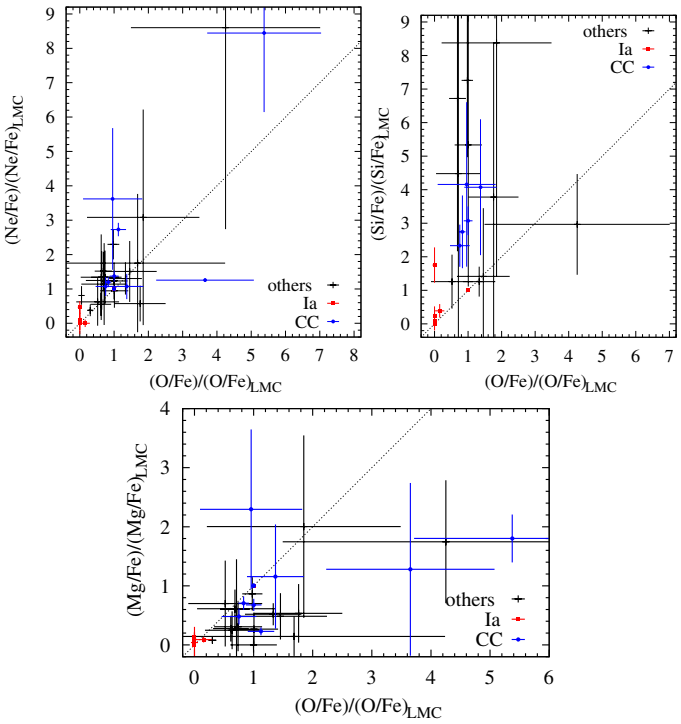

Fig. 4. Abundance ratio diagrams of LMC SNRs with fitted abundances. Sources firmly classified as type Ia or CC-SNRs are plotted in red and blue, respectively, and the rest of the sample in black. See text (Sect. 5.5) for details.

Table 3. Constraints used for the identification of ejecta in SNR spectra.

X	"high X/Fe" flag		"low X/Fe" flag	
	(1)	(2)	(1)	(3)
O	>1.0	>0.83	<0.60	<0.83
Ne	>1.43	>1.30	<0.55	<1.30
Mg	>0.62	>0.48	<0.22	<0.48
Si	>2.70	>1.60	<1.30	<1.60

Notes. (1) Constraints on the ratio $(X/Fe)/(X/Fe)_{LMC}$. (2) Constraints on the lower limit $(X/Fe)/(X/Fe)_{LMC} - \Delta(X/Fe)$, where $\Delta(X/Fe)$ is the uncertainty of the abundance ratio. (3) Constraints on the upper limit $(X/Fe)/(X/Fe)_{LMC} + \Delta(X/Fe)$.

We then assign a "high X/Fe" flag to an object if its ratio is above the 68th percentile ($\sim 1\sigma$) of the cumulative distribution. Symmetrically, a "low X/Fe" flag is given if the ratio is below the 32th percentile. Since the uncertainties in the fitted abundances can be large, it is necessary to put a second constraint using the uncertainty of the ratio, noted $\Delta(X/Fe)$: a "high X/Fe" flag is only given if the lower limit (i.e. ratio minus the uncertainty) is above the median of the cumulative distribution. For a "low X/Fe" flag the upper limit must be below the median. This excludes all cases where the ratios are elevated (or much smaller than one) but highly uncertain. Though some of the criteria for "low X/Fe" flags may seem high, the selected SNRs have actual ratios well below half the LMC average (well below 0.2 times the average for Mg). The criteria for "high X/Fe" and "low X/Fe" flag are given in Table 3. There are 23 SNRs in the 1T/2T sample with high or low abundance ratio flags, as listed in Table 4. These flags are used in Sect. 6 to help the typing of all LMC SNRs.

Table 4. 1T/2T SNRs with detected ejecta (top part), and used for measurements of ISM composition (bottom part).

MCSNR	Old name	SN type	High X/Fe flags				Low X/Fe flags			
			O	Ne	Mg	Si	O	Ne	Mg	Si
J0453-6829	B0453-685	CC	–	–	Y	Y	–	–	–	–
J0506-6541	–		–	Y	–	–	–	–	–	–
J0506-7026	[HP99] 1139		–	–	–	–	Y	Y	Y	–
J0508-6830	–	Ia	–	–	–	–	Y	–	–	–
J0508-6902	[HP99] 791	Ia	–	–	–	–	Y	–	–	–
J0511-6759	–	Ia	–	–	–	–	Y	–	–	–
J0519-6926	B0520-694		–	Y	Y	Y	–	–	–	–
J0523-6753	N44		Y	Y	Y	–	–	–	–	–
J0525-6559	N49B	CC	–	Y	Y	Y	–	–	–	–
J0526-6605	N49	CC	Y	–	Y	Y	–	–	–	–
J0529-6653	DEM L214		Y	–	–	–	–	–	–	–
J0531-7100	N206		Y	–	–	Y	–	–	–	–
J0533-7202	1RXSJ053353.6-7204		–	–	–	–	–	–	Y	–
J0534−6955	B0534−699	Ia	–	–	–	–	Y	Y	Y	–
J0534-7033	DEM L238	Ia	–	–	–	–	Y	Y	Y	Y
J0535-6602	N63A	CC	Y	Y	–	–	–	–	–	–
J0535-6918	Honeycomb		–	–	–	Y	–	–	–	–
J0536-6735	DEM L241	CC	Y	Y	Y	–	–	–	–	–
J0536-6913	B0536-6914	CC	Y	–	–	–	–	–	–	–
J0536-7039	DEM L249	Ia	–	–	–	–	Y	Y	Y	Y
J0537-6628	DEM L256		–	–	–	–	–	–	Y	–
J0547-6941	DEM L316A	Ia	–	–	–	–	Y	Y	Y	Y
J0547-7025	B0548-704	Ia	–	–	–	–	Y	Y	Y	–

			ISM abundance			
			O & Fe	Ne	Mg	Si
J0450-7050	B0450-709		Y	Y	Y	–
J0453-6655	N4		Y	Y	Y	–
J0453-6829	B0453-685	CC	Y	Y	–	–
J0454-6626	N11L		Y	Y	Y	–
J0505-6802	N23	CC	Y	Y	Y	Y
J0514-6840	–		Y	–	–	–
J0518-6939	N120		Y	Y	Y	Y
J0519-6926	B0520-694		Y	–	–	–
J0527-6912	B0528-692		Y	Y	Y	Y
J0528-6727	DEM L205		Y	–	–	–
J0531-7100	N206	CC	–	Y	Y	–
J0532-6732	B0532-675		Y	Y	Y	Y
J0533-7202	1RXSJ053353.6-7204		Y	Y	–	–
J0535-6918	Honeycomb		Y	Y	Y	–
J0543-6858	DEM L299		Y	Y	Y	Y
J0547-6943	DEM L316B		Y	Y	Y	Y

Notes. The classification given (type Ia or core-collapse) is described in Appendix B.

5.6. Metal abundances of the LMC ISM

When no SN ejecta is detected, the X-ray emission is dominated by the ISM swept-up by the SN blast wave. Therefore, the fitted abundances in these cases provide us with measurements of the chemical composition of the gas phase of the LMC ISM. Russell & Dopita (1992) and Hughes et al. (1998) have used samples of SNRs to obtain the abundance of some elements (using optical and X-ray observations, respectively), but the smaller sample of known SNRs and sensitivity of the X-ray instrument used (*ASCA*) at the time limited the number of SNRs eligible to measure LMC abundances.

We first selected all 1T/2T SNRs with fitted abundances but no high or low abundance ratios. To increase that sample, we included SNRs where some abundances are enhanced but others can still be used. For example in MCSNR J0453−6829, the spectrum is enhanced in Mg and Si, but the fitted values for O, Ne, and Fe, are still (assumed to be) reflecting the LMC ISM abundance. Furthermore, if the abundance of a given element is too uncertain, then the SNR is not used to measure the average abundance of that element. This limits in particular the size of the SNR sample allowing the abundance of silicon to be measured.

In Table 4 we give the list of SNRs used to measure the abundance of O, Ne, Mg, Si, and Fe, or a subset of these elements. The measured abundances for this sample are plotted relative to solar values in Fig. 5. The final LMC abundances are obtained by taking the average values from all SNRs where an element is used; the errors given are the RMS scatter amongst the SNRs used. This method is similar to that of Hughes et al. (1998). Resulting abundances range from ∼0.2 solar for oxygen to ∼0.7 solar for silicon. The results are listed in Table 5. The absolute abundances, in the form 12 + log(X/H) (by number), are given, in comparison with results from Russell & Dopita (1992)

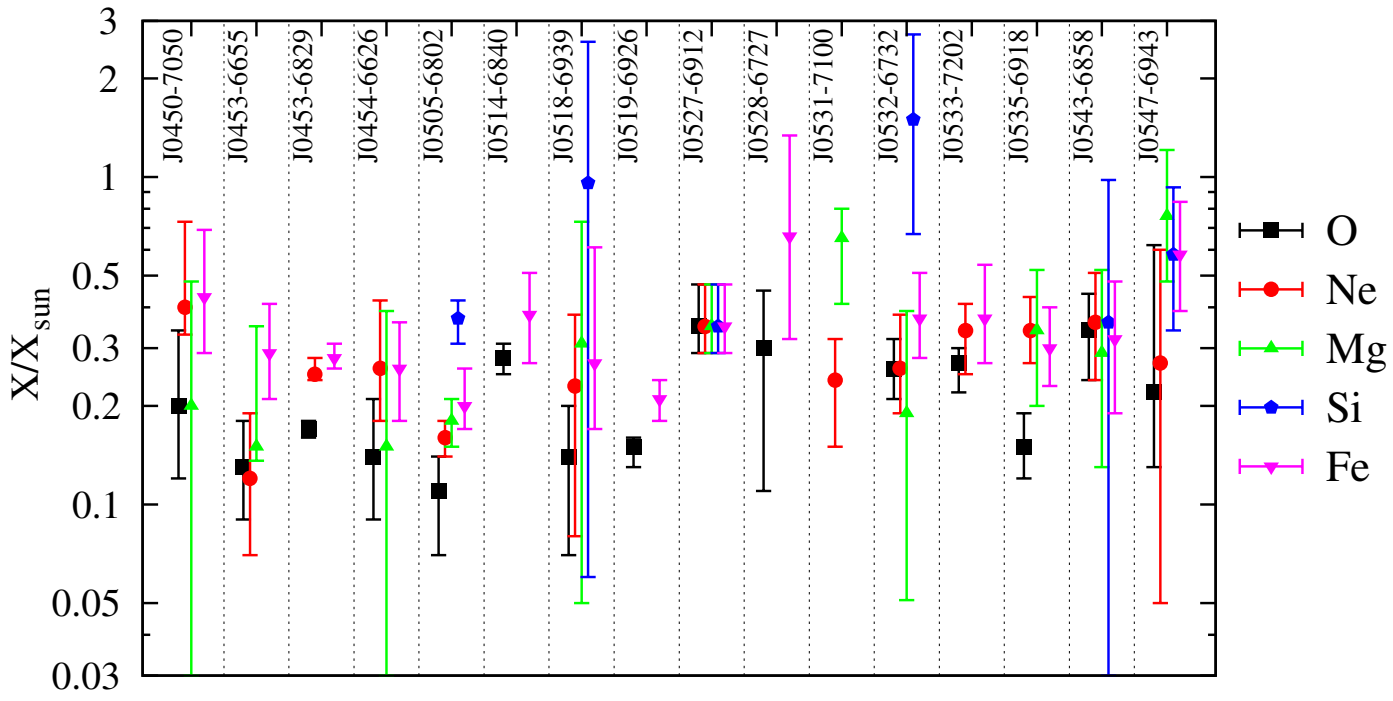

Fig. 5. LMC ISM abundances, relative to the solar values of Wilms et al. (2000), measured in a sample of 16 X-ray SNRs. The selection of the sample and the measurements of abundance are described in Sect. 5.6.

Table 5. LMC abundances.

Element	$X/X_\odot$ (1)	N (2)	rms (3)	12 + log(X/H)	Hughes et al. (1998)	RD92
O	0.21	15	0.08	$8.01^{+0.14}_{-0.21}$	8.21 ± 0.07	8.35 ± 0.06
Ne	0.28	13	0.08	$7.39^{+0.11}_{-0.15}$	7.55 ± 0.08	7.61 ± 0.05
Mg	0.33	11	0.19	$6.92^{+0.20}_{-0.37}$	7.08 ± 0.07	7.47 ± 0.13
Si	0.69	6	0.42	$7.11^{+0.20}_{-0.41}$	7.04 ± 0.08	7.81[a]
Fe	0.35	15	0.12	$6.97^{+0.13}_{-0.18}$	7.01 ± 0.11	7.23 ± 0.14

Notes. (1) Abundance relative to the solar value of Wilms et al. (2000). (2) Number of SNRs used to measure $X/X_\odot$. (3) RMS scatter amongst the N SNRs. [(a)] Silicon abundance was quoted as highly uncertain in Russell & Dopita (1992).

and Hughes et al. (1998). Abundances of Fe and Si measured with *XMM-Newton* are in good agreement with the results measured for a different sample of SNRs by Hughes et al. (1998)[14]. More recent studies of abundances in the LMC, using large samples of field stars (Cole et al. 2005; Pompéia et al. 2008; Lapenna et al. 2012; Van der Swaelmen et al. 2013), can be used to evaluate our results. The metallicity distributions [Fe/H][15] peak at about −0.5 dex for most field star samples (Lapenna et al. 2012), corresponding to 12 + log(Fe/H) = 7. This matches very well our value based on *XMM-Newton* SNRs ($6.97^{+0.13}_{-0.18}$), indicating no metallicity difference between field stars and gas-phase ISM.

However, the abundances of light α-elements tend to be lower (by ∼0.15 dex−0.2 dex) compared to Hughes et al. (1998), although the results for Mg and Ne might still be reconciled given the larger uncertainties. Still, we measured a ratio [O/Fe] of −0.21 while *ASCA* SNRs gave −0.06. The likely explanation is two-fold. First, the α-elements abundance has an intrinsic scatter (about 0.05 dex−0.08 dex at the relevant metallicity, Van der Swaelmen et al. 2013) that can partly explain the discrepancy. The second reason is the sample used by Hughes et al. (1998): N132D, N49, and N49B contain regions that have been (since then) found to be enhanced in low-Z elements (e.g. this work, and references in Appendix B), while the bright central regions of the type Ia SNR DEM L71 are enriched in iron. These contributions from ejecta to the integrated spectra measured with *ASCA* affect the measured LMC abundances. Six out of the seven SNRs used by Hughes et al. (1998) are well-established CC-SNRs, and this bias is likely to explain their higher [O/Fe] (or more generally [α/Fe]). On the contrary, the *XMM-Newton* sample used here is explicitly cleaned of SNRs with abnormal abundance patterns (i.e. those with ejecta detected), resulting in a purer sample better suited to the measurement of the ISM composition. However, this sample comprises SNRs fainter than used in previous studies, and the abundances thus obtained are consequently relatively uncertain.

The abundance pattern of metals should reflect the past history of chemical enrichment, and in particular the relative number of CC and Ia SNRs (hereafter N_{CC}/N_{Ia}), because their metal yields are markedly different. In Fig. 6 we show the [O/Fe] and [Mg/Fe] vs. [Fe/H] diagrams. Abundances measured with SNRs (i.e. that of the ISM gas phase) are compared with that measured in older populations: old globular clusters from Johnson et al. (2006, ages ∼ 10 Gyr) and Bar and disc field red giant stars from Van der Swaelmen et al. (2013, ages $\gtrsim$ 1 Gyr). SNRs are only found in the higher metallicity ([Fe/H]) range. There is also a clear trend for SNRs to be at lower [α/Fe] ratios, although uncertainties from X-ray spectral fitting are large (particularly for [Mg/Fe]). A larger sample and more data would be desirable to demonstrate this result definitely. Nevertheless, this trend should reflect the continued enrichment by type Ia SNe in the last ∼1 Gyr, which inject large amounts of Fe back in the ISM and drive younger populations towards the bottom right corner of the [α/Fe] – [Fe/H] diagrams.

[14] They used six CC SNRs (J0453-6829, N23, N49, N49B, N63A, and N132D) and one type Ia SNR (DEM L71).

[15] Using the conventional notation: $[X/Y] = \log(X/Y) - \log(X/Y)_\odot$.

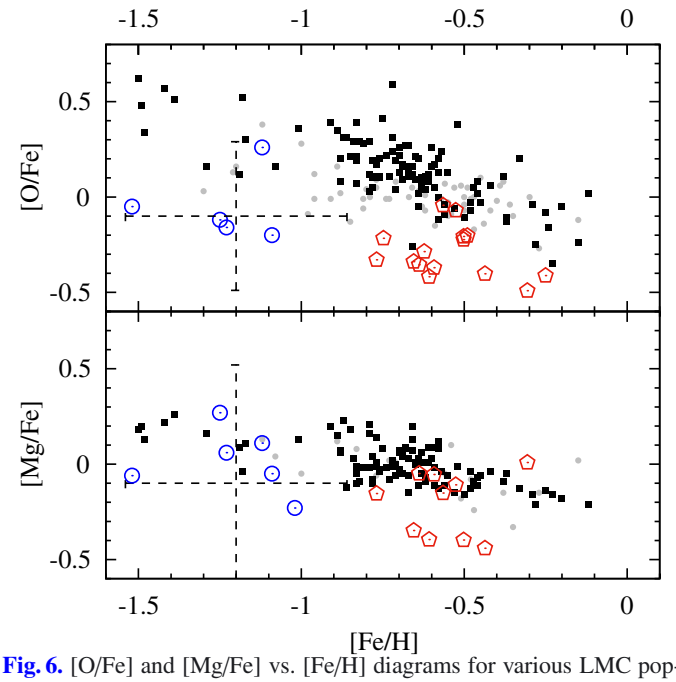

Fig. 6. [O/Fe] and [Mg/Fe] vs. [Fe/H] diagrams for various LMC populations: abundances measured in SNRs (ISM gas phase, this work) are shown with red pentagons. The crosses indicate median error bars. Blue open circles are the old globular clusters from Johnson et al. (2006, ages ∼10 Gyr). Chemical abundances of Bar and disc stars are marked by black squares and grey dots, respectively (from Van der Swaelmen et al. 2013, ages $\gtrsim$1 Gyr).

There are SNR-to-SNR variations in the abundances, but the metallicity scatter in the ISM gas phase is less than for field stars. In particular there is no metal-poor population ([Fe/H] $\lesssim -0.9$). We also checked that there is no clear correlation between the location of an SNR in the [α/Fe] – [Fe/H] diagrams and the SFH around the SNR. For instance, SNRs with relatively high [α/Fe] are not necessarily in regions with increased recent SF, which would produce massive stars that release low-Z elements. Despite the uncertainties and the limited size of the sample, this lack of correlation likely indicates that SNe-produced elements are well mixed in the ISM. In other words, the ISM is quickly homogenised, at least at the spatial scales over which SFH is measured (∼200 pc).

After LMC abundances were measured (e.g. Russell & Dopita 1992), Tsujimoto et al. (1995) found with chemical evolution models that the deficit of light α-elements of the MCs (i.e. lower [α/Fe] for a given [Fe/H]) compared to the Galaxy must be explained by a *smaller* $N_{\rm CC}/N_{\rm Ia}$ (more type Ia SNe). They measured a Galactic ratio of 6.7, but $N_{\rm CC}/N_{\rm Ia} \sim 4$–5 and ∼3.3 for the LMC and SMC, respectively. Our results for the LMC ISM abundance suggest an even lower ratio $N_{\rm CC}/N_{\rm Ia}$, because the deficit of light α-elements is wider than previously assumed by Tsujimoto et al. (1995). By tentatively typing all LMC remnants, we show in Sect. 6 that indeed $N_{\rm CC}/N_{\rm Ia}$ is particularly low, compared to previous measurements of the ratio in the LMC or inferred from galaxy cluster X-ray observations, and discuss likely explanations.

6. Measuring the ratio of CC to type Ia SNe in the LMC using "SFH-typing"

6.1. The typing of SNRs in general

Because the two flavours of SNe deposit a similar amount of energy in the ISM, they produce remnants which become increasingly hard to type as they age. The most secured typing methods are the study of SN *optical* light echoes (Rest et al. 2005, 2008; *infrared* light echoes can be used to probe the ISM dust, see e.g. Vogt et al. 2012), the measurement of the nucleosynthesis products in the ejecta (e.g. Hughes et al. 1995), or the association with a neutron star/pulsar wind nebula. Optical spectroscopy can also be used: In some cases the fast-moving ejecta are detected in optical lines with highly elevated abundances of oxygen. Those so-called *oxygen-rich SNRs* have massive star progenitors, see for instance Lasker (1978), Chevalier & Kirshner (1979), Morse et al. (1995), and references therein. On the contrary, some SNRs have prominent Balmer lines of hydrogen, but absent or weak [S II] and [O III] lines. These Balmer-dominated optical spectra are interpreted as non-radiative shocks overtaking (partially) neutral gas (Chevalier & Raymond 1978; Chevalier et al. 1980). A type Ia SN progenitor is consistent with the presence of neutral gas, as massive stars would ionise their surrounding. A sample of optically bright Balmer-dominated SNRs was detected in the LMC by Tuohy et al. (1982).

These methods work best for relatively young remnants ($\lesssim$5000 yr), leaving a significant fraction of the SNR population untyped. However, several *evolved* SNRs have been discovered (in X-rays) in the Magellanic Clouds with an iron-rich, centrally bright emission (Nishiuchi et al. 2001; Hendrick et al. 2003; van der Heyden et al. 2004; Seward et al. 2006; Borkowski et al. 2006; Bozzetto et al. 2014; Maggi et al. 2014), naturally leading to their classification as type Ia remnants.

In addition, studies of the X-ray and infrared morphologies of SNRs (Lopez et al. 2009; Peters et al. 2013) suggest that, as a class, type Ia and CC SNRs have distinct symmetries: type Ia remnants are statistically more spherical and mirror symmetric than the CC SNRs. However, this method cannot give definite results for *individual* objects: Prominent counterexamples include SNR 1E 0102.2−7219, a textbook CC SNR which is highly symmetric (Flanagan et al. 2004), and MCSNR J0547−7025, which is a type Ia SNR (based on its X-ray spectrum Hendrick et al. 2003, this work) with "anomalous" ejecta distribution (Lopez et al. 2009).

For a decent fraction of the LMC remnants, these various methods give a secured classification. This "secured-type" sample is presented in Appendix B and listed in Table A.1. To tentatively type the rest of the sample, we devise a new way to quantify the local stellar environment of LMC, as described in Sect. 6.2. This method is calibrated with the "secured-type" sample and applied in Sect. 6.3. We can then discuss the measured ratio of CC to type Ia SNRs in the LMC and its implications in Sect. 6.4.

6.2. Evaluating the local stellar environment

We devised two metrics to assess the local stellar environment of LMC SNRs. Both ultimately stem from the same set of data (the MCPS catalogue of Zaritsky et al. 2004). Although connected, they still measure two distinct properties and are therefore complementary, as we discuss below. The two metrics are given for each SNR in Table C.1.

- $N_{\rm OB}$, the number of blue early-type stars in the immediate vicinity of the remnant:
  To obtain this number, we constructed a V vs. $(B-V)$ colour–magnitude diagram (CMD) of all stars whose projected position lies within 100 pc (∼6.9′) of each SNR. This value corresponds to the drift distance for a star of age 10^7 yr at a velocity of 10 km s^{-1} and was used by

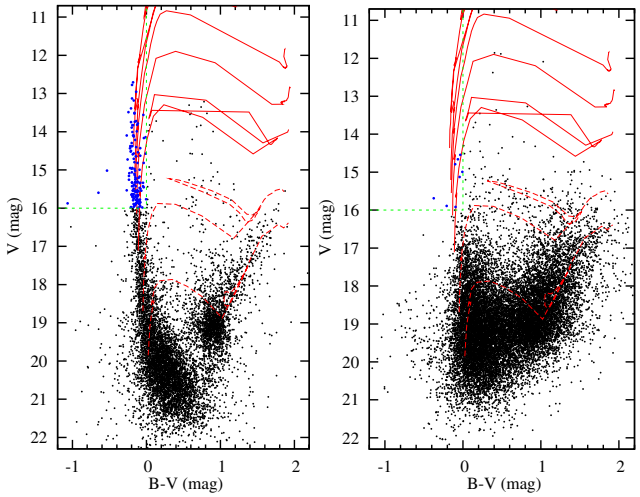

Fig. 7. Colour−magnitude diagram (CMD) of the MCPS stars (Zaritsky et al. 2004) within 100 pc (~6.9′) of the central position of two remnants, MCSNR J0528−6727 (*left*) and MCSNR J0534−6955 (*right*). Geneva stellar evolution tracks (Lejeune & Schaerer 2001) are shown as red lines, for metallicity of 0.4 $Z_\odot$ and initial masses of 3, 5 $M_\odot$ (dashed lines) and 10, 15, 20, 25, and 40 $M_\odot$ (solid lines), from bottom to top. The green dashed line shows the criteria used to identify the OB stars ($V < 16$ and $B - V < 0$). Stars satisfying these criteria are shown as blue dots.

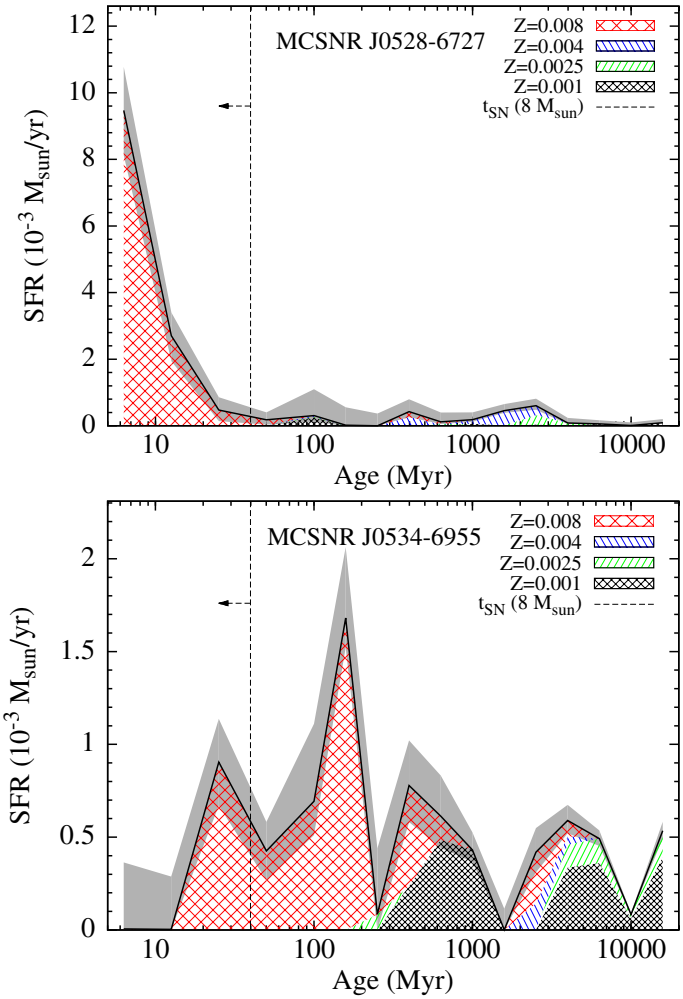

Fig. 8. Star formation history around MCSNR J0528−6727 (*top*) and J0534−6955 (*bottom*). Data are taken from Harris & Zaritsky (2009). The star formation rate in four metallicity bins are plotted against look-back time. The errors (combining all metallicities) are shown by the grey shading. The vertical dashed line at 40 Myr indicates the maximal lifetime of a CC SN progenitor. Note the changing vertical scale.

Chu & Kennicutt (1988). The upper main-sequence of stars in the LMC was identified by adding the stellar evolutionary tracks of Lejeune & Schaerer (2001), for $Z = 0.4\ Z_\odot$ and initial masses from 3 $M_\odot$ to 40 $M_\odot$. We assumed a distance modulus of 18.49 and an extinction $A_V = 0.5$ (the average extinction for "hot" stars, Zaritsky et al. 2004). From there, we used the criteria of $V < 16$ and $B - V < 0$ to identify OB stars. In Fig. 7 we show two example CMDs of the regions around MCSNR J0528−6727 (left) and MCSNR J0534−6955 (right). In the former case, a prominent upper-main sequence is obvious and the number of OB stars $N_{\rm OB} = 142$. By contrast, the region around MCSNR J0534−6955 is devoid of young massive stars. For this remnant, $N_{\rm OB}$ is only 8. Note that $N_{\rm OB}$ is likely a lower limit on the actual number of massive stars due to stellar crowding (the typical seeing of the MCPS is 1.5″). This issue affects chiefly regions with higher $N_{\rm OB}$.

- $r = N_{\rm CC}/N_{\rm Ia}$, the ratio of CC SNe to thermonuclear SNe expected from the observed distribution of stellar ages in the neighbourhood of the remnants:
  This number is obtained via the spatially resolved SFH map of Harris & Zaritsky (2009, see Sect. 2.3). For each SNR we plot the SFR of the cell including the remnant as a function of lookback time and metallicity. Two example SFHs are shown in Fig. 8 for the same SNRs of Fig. 7. They are strikingly different: the SFR around J0528−6727 soared in the last 20 Myr, when the numerous early-type stars in the vicinity of the remnant were formed, while the star formation around J0534−6955 peaked (at a lower absolute rate) about 125 Myr ago and was shut down in the most recent 20 Myr.

Because stars might drift away from their birth place, one potentially important caveat is that the SFH of a cell hosting an SNR may be derived from stars having no physical connection with the SNR progenitor. For a detailed discussion on the relevance of local stellar populations to the study of progenitors, we point to Badenes et al. (2009). However, we stress that most of the information that can be gained from the study of the local SFHs, in the context of typing remnants, is contained in the most recent time bins. Namely, the presence of recent star formation episode is a strong necessary (but not sufficient) condition to tentatively type a remnant as having a CC origin. Conversely, the lack of recent star-forming activity favours a thermonuclear origin.

To approach this question in a quantitative way, we did the following: We used the delay time distribution (DTD) $\Psi_i(\tau)$, the SN rate at time τ following a star formation event, measured by Maoz & Badenes (2010) in the Magellanic Clouds, with $i = 1$, 2, and 3 designating the time intervals they used ($t < 35$ Myr, 35 Myr $< t <$ 330 Myr, and 330 Myr $< t <$ 14 Gyr, respectively). From timescale arguments it is reasonably assumed that Ψ_1 will correspond to the CC-SN rate, whilst Ψ_2 and Ψ_3 will be that of SNe Ia (regardless of their "prompt" or "delayed" nature). The SFR is integrated to obtain M_i, the stellar mass formed in each time interval. The SFH of Harris & Zaritsky (2009) is only given at $t = 25$ Myr and $t = 50$ Myr. To obtain M_1, the mass formed at $t < 35$ Myr, we approximate $M(25 < t < 35)$ as half that formed between 25 Myr and 50 Myr (the second half is included in M_2).

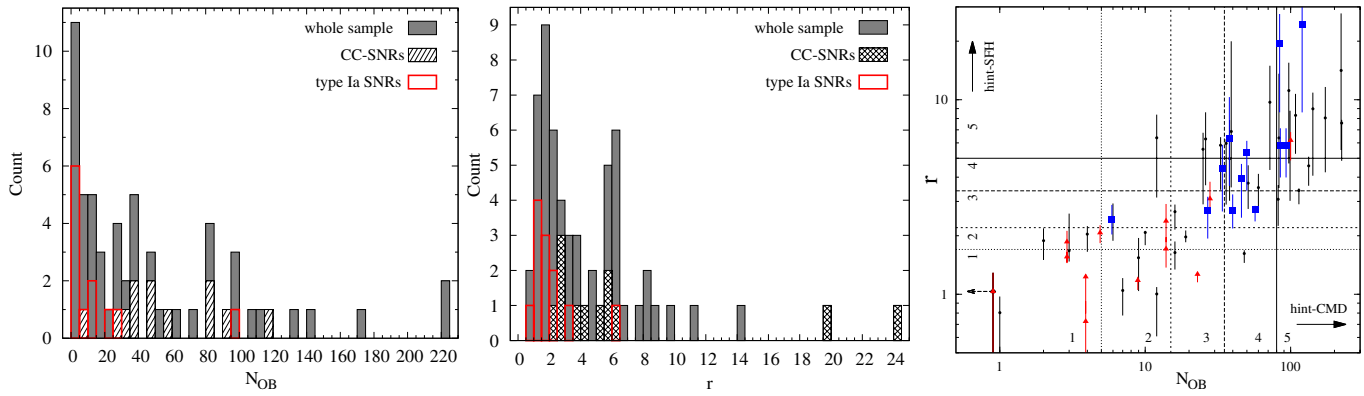

Fig. 9. *Left and middle panel*: count distribution of LMC SNRs as function of N_{OB} and r. The distribution for the SNRs with a secured CC classification is shown with the hatched boxes; that for type Ia SNRs is outlined in red. The whole sample is shown by the solid grey histograms. *Right panel*: r–N_{OB} diagram of LMC SNRs. Secured Ia and CC SNRs are marked by red triangles and blue squares, respectively; the rest of the sample is shown with black dots. The arrow in the lower left corner indicates an SNR with $N_{OB} = 0$. The regions corresponding to different "Hint-SFH" and "Hint-CMD" are marked by the gridding.

Likewise, we split the mass formed between $t = 250$ Myr and $t = 400$ Myr in two and include a half in both M_2 and M_3.

Then, we compute $r = N_{CC}/N_{Ia}$ as the ratio of the *rates* of CC and Ia SNe, since the visibility times are the same for both types, i.e.:

$$r = \frac{\Psi_1 M_1}{\Psi_2 M_2 + \Psi_3 M_3}. \quad (2)$$

Over the visibility time of a remnant – taking 100 kyr as a very conservative limit – the stars in the SFH cell including the remnant will not drift away. In other words, the distribution of stellar ages observed *now* is the same as that when the SN exploded. r is therefore a measure of the relative size of the pool of possible progenitors of both types. Using the same example SNRs as in Fig. 8, a value of $r = 9.0^{+1.9}_{-4.9}$ is obtained for J0528−6727[16] while for J0534−6955 it is only $r = 1.2 \pm 0.1$.

6.3. "SFH-typing" all LMC SNRs

We now proceed to give a tentative type to the whole sample of SNRs in the LMC, using N_{OB} and r. We assign two numbers called "Hint–CMD" and "Hint–SFH", depending on the N_{OB} and r-value obtained for each SNR, respectively. The numbers range from 1 meaning "strongly favours a type Ia SN origin", to 5 meaning "strongly favours a CC-SN origin". We used the distribution of N_{OB} and r for the sample of "secured-type" SNR to establish the correspondence between their values and the hints.

This method is conceptually similar to that used by Chu & Kennicutt (1988), albeit with several improvements: firstly, the sample in this work is twice the size of that available to Chu & Kennicutt. Secondly, many (~25) SNRs have now a secured type (Appendix B) and can be used to calibrate the method and evaluate the rate of erroneous classification. Then, the completeness of the census of early-type stars in the vicinity of the remnants is higher, owing to the use of the MCPS catalogue. Finally, the spatially-resolved SFH reconstruction was simply unavailable before Harris & Zaritsky (2009).

[16] The uncertainty given for r solely includes that of the mass formed M_i, which is computed from uncertainties of the SFR given in Harris & Zaritsky (2009). The uncertainties on Ψ_2 and Ψ_3 are larger, but are the same for all SNRs in the sample, allowing the use of r in a comparative fashion. we adopted $\Psi_2 = 0.26$ SNe yr^{-1} $(10^{10}\ M_\odot)^{-1}$ and $\Psi_3 < 0.0014$ SNe yr^{-1} $(10^{10}\ M_\odot)^{-1}$. Note that because Ψ_3 is an upper limit, r is formally a lower limit.

Table 6. Criteria and "Hints" attributed to SNRs as function of N_{OB} and r.

Value	Hint-CMD	Hint-SFH	Meaning
1	$N_{OB} < 5$	$r < 1.7$	Strongly favours a type Ia
2	$5 \le N_{OB} < 15$	$1.7 < r < 2.2$	Moderately favours a type Ia
3	$15 \le N_{OB} < 35$	$2.2 < r < 3.4$	Undecided
4	$35 \le N_{OB} < 80$	$3.4 < r < 5$	Moderately favours a CC
5	$80 \le N_{OB}$	$5 < r$	Strongly favours a CC

Calibration of the "SFH-typing": the number of OB stars in the vicinity of the secured type Ia and CC SNRs is shown in Fig. 9 (left panel). The two samples are rather well separated: the majority of type Ia SNRs have less than 20 early-type stars in their neighbourhood, while most of the CC-SNRs have $N_{OB} > 30$. The single major type Ia outlier is N103B ($N_{OB} = 99$), which is known to be in a region with a vigorous recent star formation activity (e.g. Badenes et al. 2009). MCSNR J0453−6829 is the only CC-SNRs to have a moderate N_{OB} (<25). The choice of "Hint-CMD" is given in Table 6 to reflect this distribution: N_{OB} less than 5 (less than 15) strongly (moderately) favours a type Ia classification, while N_{OB} in excess of 80 (35) strongly (moderately) favours the CC-SN case.

Intuitively, any value $r > 1$ should favour a CC SN origin (conversely for a thermonuclear origin). However, an important caveat in interpreting r is that the rates of Maoz & Badenes (2010), especially Ψ_2 and Ψ_3, are quite uncertain, due to the still limited sample of SNRs. Specifically, Ψ_2 has a value that changes by a factor of four depending on the tracer used to constrain the SNR visibility time. To provide a better feeling on what r-value to expect in either case (and to decide where is the separation), we show the count distribution of secured type Ia and CC SNRs in the r-domain in Fig. 9 (middle panel). There is a stronger overlap of both types in the intermediate range ($2.2 \lesssim r \lesssim 3.5$) than with N_{OB}. However, the lower end ($r < 2.2$) still includes most of the type Ia SNRs, without contamination by the other type. N103B is again the only outlier at $r = 6.2$; at

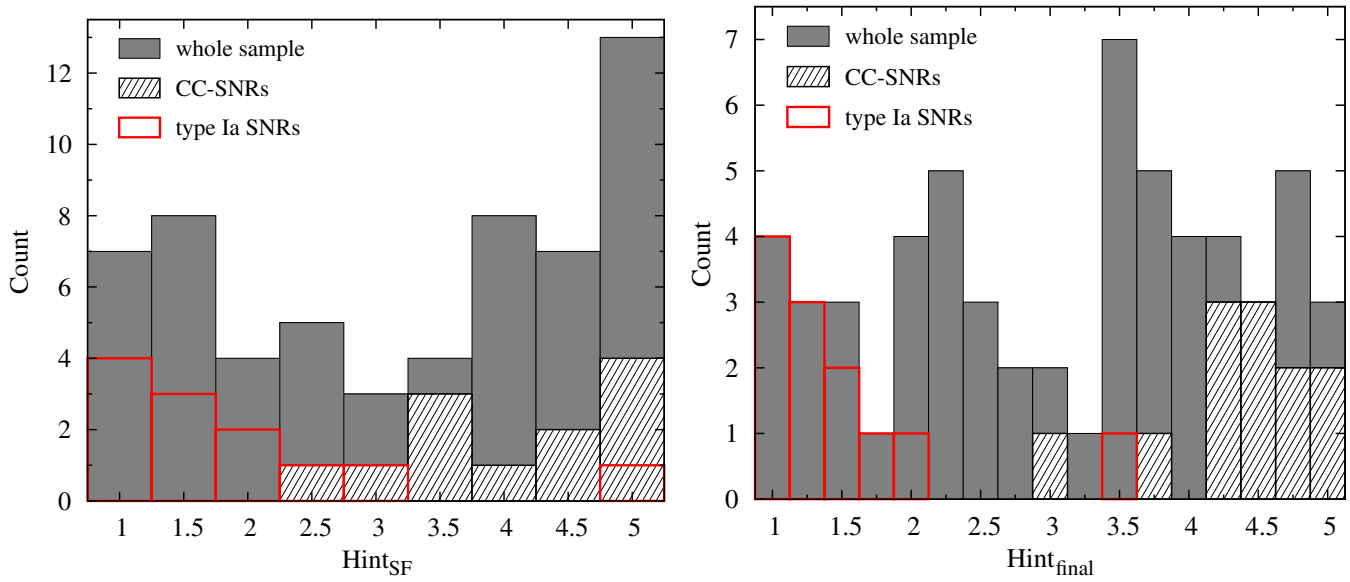

Fig. 10. *Left*: count distribution of the LMC SNRs as function of "Hint-SF", combining N_{OB} and r. *Right*: count distribution of the LMC SNRs as function of "Hint–final", combining spectral *and* SFH information (see text for details). Hatching and colours as in Fig. 9.

$r > 3.4$ only CC-SNRs are found. In view of this observed distribution, the ratio $r = N_{CC}/N_{Ia}$ is still a useful tool to assign a type to SNRs using the observed local SFH, and should be valid in a comparative and statistical sense. The "Hints-SFH" attributed to the sample based on r are listed in Table 6. r and N_{OB} are also displayed as a scatter plot for secured Ia and CC SNRs (right panel of Fig. 9). There, the regions corresponding to different "Hints" are marked.

Caveat on the complementarity of N_{OB} and r: it is clear that the two metrics are connected. Both are based on the MCPS catalogue; the early-type stars detected in a cell drive the fitting of the most recent time bins in the SFH reconstruction of Harris & Zaritsky (2009). However, the r-value of a cell can be moderate even though N_{OB} is high, as evident from the scatter along the horizontal axis in Fig. 9 (right panel). That is because r is a *relative* measure of the recent SFR compared to that at earlier epochs, while N_{OB} gives a measure of the *absolute* strength of the recent star formation. In the (high N_{OB}– moderate r) case, there are many available progenitors of both CC- and type Ia SN; these are typically cases where the classification is inconclusive.

Results for the whole sample: the count distributions for all LMC SNRs in the N_{OB} and r spaces are shown in Fig. 9 (grey histograms, left and middle panels), and as a scatter plot in the right panel. They are similar, with larger numbers, to the distributions of the secured-type SNRs. About twenty remnants are in regions with a low number of early-type stars ($N_{OB} < 15$) and not dominated by recent SF ($r \lesssim 2$). There is a peak at $r \sim 6$ with a dozen remnants. Those are SNRs in star-forming regions which are widely spread across the LMC. They are often associated with giant H II complexes (e.g. LHA-120 N4, N11, N44). The objects with extreme values for r ($\gtrsim$8) also have the largest N_{OB}. Those are located in the two most intensively star-forming regions of the LMC: 30 Doradus, and the rim of the supergiant shell LMC 4 (which embeds the "Constellation III" region, Harris & Zaritsky 2008, 2009).

To combine the two "Hints" into one, we computed the arithmetic mean of Hint-CMD and Hint-SFH. The resulting "star-formation Hint" (Hint-SF) again ranges from 1 to 5. Its distribution for the whole sample and the secured-type SNRs is shown in Fig. 10. There are 19 remnants with Hint-SF ≤ 2; they most likely all result from a type Ia SN. We call this sample "likely-Ia". Likewise, the 28 objects above Hint-SF ≥ 4 are probably most of the CC-SNR population. They form the "likely-CC" sample.

The single type Ia SNR contaminating the sample (N103B) allows estimating a false-positive rate of 5%−10%. The false-positive rate of the "likely-Ia" sample is probably lower: the massive stars formed at (roughly) the same time as the progenitor of a CC-SN can hardly be missed by photometric survey, because they would form the bright end of the population.

There are 12 SNRs in between $2.5 \leq \text{Hint}_{SF} \leq 3.5$, for which the local stellar environment cannot be used to decisively type the origin; they form the "SFH-untyped" sample. Interestingly, two and five of these remnants can be classified from other indicators as type Ia (the iron-rich MCSNR J0508−6830 and DEM L71) or CC-SNRs (e.g. the oxygen-rich N132D or MCSNR J0453−6829, which hosts a PWN), respectively.

Including the spectral results for typing purpose The spectral analysis of Sect. 5 revealed the presence of ejecta-enhanced plasma in almost half of the sample (Tables 3 and E.2). One should take advantage of this for the typing of the remnant, in combination with the SFH-based method we just presented. We assign another number, "Hint-spec", which depends on the high- or low-abundance flags of each SNR (Sect. 5.5). The numbers range from 1 (strongly favouring a type Ia origin) if "low X/Fe" flags are raised (i.e. the SNR is iron-rich), to 5 (strongly favouring a CC origin) when "high X/Fe" flags are raised (i.e. CC nucleosynthesis pattern is detected).

The choice of "Hint-spec" is given in Table 7. Note that a bigger impact is given to the low or high O/Fe ratio, as these elements are the most abundant. Therefore, this ratio is easier to fit, more reliable, and sometimes the only one available. A value of 5 is also attributed to remnants where a pulsar/PWN is

Table 7. "Hint-spec" attributed to SNRs as function of spectral results.

Hint-spec	Criteria
1	at least three "low X/Fe" flags, no "high X/Fe" flag
1.5	two "low X/Fe" flags or low O/Fe, no "high X/Fe" flag
2	one "low X/Fe" flag (except O/Fe), no "high X/Fe" flag
2.5	low Si/Fe, no "high X/Fe" flag
3	ISM abundances, unfitted abundances, or no *XMM-Newton* data
3.5	high Si/Fe, no "low X/Fe" flag
4	one "high X/Fe" flag (except O/Fe), no "low X/Fe" flag
4.5	two "high X/Fe" flags or high O/Fe, no "low X/Fe" flag
5	at least three "high X/Fe" flags, no "low X/Fe" flag; pulsar/PWN detected

detected in the remnant. The values of "Hint-spec" for each SNR are given in Table C.1. We combined "Hint-SF" and "Hint-spec" by taking their arithmetic mean. The distribution of the resulting "Hint-final" is shown in Fig. 10 (right panel). The contamination (i.e. misclassification of N103B) is slightly alleviated, while a better separation of the "secured-type" SNRs is evident. There are 23 SNRs with "Hint-final" $\leq$ 2.5 which are likely of type Ia, and 31 SNRs where "Hint-final" $\geq$ 3.5 which are likely attributed to CC, although N103B (Hint-final = 3.5) is still contaminating the sample. There are five sources with inconclusive "Hint–final", including one secured-CC (N23).

6.4. Ratio of CC to type Ia SNe and implications

The observed number of SNRs of both types provides a measurement of the ratio of CC to type Ia SNe that exploded in the LMC over the last few 10^4 yr, i.e. very close to the current ratio of CC/Ia SN *rates*. Based on the "star formation Hint", the numbers of SNRs in the "likely Ia" and "likely CC" samples translate in $N_{\rm CC}/N_{\rm Ia}$ = 1.47 (28/19). Assuming all "SFH-untyped" SNRs which do not have a secured type are of type Ia then the ratio $N_{\rm CC}/N_{\rm Ia}$is 1.27 (33/26). Conversely, if the 'SFH-untyped" are all CC, the ratio is 1.81 (38/21). Even correcting for N103B, $N_{\rm CC}/N_{\rm Ia}$is conservatively in the range 1.2 to 1.8.

Including the spectral results (detection of ejecta in X-rays), we have a ratio $N_{\rm CC}/N_{\rm Ia}$ = 1.35 (31/23). Correcting for N103B and N23 (with wrong and uncertain classifications), the ratio CC:Ia based on SFH *and* X-ray spectroscopy is between 1.11 (31/28) and 1.46 (35/24), depending on the type assigned to the remaining four objects. This range is compatible with that derived from the "SFH-typing" alone, albeit narrower because of the greater amount of information included in the calculation.

This ratio can be compared to two kinds of measurements: first, to the observed ratio of current rates, obtained from SNe search. For instance, Li et al. (2011) measured a ratio of about 3:1 in a volume-limited sample. Second, to the ratio $N_{\rm CC}/N_{\rm Ia}$ derived from intracluster medium (ICM) abundances. Galaxy clusters retain all the metals produced by SNe. The X-ray spectrum of the ICM reveals the elemental abundances, which are used to constrain the *time-integrated* numbers of CC and Ia SNe. From *Suzaku* observations of a small sample of clusters and groups of galaxies, Sato et al. (2007) estimated $N_{\rm CC}/N_{\rm Ia} \sim 3.5$ (ranging between 2 and 4, depending on the type Ia SN model assumeds). With *XMM-Newton* and a larger cluster sample, de Plaa et al. (2007) measured a $N_{\rm CC}/N_{\rm Ia}$ between 1.7 and 3.5, again depending on the adopted SN Ia models. However, none of the explored SN models could reproduce the Ar/Ca ratio. Lovisari et al. (2011) derived $N_{\rm CC}/N_{\rm Ia} \sim$ 1.5−3. Therefore, the current ratio of CC/Ia SNe in the LMC is significantly lower than that measured in local SN surveys and in galaxy clusters.

One possible caveat could be that we are missing CC-SNRs. For instance, SNe exploding in superbubbles (SBs, see e.g. Chu 2008, for a review) will not be directly recognised as SNRs. Wang & Helfand (1991) and Dunne et al. (2001) found a dozen LMC SBs with an X-ray luminosity, measured with *Einstein* and ROSAT, brighter than theoretically expected for a wind-blown bubble, and possibly energised by interior SNRs. The limited spatial resolution of the instruments used may result in *distinct* SNRs to have been overlooked and the X-ray emission of the SB overestimated (e.g. MCSNR J0523−6753, near the H II region/SB N44 in Wang & Helfand 1991, see also Jaskot et al. 2011). With a dozen extra CC SNRs, the ratio $N_{\rm CC}/N_{\rm Ia}$ is pushed to ∼1.5−2. However, the number of type Ia SNRs currently known in the LMC is also expected to be below the actual number (see Sect. 7 for a discussion on sample completeness). Therefore, it is unlikely that the ratio $N_{\rm CC}/N_{\rm Ia}$ is significantly underestimated. Furthermore, the abundance pattern of the LMC, with its low [α/Fe] (Sect. 5.6), lends support to such a low $N_{\rm CC}/N_{\rm Ia}$. This should be lower than the value of $N_{\rm CC}/N_{\rm Ia}\sim$ 4−5 estimated by Tsujimoto et al. (1995) using metallicity alone.

The low $N_{\rm CC}/N_{\rm Ia}$ ratio measured in the LMC therefore has to be a consequence of the different SFH of the Cloud compared to that in other nearby galaxies or galaxy clusters. The local SN rates depend on the summed SFH of galaxies included in the SN surveys. The higher ratio measured by e.g. Li et al. (2011) simply indicates that many star-forming galaxies are included in the local volume explored. The SFHs of galaxy clusters are relatively simple, with short episodes of star-formation at a redshift of $z \sim 3$ (Eisenhardt et al. 2008), so that the integrated numbers of type Ia and CC SNe inferred from X-ray observations correspond to the fractions of stars formed that end their lives as SN of either type.

In the LMC, star formation occurred during several episodes. In addition to many regions with recent or ongoing star formation where, unsurprisingly, the CC-SNRs are found (see Sect. 8), the LMC had enhanced star formation episodes 100 Myr, 500 Myr, and 2 Gyr ago as well (Harris & Zaritsky 2009). The SN Ia DTD follows fairly well a t^{-1} power law for delays $t > 1$ Gyr, and appear to keep increasing below 1 Gyr (for a review of SN Ia DTD measurements, see Maoz & Mannucci 2012). The majority of type Ia SNe explode within 2 Gyr after star-forming episodes. We are therefore coincidentally observing the LMC at a time when the rate of type Ia SN from the stellar populations formed 500 Myr to 2 Gyr ago is high. Integrated over an SNR lifetime (a few 10^4 yr), it results in the relatively large number of type Ia SNRs. It is not possible to use $N_{\rm CC}/N_{\rm Ia}$ to estimate η, the fraction of stars that eventually explode as Ia SNe (Maoz 2008), because of the complex SFH of

the LMC: stars exploding now (as either SN types) were created at different epochs. Furthermore, η is also dependent on the initial mass function (IMF), over which one has little freedom, since the SFH-reconstruction already assumes a particular form (the Salpeter IMF).

Currently, the only other galaxy with which to compare the N_{CC}/N_{Ia} of the LMC is the SMC. In our own Milky Way, there remain too many untyped SNRs. More problematic are the distance uncertainties and line-of-sight confusion that prevent associating remnants to regions of star formation (e.g. spiral arms). In the Local Group (M31, M33) and beyond (e.g. M83, Dopita et al. 2010), the problem is again the lack of secured typing methods, and generally the absence of spatially resolved SFH. The situation is likely to improve in the near future with more sensitive X-ray observatories (e.g. *Athena*), and large observing programmes of M31 and M33 with *Hubble* which allow SFH maps to be built (so far, this was done in the few archival field available, Jennings et al. 2012, 2014). The SMC is the only obvious target remaining where a similar study can be currently performed, although the smaller sample of SNRs and inclination of the galaxy (and corresponding line-of-sight confusion) might complicate direct comparisons to the LMC.

7. X-ray luminosity function of SNRs in the Local Group

X-ray luminosity functions (XLFs) are valuable tools for the study of X-ray sources and comparisons between populations. The *XMM-Newton* dataset is ideally suited to derive the XLF of LMC SNRs. Out of the 59 objects in the sample, *XMM-Newton* covered 51 of them, to which we fitted spectral models (Sect. 5). For all these, the X-ray fluxes in various bands are obtained from the best-fit models (Tables E.1 and E.2) with the XSPEC command `flux`. The final results are presented in the "broad" band, from 0.3 keV to 8 keV (the effect of including the high-energy part is very minor and discussed below).

Three SNRs have been covered with *Chandra* but not *XMM-Newton*: for MCSNR J0454−6713 (N9), we used the spectral results of Seward et al. (2006) to measure the flux. MCSNR J0459−7008 (N186D) was covered in the *Chandra* observation of the SB DEM L50. Jaskot et al. (2011) published the results from these data. We used their best-fit NEI model for the SNR emission, which is spatially resolved from the SB, to derive the X-ray flux. Finally for MCSNR J0550−6823, we used the spectral parameters given in the entry of the *Chandra* SNR catalogue[17].

Two SNRs have neither *XMM-Newton* nor *Chandra* observations available, but were covered with ROSAT. Williams et al. (1999b) present a spectral analysis of MCSNR J0455−6839 (in N86). We obtained the X-ray flux of the SNR using their best-fit model. MCSNR J0448−6700 corresponds to the ROSAT PSPC source [HP99] 460, with a count rate of 1.41×10^{-2} cts s^{-1} (Haberl & Pietsch 1999). With the multi-mission count rate simulator WebPIMMS[18], we calculated the flux in several energy bands for various temperatures of an APEC model, assuming a total absorbing column $N_H = 7 \times 10^{20}$ cm^{-2} towards the source and a mean abundance of 0.4 solar. The observed hardness ratios could be reproduced for $kT = 0.97$ keV. These spectral parameters and normalisation can be converted into fluxes in the same bands as used for the rest of the sample.

In total, 56 objects have well-defined X-ray fluxes and make it into the XLF. The adopted values are listed in Table C.1. Only three SNRs have no X-ray data available. The cumulative XLF is shown in Fig. 11. The sample spans almost four orders of magnitude in luminosity, from the brightest (N132D) at $L_X = 3.15 \times 10^{37}$ erg s^{-1} down to $\sim 7 \times 10^{33}$ erg s^{-1}. The L_X used is the observed value, uncorrected for (LMC) absorption, because the fitted column densities can be quite uncertain, in particular in the faint end. We checked the $N_{H\,LMC}$-corrected XLF and found no significant variations in its shape compared to that of Fig. 11, except the shift to higher L_X.

SNR XLF from other Local Group galaxies: the LMC XLF can be best compared to other Local Group galaxies such as M31, M33, and the SMC. Sasaki et al. (2012) studied M31 SNRs and candidates identified in the *XMM-Newton* Large Programme survey of the Andromeda galaxy (Stiele et al. 2011). They converted EPIC count rates into 0.35 keV−2 keV luminosities assuming a thermal (APEC) spectrum with $kT = 0.2$ keV, $N_{H\,M31} = 10^{21}$ cm^{-2}, and $N_{H\,MW} = 0.7 \times 10^{21}$ cm^{-2}. The quoted values, however, are corrected for $N_{H\,MW}$, while for the LMC we give the observed luminosities. For consistency with the LMC XLF, we re-included $N_{H\,MW} = 0.7 \times 10^{21}$ cm^{-2} in the results of Sasaki et al. (2012) and converted the luminosity in the 0.3 keV−8 keV by scaling their L_X by 0.577 (a factor derived from simulating their assumed spectrum with and without $N_{H\,MW}$). Note that the effect of the foreground absorption should be very minor, since $N_{H\,MW}$ values are very similar in the directions of M31, M33, and the LMC ($5-7 \times 10^{21}$ cm^{-2}). 26 objects were confirmed SNRs in Sasaki et al. (2012), and another 20 were candidate SNRs.

Long et al. (2010) present a large catalogue of 82 confirmed SNRs in M33, based on the *Chandra* ACIS survey of M33 (ChASeM33, Tüllmann et al. 2011). They give L_X in the 0.35 keV−2 keV band, converted from ACIS count rates, assuming a thermal plasma at 0.5 solar, $kT = 0.6$ keV, and total $N_H = 10^{21}$ cm^{-2} (i.e. the spectrum found for the brightest source). We obtained the corresponding 0.3 keV−8 keV luminosity by scaling up the values of Long et al. (2010) by 4%.

Recently, Williams et al. (2015) published the results of a deep *XMM-Newton* survey of M33 with a larger coverage than ChASeM33, up to the D_{25} isophote of the galaxy. They recovered most of the SNRs of Long et al. (2010), except in the central region where source confusion is an issue for *XMM-Newton*, and detected or confirmed eight new SNRs, including three sources far in the outskirts of M33. We converted the unabsorbed 0.2−4.5 keV EPIC flux of the new inclusions of Williams et al. (2015), obtained assuming a power-law spectrum, to the 0.3−8 keV luminosity for the same spectrum as the SNRs of Long et al. (2010). The final, concatenated list of M33 SNRs thus comprises 90 objects.

Converting count rate to luminosity in different energy bands assuming a single temperature might affect the slope of the XLF. For instance, from a count rate in the 0.35 ke−2 keV band, the luminosity in the broad band is 25% higher with $kT = 0.6$ keV than if it is 0.2 keV. The two studies have limited knowledge of the actual spectrum of each remnant, because the larger distances prohibit more complex spectral fits, and they have to assume a particular spectrum, regardless of luminosity. This is not the case in the LMC. We indeed found a trend for brighter remnants to have higher plasma temperatures (Sect. 5.1). Quantitatively,

[17] Maintained by Fred Seward: http://hea-www.cfa.harvard.edu/ChandraSNR/index.html

[18] http://heasarc.gsfc.nasa.gov/cgi-bin/Tools/w3pimms/w3pimms.pl

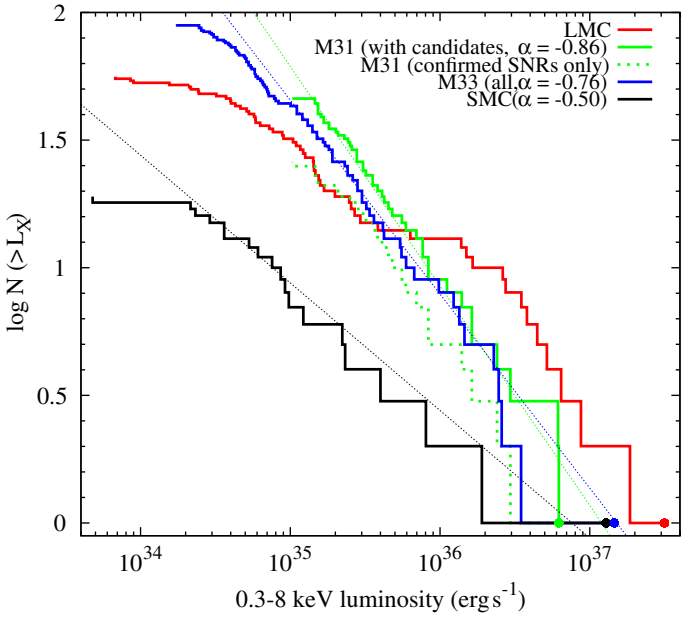

Fig. 11. Cumulative X-ray luminosity function of SNRs in Local Group galaxies. See text for details and references on how L_X was measured for each sample. The brightest SNR in each galaxy is marked by a dot. The thin dotted lines are nonlinear least-square fits of a power law ($N(>L_X) \propto L_X{}^{\alpha}$). Slopes α are given in the legend. These fits are only used to characterise the slopes and illustrate the differences between galaxies; they do not represent a physical fit of the population.

the median temperatures are $kT = 0.31$ keV for luminosities less than 10^{35} erg s^{-1}, 0.55 keV between 10^{35} erg s^{-1} and 10^{36} erg s^{-1}, and 0.8 keV above 10^{36} erg s^{-1}. The luminosities of M31 SNRs were given assuming $kT = 0.2$ keV; we scaled the 0.3 keV−8 keV luminosity up by 1.05, 1.20, and 1.35 for sources with $L_X < 10^{35}$, $10^{35} < L_X < 10^{36}$, and $L_X > 10^{36}$ erg s^{-1}, respectively. M33 SNRs were assumed to have a higher temperature (0.6 keV), which means that the luminosity of objects below $\sim 10^{35}$ erg s^{-1} was overestimated by about 15%, while for those above 10^{36} erg s^{-1} it was underestimated by ∼8%. Correcting for this effect ensures a meaningful comparison between M31, M33, and the LMC.

The SMC SNR population is comparatively smaller. van der Heyden et al. (2004) presented an X-ray spectral analysis of all SNRs in the SMC known at that time. We used their best-fit models to measure the observed (i.e. absorbed) X-ray luminosity in the same 0.3 keV−8 keV band[19], except for IKT 16. For this SNR we used results from Owen et al. (2011), which included more data from subsequent *XMM-Newton* observations. Three additional SNRs were covered with *XMM-Newton*; the results were published in Filipović et al. (2008), from which we borrowed the best-fit spectral models. The latter study also reported a new SNR, HFPK 334. For this one, we used the best-fit model from Crawford et al. (2014), which combined *XMM-Newton* and *Chandra* observations. Also included is the SNR XMMU J0056.5−7208 identified during the SMC survey (Haberl et al. 2012b; Sturm 2012). Finally, the Be/X-ray binary pulsar SXP 1062 was found to be associated to an SNR, of which it is most likely the progenitor (Hénault-Brunet et al. 2012). The thermal emission from the SNR was studied by Haberl et al. (2012c). This sample of 19 SMC SNRs is the most up to date.

[19] The luminosity given in van der Heyden et al. (2004), Table 3, for IKT 22 (1E0102−7219, the brightest SMC SNR) was mistyped. Instead of the 150×10^{27} W, it should read 1500×10^{27} W (1.5×10^{37} erg s^{-1}).

Comparative study of SNR XLFs: the cumulative XLFs of M31 and M33 in the 0.3 keV−8 keV band, corrected for the $kT - L_X$ trend, are shown along that of the SMC and LMC in Fig. 11. In terms of depth, the LMC XLF dominates. There is a single SNR at $L_X < 2 \times 10^{34}$ erg s^{-1} in M33 and in the SMC, but the bright interior pulsar in the SMC case (SXP 1062) makes the measurement of the thermal emission luminosity uncertain. In contrast, there are eight SNRs with $L_X \lesssim 2 \times 10^{34}$ erg s^{-1} in the LMC, of which seven were discovered or confirmed thanks to *XMM-Newton* observations.

In terms of number, the largest population so far is found in M33 (90 SNRs in X-rays), probably owing to the depth of the *Chandra* survey (using 100 ks pointings) in the central 15′, the overlap with a deep *XMM-Newton* survey up to the D_{25} isophote, and the favourable (face-on) orientation of M33. However, the population of M31 SNRs is larger than any other at $L_X \lesssim 5 \times 10^{35}$ erg s^{-1} and is only limited by the depth of the survey ($\sim 10^{35}$ erg s^{-1}). The ratio of M31-to-M33 SNRs in the 10^{35}−10^{36} erg s^{-1} range is at most 1.5, i.e. substantially smaller than the mass ratio of the galaxies (10–20, Corbelli 2003; Peñarrubia et al. 2014). This shows the effect of the higher (recent) SFR in M33 compared to M31 (0.45 $M_\odot$ yr^{-1} vs. 0.27 $M_\odot$ yr^{-1}, Verley et al. 2009; Tabatabaei & Berkhuijsen 2010) leading to a larger production of CC SNRs in M33. In the same luminosity range, the number of LMC SNRs is comparable to that in M33. This is expected because the LMC is only slightly less massive than M33. Furthermore, the recent SFR of the LMC is high, 0.3–0.4 $M_\odot$ yr^{-1} in the last 40 Myr (Harris & Zaritsky 2009). This conspires with the high current type Ia SN rate (Sect. 6.4) to build up the large population of SNRs in the LMC. Finally, the "feather-weight" SMC (about ten times less massive than the LMC, (Stanimirović et al. 2004; Harris & Zaritsky 2006) has a smaller, yet decent population of remnants, likely owing to its recent star formation activity (0.08−0.3 $M_\odot$ yr^{-1}, Harris & Zaritsky 2004).

In terms of shape, the XLF of M31 SNRs is the most uniform, following a power law ($N(>L_X) \propto L_X{}^{\alpha}$) with $\alpha = -0.86 \pm 0.04$ down to $\sim 2 \times 10^{35}$ erg s^{-1}. This holds with or without including the candidates, which means that most are indeed bona-fide SNRs. The M33 remnants follow mostly the same distribution, with $\alpha = -0.76 \pm 0.05$. Towards the faint end, the M33 XLF flattens and diverges from the power law below 10^{35} erg s^{-1}, indicating incompleteness. Long et al. (2010) concluded that no SNR brighter than 4×10^{35} erg s^{-1} was missed across the surveyed field. It is likely that they were over-conservative and that missing SNRs are only those which have luminosity below 10^{35} erg s^{-1}. The combined ChASeM33 and *XMM-Newton* surveys cover the total extent of the galaxy (Plucinsky et al. 2008; Williams et al. 2015), so the missing SNRs are either too X-ray-faint (below the surveys' detection limits), or absent/undetected at radio and optical wavelengths, precluding their identifications as SNRs.

We performed Kolmogorov-Smirnov (KS) tests to compare the different populations. Using a bootstrapping method, we produced 1000 luminosity functions from the original data. We checked that similar results were obtained when increasing that number to 10^6. Restricting the analysis to SNRs brighter than 3×10^{35} erg s^{-1} to ensure completeness of the samples, we found that the XLFs of M31 and M33 SNRs follow the same distribution at the 3σ confidence level. There was a marginal indication that the M33 distribution was steeper than that of M31 (Sasaki et al. 2012), but this difference essentially disappears once the $kT - L_X$ trend is taken into account.

In the SMC, although the population is limited to about 20 objects, the distribution is relatively uniform. The XLF is however flatter ($\alpha = -0.5 \pm 0.05$), and KS tests confirm that the SMC population is different from those of M31 and M33. This might indicate that SMC remnants evolve faster (and fade earlier) than in M31 and M33, due to a lower ISM density. The lower metallicity in the SMC (about 0.2 solar, Russell & Dopita 1992) may also participates in the lower luminosities of the SMC SNR, since the emissivity of hot plasmas is smaller for lower metallicities.

In contrast to the other galaxies, the luminosity function of SNRs in the LMC exhibits a complex behaviour and does not obey a smooth power-law distribution over most of the dynamical range. Regardless of the lower luminosity cut used, the KS tests reject the null hypothesis that LMC SNRs have the same XLF than those in M31, M33, or the SMC.

The most striking and robust result is the very prominent bright end of the LMC XLF. There are 13 SNRs with $L_X > 10^{36}$ erg s^{-1}, more than in M31 and M33. Amongst these, there are two SNRs hosting bright pulsars/PWNe and a harder non-thermal spectrum. Even restricting the XLF to the soft band or excluding these two objects, the population of bright LMC SNRs is still above the other ones. This bright population is not a clearly distinct group. In particular, it is not made up of remnants from only one SN type. There are four type Ia SNRs and nine CC-SNRs, so the N_{CC}/N_{Ia} ratio is higher than overall (Sect. 6.4), but not exceedingly so. Higher luminosities are expected from SNRs interacting with denser ISM. We compared the average LMC H I column density (from the map of Kim et al. 2003) around the position of remnants in various luminosity bins, but no trend could be found. However, the line-of-sight integrated column density might not be a good indicator of the ISM density *local* to the remnant, considering that the SNR could be in front of or behind the regions where most of the neutral hydrogen is (see Sect. 8).

A possible explanation for the population of bright SNRs in the LMC stems from its lower metallicity. Massive stars lose a considerable amount of mass in the form of winds (e.g. Kudritzki & Puls 2000). The stellar winds blow low-density cavities, bordered by dense shells, around the stars that eventually explode as (core-collapse) SNe. The interaction of the SN shocks with the modified CSM results in a different evolution compared to that in a constant-density ISM. Dwarkadas (2005, 2007, and references therein) explored the evolution of remnants in wind-blown cavities. It was shown that it critically depends on one parameter (coined Λ), the ratio of the mass of the dense shell to that of the ejected material. For low values ($\Lambda < 1$) the X-ray luminosity increases sharply when the shock reaches the dense shell early on ($t < 10^3$ yr). If instead the shell is more massive compared to the ejecta material, the shock propagates in the very low density of the (much larger) bubble, producing less X-ray emission. The increase of X-ray luminosity upon impact (after a few thousand years) is also smaller than in the low-Λ case (Dwarkadas 2005, his Figs. 7 and 12). The properties of the cavities around massive stars are determined by the mass loss rate $\dot{M}$ during their various evolutionary stages. This in turn is affected by the elemental abundance (i.e. metallicity), because the main driving mechanism of stellar winds is the transfer of momentum from photons to the star atmospheric gas by line interactions[20] (Kudritzki & Puls 2000; Vink et al. 2001). By measuring mass-loss rates of early-type stars in the Galaxy, LMC, and SMC, Mokiem et al. (2007) could quantify the dependence of $\dot{M}$ on the metallicity as $\dot{M} \propto Z^{0.83}$. It is therefore expected that in lower metallicity environment (e.g. LMC) massive stars explode in wind-blown cavities with lower Λ, and are more likely to produce *young* remnants that are brighter in X-rays. Since the SMC has the lowest metallicity of our sample of galaxies (0.2 solar), one would also expect an excess of bright sources. However, the SMC does not host SNRs as young (less than a few thousand years) as the LMC (van der Heyden et al. 2004), and it is likely that the smaller wind-blown bubbles do not affect the X-ray luminosities of more evolved remnants. Furthermore, the small number of SNRss in the SMC hinders conclusions regarding a possible excess of bright sources.

Finally, there are also four type Ia SNRs amongst the bright end of the population, to which the explanation discussed above does not apply. If we exclude, these however, there is still an excess. Because they are prominently young (three are less than a thousand years old), it appears that the high current type Ia SN rate in the LMC (Sect. 6.4) will also contribute to a larger population of bright remnants.

Between $\sim 1 \times 10^{35}$ erg s^{-1} and 5×10^{35} erg s^{-1}, where many SNRs reside (a third of the sample), the LMC XLF is comparable in shape to the M31 and M33 XLFs, with a power-law distribution (consistent with α between -1 and -0.8), and in number to M33 (M31 begins to have more sources below $\sim 8 \times 10^{35}$ erg s^{-1}). Towards the fainter end, the LMC XLF is again remarkable via its significant flattening. It is unlikely that this represents an overall flatter distribution (at least not as strongly as in the SMC), because it would imply that a lot of SNRs with $L_X \sim (5-8) \times 10^{35}$ erg s^{-1} (thus easy to identify) have been missed. It is more plausible that the flattening of the XLF is almost exclusively due to incompleteness. The majority of the remnants at $L_X < 8 \times 10^{34}$ erg s^{-1} (15/22) were identified/confirmed thanks to (pointed or serendipitous) *XMM-Newton* observations. Though many were already detected with ROSAT, the combination of the large effective area and resolution of *XMM-Newton* is usually needed to confirm the extent and thermal emission of candidates. Even with the VLP survey, the area of the LMC covered by *XMM-Newton* is less than 20 square degrees, i.e. about a third of the whole galaxy. In particular, X-ray coverage to the south-west of the LMC Bar is sparse (see Fig. 1). Extending the covered fraction warrants to find the missing remnants. The M31 survey with *XMM-Newton* exemplifies how a full coverage results in a high completeness: the M31 SNR XLF is uniform down to the sensitivity limit of the survey, which fully covers the D_{25} ellipse of M31 (Sasaki et al. 2012). In the LMC, the situation could easily be improved with more X-ray observations. We briefly discuss possible strategies in Sect. 9.

8. 3D spatial distribution

8.1. Comparison with other wavelengths

The positions of SNRs in the LMC are plotted on the H I column density map of Kim et al. (2003), showing the LMC gas disc (Fig. 12). The population exhibits correlations with neutral hydrogen structures. The most striking example is the many SNRs (a dozen) around the supergiant shell (SGS) LMC 4 (Meaburn 1980, SGS 11 in the notation of Kim et al. 1999). SGSs are formed by the combined action of multiple generations of massive star formation. Their expansions shock and sweep up the ISM, which can trigger further star formation along the SGS rims (Elmegreen 1998, and references therein). The impact of

[20] The product abundance × ionisation fraction × number of available lines for metals is comparable to that of hydrogen and helium.

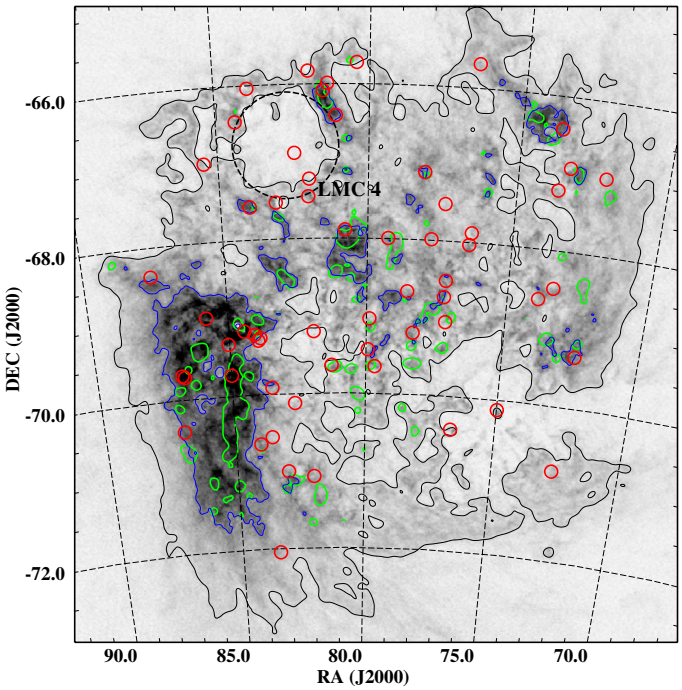

Fig. 12. Positions of LMC SNRs (red circles) on the H I column density map of Kim et al. (2003), displayed on a linear scale ranging from 0 to 6×10^{21} cm^{-2}. Black and blue contours indicate levels of 1 and 3×10^{21} cm^{-2}, respectively. The green contours are the 3σ level (1.2 K km s^{-1}) of the velocity-integrated map of ^{12}CO (J = 1–0) from the NANTEN survey (Fukui et al. 2008). The position of the SGS LMC 4 is marked with a dashed black circle.

SGSs on star formation, particularly in the LMC, was demonstrated by Yamaguchi et al. (2001a,b). They found that the concentration of molecular clouds and young star clusters is enhanced by a factor of 1.5–2 near the SGS rims, and most of these clusters are on the side of the molecular clouds facing the interior of the SGSs. Book et al. (2009) added massive young stellar objects and H II regions/OB associations to the list of tracers of recent star formation that are well correlated with the shell peripheries.

Because (core-collapse) SNRs are themselves very good indicators of recent star formation, the distribution of many SNRs around the edge of LMC 4 is a further sign of the important role played by SGSs in triggering star formation. In turn, this could be used to look for *new* SNRs: the high number of remnants around LMC 4 is explained in part by the large size of the SGS (~1.2 kpc), but also by the good X-ray coverage (only two out of twelve SNRs around LMC 4 were not observed with *XMM-Newton*). Exploring SGSs less well studied, e.g. in the west and south-west regions of the LMC, is promising, as we discuss in Sect. 9.

Another prominent H I feature is the density enhancement in the east that extends southwards into "arms B and E" (see Fig. 1 of Staveley-Smith et al. 2003), which are interpreted as tidal features. Most of the SNRs in the south-east of the LMC are associated to the 30 Doradus complex (which itself might be a manifestation of tidal shear). Only a handful of sources are known in the regions of the B and E arms (and a single SNR is confirmed south of a declination of −71°, Bozzetto et al. 2013). The southern region of the LMC is poorly studied in X-rays, preventing conclusions regarding the dearth of SNRs observed there. However, it could be an interesting target for future studies (Sect. 9).

In Fig. 13, we show the position of SNRs relative to Hα (left, MCELS data), and to a red continuum image from the SHASSA survey (Gaustad et al. 2001). The association of many CC-SNRs with large H II regions, which trace regions of active star formation, is evident: out of 31 secured or "likely" CC SNRs, 25 correlate with strong Hα emission, three with moderate Hα emission, and only three are not associated to large optical nebulosities. In contrast, many SNRs are not associated to Hα emission, e.g. in the Bar, or south-east and north-west of it. These are the type Ia SNRs: 22 out of 24 secured or "likely" Ia SNRs have no coincident Hα emission (except the remnant's emission itself). Only N103B is spatially associated to strong Hα emission, although it is plausibly a projection effect, with the SNR on the far side of the LMC (as suggested by its large "$N_{\rm H}$ fraction", see Sect. 8.2). This would resolve the long-standing issue of the association of a type Ia SNR with a region of intense star formation (Chu & Kennicutt 1988; Badenes et al. 2009). The type Ia SNRs are in regions of relatively high stellar density (e.g. the Bar, as traced in the red continuum image) but are also present in more isolated, less active regions, where intermediate- and old-age stellar populations dominate.

8.2. Adding the third dimension

So far, we discussed the 2D distribution of SNRs, projected on the sky. It is possible to gain a rudimentary sense of depth, by comparing the absorbing column density derived from X-ray observations (hereafter $N_{\rm H}^{\rm X}$), to the line-of-sight integrated H I column density, derived from 21 cm observations (hereafter $N_{\rm H}^{21\,{\rm cm}}$). We recall that $N_{\rm H}^{\rm X}$ is an *equivalent* neutral hydrogen column density assuming a given chemical composition[21]. The ratio $N_{\rm H}^{\rm X}/N_{\rm H}^{21\,{\rm cm}}$ (hereafter "$N_{\rm H}$ fraction") is a measurement of how deep an SNR is with respect to the H I structure. Interpreting the $N_{\rm H}$ fraction is made easier by the favourable orientation of the LMC. Neutral hydrogen is mainly distributed in a nearly circular disc at a moderate inclination angle[22], with a thickness of ~360 pc (Kim et al. 1999). Small $N_{\rm H}$ fractions ($\lesssim$0.3, e.g. when $N_{\rm H}^{\rm X}$ is consistent with zero) indicate that the SNR is well in front of the disc; intermediate values (0.3 to 0.8) are expected from sources within the disc; high fractions (0.8–1.2; a value of 1.23 is expected when including contributions of neutral and singly ionised helium, Arabadjis & Bregman 1999) are associated to remnants on the far side, or behind, the disc. Values significantly above 1.2 are discussed below.

$N_{\rm H}^{\rm X}$ is taken from the spectral results of Sect. 5. For the 1T/2T sample, the adopted value is simply that in Table E.1. Only two 2T remnants have two different absorption components: for MCSNR J0517−6759 we used the higher value. For MCSNR J0535−6602 (N63A), the highly absorbed component is ejecta-rich and has a lower EM; we therefore adopted the (lower) $N_{\rm H}$ of the ISM component, which is more representative. For the brightest SNRs, we adopted the best-fit values given in Table E.2 and in Sect. 5.3 (for SNR 1987A). For three SNRs with

[21] X-rays are absorbed not only by H I, but also by molecular hydrogen, helium, and metals (Wilms et al. 2000).

[22] Measurements of the orientation of the disc, i.e. inclination i (with 0 ° defined as face-on) and position angle of line of nodes Θ (the intersection of the disc and sky planes, measured eastwards of north), are widely scattered but are in the range 25 °$< i <$ 40 ° and 120 °$< \Theta <$ 155 ° (Westerlund 1997; Subramanian & Subramaniam 2013; van der Marel & Kallivayalil 2014).

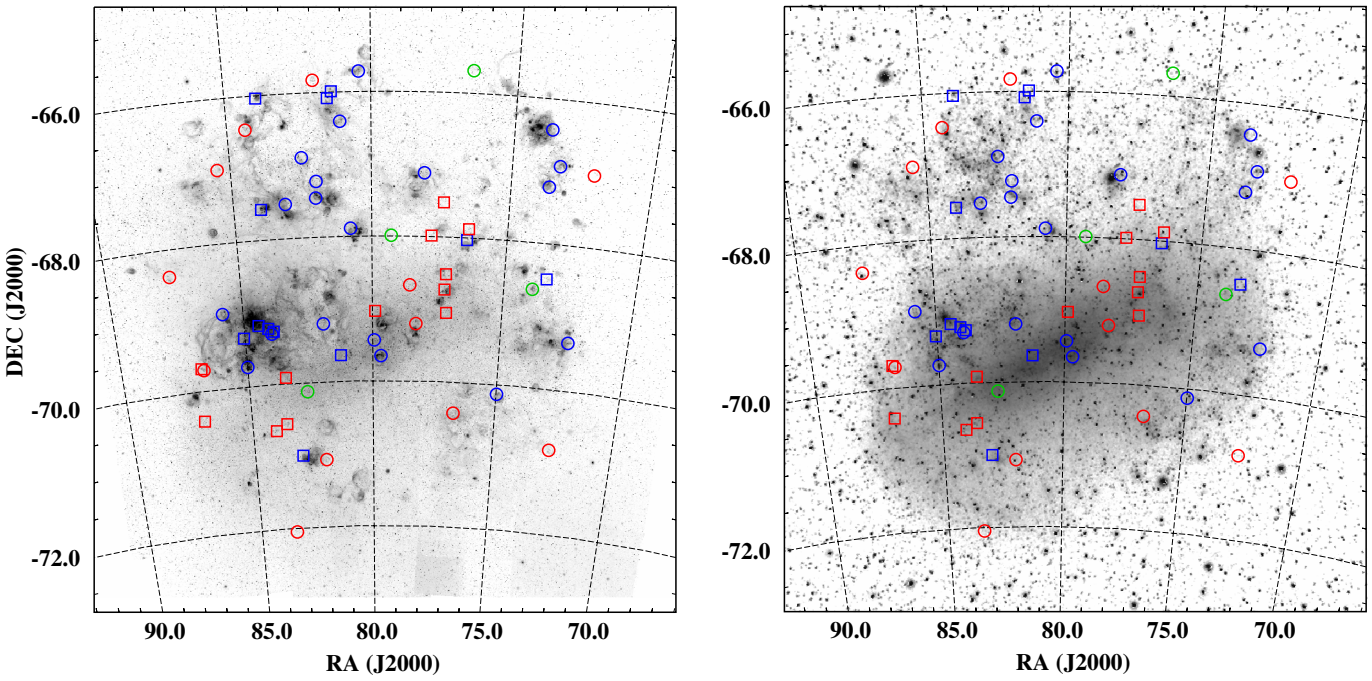

Fig. 13. *Left*: location of LMC SNRs on the MCELS Hα mosaic, displayed logarithmically in greyscale. "Likely-Ia" and "secured-Ia" SNRs are marked by red circles and squares, respectively, while "likely-CC" and "secured-CC" SNRs are shown in blue. Green circles are SNRs with undecided type. *Right*: same as left on a red continuum image from the SHASSA survey.

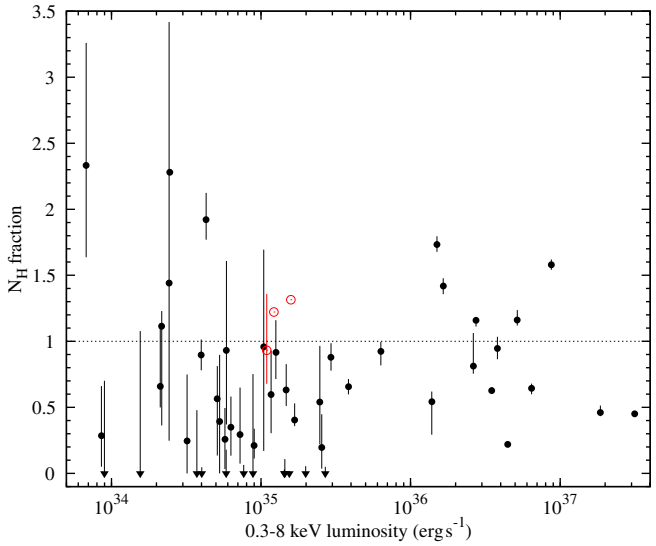

Fig. 14. $N_{\rm H}$ fraction = $N_{\rm H}^{\rm X}/N_{\rm H}^{21\,{\rm cm}}$ as function of broad-band X-ray luminosity (see text for details). Downward pointing arrows indicate upper limits, for objects with $N_{\rm H}^{\rm X}$ consistent with 0. SNRs covered with *Chandra* are shown in red.

Chandra data only, we obtained $N_{\rm H}^{\rm X}$ from the same references as in Sect. 7. Five remaining SNRs have either no or only ROSAT data available, and are not used in this analysis.

$N_{\rm H}^{21\,{\rm cm}}$ is measured from the map of Kim et al. (2003), by averaging the column density around each SNR over a 5′ radius (the resolution of the map is about 1′, i.e. ∼15 pc). We checked that using a smaller averaging radius, closer to the typical SNRs size, gave essentially the same results. We then computed the ratio, propagating only the uncertainties on $N_{\rm H}^{\rm X}$ since they should dominate the error budget in most cases. $N_{\rm H}$ fractions are plotted against $L_{\rm X}$ in Fig. 14. No correlation is evident, as expected: $L_{\rm X}$ depends mostly on the evolutionary state of the remnant, while the depth within the LMC does not. At lower luminosities, however, there are more remnants with only upper limits on $N_{\rm H}^{\rm X}$ (and thus on the $N_{\rm H}$ fraction). This likely stems from the difficulty of deriving $N_{\rm H}^{\rm X}$ from limited X-ray statistics. For the same reason, the error bars are larger in the handful of cases below a few 10^{34} erg s^{-1}, and the sense of depth provided by the $N_{\rm H}$ fraction becomes blurry.

In Fig. 15, the $N_{\rm H}$ fraction is projected on the sky, on the same field of view as showed in Figs. 12 and 13. Prominent LMC structures are labelled, including the LMC Bar: the bar is traced by the stars, both in young and intermediate-age populations (de Vaucouleurs & Freeman 1972; van der Marel 2001, respectively). It was found to be on the near side of the LMC, "floating" ∼0.5 kpc to 5 kpc above the plane of the disc, as evidenced from near-infrared star count maps and distances to Cepheids, red clump, and RR Lyrae stars (Zhao & Evans 2000; Nikolaev et al. 2004; Koerwer 2009; Haschke et al. 2012). This interpretation is challenged by red clump stars distance measurements of Subramaniam & Subramanian (2009) and Subramanian & Subramaniam (2013). Zaritsky (2004) proposed an alternative model, where the Bar is a stellar bulge (with a z scale height of 2.5–3 kpc) whose south-eastern part is obscured by the gas disc. Consequently, the photometric centre is offset (in the plane of the sky), and distance measurements are biased to stars in the near side of the bulge. As can be seen in Fig. 15, SNRs in the Bar region are primarily on the near side (low $N_{\rm H}$ fraction). Since some of these remnants must originate from the stellar population of the Bar, this lends support to previous findings that the Bar is indeed "floating" in front of the disc. One advantage of our method is that it does not need distance measurements of both disc and Bar objects; it directly gives locations *relative* to the disc. In the bulge model of Zaritsky (2004), SNRs in the Bar, but behind the

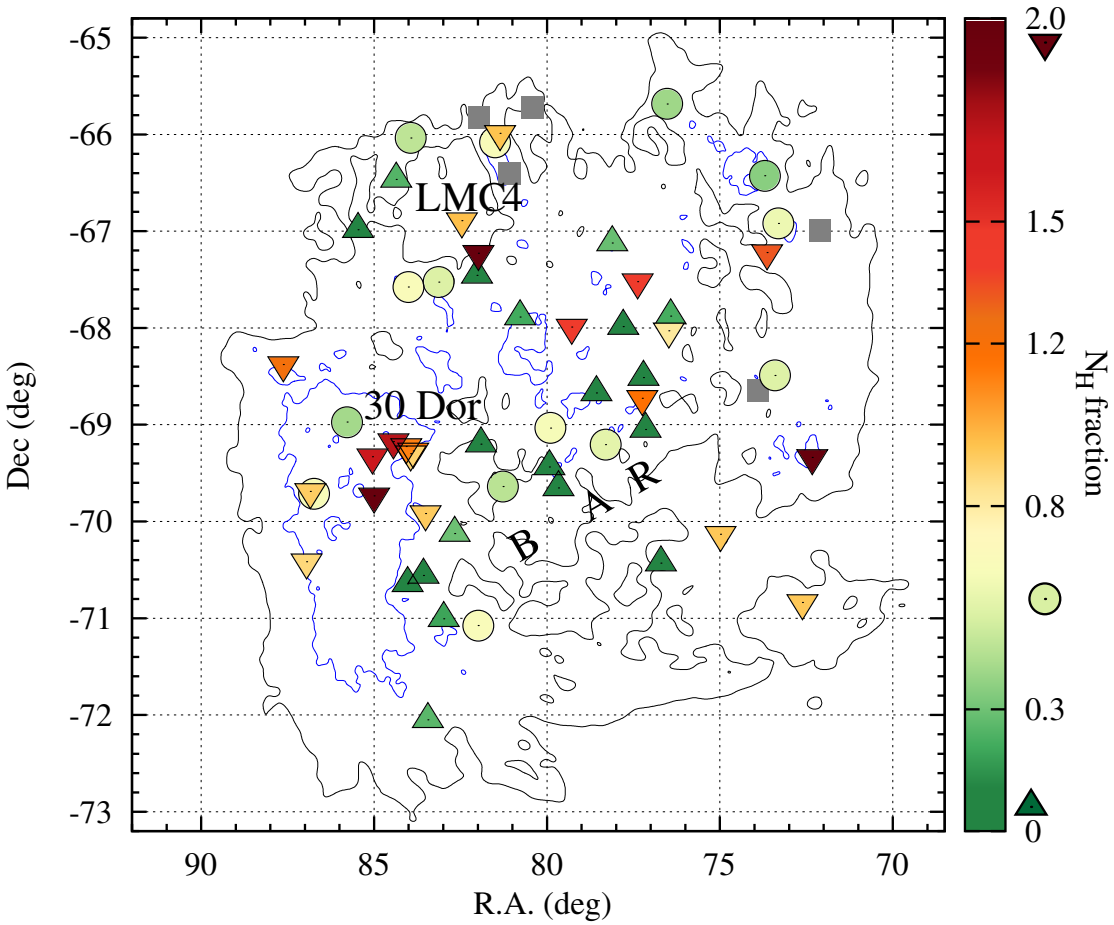

Fig. 15. "Pseudo-3D" distribution of LMC SNRs, using $N_{\rm H}$ fractions (quantified by the colour bar) as indicators of location along the line of sight. Objects "in front of the disc" ($N_{\rm H}$ fraction <0.3) are marked by upward pointing triangles; downward pointing triangles are used for those "behind the disc ($N_{\rm H}$ fraction >0.8). Objects within the disc (0.3 to 0.8) are marked by dots. The black and blue contours delineate H I column densities of 1 and 3×10^{21} cm^{-2}, respectively (same as in Fig. 12). Prominent LMC structures are labelled.

disc[23], should have large $N_{\rm H}$ fractions, while some scatter should be found along the line of nodes, where the disc and bulge intersect. Unfortunately, there are too few SNRs known in the Bar region to adequately test this alternative model.

The remnants in the 30 Doradus region and directly south of it (MCSNR J0540−6920 and J0540−6944) are the most absorbed, both in absolute and relative terms (largest $N_{\rm H}^{\rm X}$ and largest $N_{\rm H}$ fractions). From distance measurements with red clump stars, Koerwer (2009) found that 30 Dor was further away, although it was noted that this could be an effect of 30 Dor being next to the Bar floating in front of the disc. With our analysis it is confirmed that not only does 30 Dor lie at a larger distance compared to neighbouring features, but is indeed *behind* the plane of the gas disc.

Finally, it is striking from Figs. 14 and 15 that a few SNRs have an $N_{\rm H}$ fraction in excess of 1.2, and up to 2.3. The extra absorption is likely to come from molecular hydrogen in front of the object (Arabadjis & Bregman 1999). We show in Fig. 12 CO contours from the NANTEN survey (Fukui et al. 2008). CO is used as a tracer of molecular hydrogen. In the east of the LMC there are large regions of molecular gas, following the peak density in H I. In most cases with large $N_{\rm H}$ fractions, we find nearby (less than a few arcmin away in projection) CO clouds, using either the NANTEN catalogue or the higher resolution MAGMA survey (Fukui et al. 2008; Wong et al. 2011, respectively). We stress that this does not imply that the remnants and the molecular clouds are physically connected, but can be merely a projection effect, with the remnant behind, and not interacting with, the molecular cloud. However, physical interactions can happen, as exemplified by the case of MCSNR J0517−6759, where secondary evidence hints at a physical connection (Maggi et al. 2014).

[23] The obscuring effect by the disc on X-rays is moderate, not sufficient to mask SNRs as it does on stars in optical surveys.

9. Summary and outlooks

We have studied the X-ray emission of the rich population of SNRs in the LMC, using data from the *XMM-Newton* observatory. We compiled a sample of 59 definite SNRs, cleaned of misclassified objects and doubtful candidates. *XMM-Newton* data are available for the vast majority (51 SNRs) of the sample, which called for a homogeneous re-analysis of the X-ray spectra of the entire population. This alleviates the inconsistencies in spectral models and analysis methods used, and allows meaningful comparisons of, e.g., temperature, chemical composition, and luminosity of SNRs. The main outcomes of this systematic spectral analysis are the following:

– First, it provides the best census of LMC remnants with an Fe K line (≈13% of the sample), which is a powerful tool to retrieve the type of SN progenitor.

- Second, it reveals the contribution to the X-ray emission by hot SN ejecta for 23 SNRs (≈39% of the sample). Since the abundance ratios measured in the ejecta components reflect the nucleosynthesis yields of either type Ia and CC SNe, this is of great help for the typing of a substantial fraction of the sample.
- And third, it allows us to select 16 SNRs (≈27% of the sample) where the X-ray emission is dominated by swept-up ISM. In these objects, the fitted abundances provide a measurement of chemical abundances in the gas phase of the LMC ISM. A metallicity of [Fe/H] = $-0.46(^{+0.13}_{-0.18})$ dex is found based on *XMM-Newton* SNRs. Light α-elements (O, Ne, Mg) have lower abundance ratios [α/Fe] than in the Milky Way. Although this general result was previously known, one can now study abundance ratios within the LMC as function of age. In comparison to old clusters (∼10 Gyr) and red giant stars (1 Gyr and older), the relatively young gas phase ISM ($\lesssim$100 Myr) has a higher metallicity [Fe/H] and lower [α/Fe] (in particular [O/Fe]). This reflects the continued enrichment by type Ia SNe in the last ∼1 Gyr, which injected large amounts of Fe back in the ISM.

We devised a quantitative way to tentatively type all LMC SNRs, based on their local SFHs and stellar environments, combined with spectral information (i.e. detection of SN ejecta, when present). We calibrated this method with SNRs having a well-established type based on robust indicators. The resulting ratio of CC to type Ia SNe that exploded in the LMC over the last few 10^4 yr (i.e. very close to the current ratio of CC/Ia *rates*) is $N_{\rm CC}/N_{\rm Ia} = 1.35(^{+0.11}_{-0.24})$. This is lower than the ratio typically measured in local SNe surveys and in galaxy clusters. After arguing that SNRs of both types might be absent from the sample (i.e. the current sample is not biased towards one type only), we concluded that the low $N_{\rm CC}/N_{\rm Ia}$ ratio is a consequence of the specific SFH of the LMC, and particularly the enhanced star formation episodes that occurred 500 Myr and 2 Gyr ago. Because the majority of type Ia SNe explode within 2 Gyr after star-forming episodes, we are coincidentally observing the LMC at a time when the type Ia SN rate is high. Integrated over an SNR lifetime, this results in the relatively low $N_{\rm CC}/N_{\rm Ia}$ observed.

We also assessed the spatial distribution of SNRs with respect to cool gas (traced by H I and molecular emission), star-forming regions (Hα), and stars (red continuum). A concentration of SNRs around the edge of the SGS LMC 4 exemplifies the role of SGSs in triggering star formation. The column density $N_{\rm H}^{\rm X}$ obtained during the X-ray spectral analysis of the whole sample, when compared to the H I column density, provides a measurement of the position of each SNR relative to the H I structure. Since most of the neutral gas lies in a well-defined thin disc seen at a moderate inclination angle, the fraction $N_{\rm H}^{\rm X}/N_{\rm H}^{21\,\rm cm}$ is a good indicator of the depth along the line-of-sight, revealing the "pseudo-3D" distribution of SNRs in the LMC. Previous studies found that the Bar is "floating" in front of the disc, but this statement was challenged by some authors. Our analysis shows that SNRs in the Bar regions are primarily on the near side (low $N_{\rm H}$ fraction), lending support to the foreground location of the Bar.

Finally, we compared the populations of SNRs in Local Group galaxies via their X-ray luminosity function. The XLF of SNRs in the SMC, M31, and M33 are relatively homogeneous over all the observed luminosity range, although that of the SMC is flatter. The LMC XLF is remarkable by its prominent bright end. The largest population of SNRs brighter than $L_{\rm X} > 10^{36}$ erg s^{-1} is found in the LMC (13 SNRs vs. 8 and 7 in M31 and M33, respectively). This is possibly an effect of the lower metallicity in the LMC: massive stars have smaller mass loss rates (less heavy elements to drive stellar winds) and the interaction of SN ejecta with less massive CSM shells produce brighter remnants. The number of SNRs brighter than 10^{35} erg s^{-1} in the LMC is comparable to that in M31 and M33, likely owing to its high recent SFR and high current type Ia SN rate. The LMC XLF flattens significantly because of incompleteness: many X-ray-faint SNRs have been missed so far, due to the incomplete coverage of the LMC with sensitive X-ray instruments (i.e. *Chandra* or *XMM-Newton*).

This work presents the state of the art on X-ray emission of SNRs in the LMC. However, it is clear that the *current* sample is incomplete, as evidenced by the flattening of the X-ray luminosity function of LMC SNRs (Sect. 7). In the last 15 years, new SNRs were confirmed or discovered in the LMC at an almost constant rate (one or few per year), principally using X-ray observations. There is no indication that this trend will stop in the near future, so that more observations of the LMC will increase the sample of SNRs.

Nevertheless, the observing time of major observatories is limited and expensive. We conclude this work by offering several strategies to maximise the chance of finding "missing" SNRs:

- As shown in Sect. 8, star formation is intense around the SGS LMC 4, and the edges of the shell abound in SNRs. Many LMC SGS have not been (fully) surveyed by *XMM-Newton*, for instance (in the notation of Kim et al. 1999) SGS 3 and 6 in the north, SGS 2 and 5 in the west, and SGS 4 in the south. Targeting in particular SGSs associated to star formation (e.g. with H II region along the rims) warrants successful SNR searches.
- The follow-up observations of X-ray-selected candidates (usually ROSAT sources) with *XMM-Newton* have been extremely successful. Such programmes should be continued until completion of the list of candidates.
- Even the ROSAT (targeted) survey of the LMC was not covering the LMC up to its outskirts. To find SNRs in these regions, the future *eROSITA* survey (Merloni et al. 2012) will be most useful, covering the full sky in the 0.5−8 keV band. The LMC is located close to the South Ecliptic Pole and will be observed with a deeper exposure than the rest of the sky. Looking for new SNR candidates, especially evolved X-ray-only SNRs, will be of special interest.

Even in *existing* data, some SNRs might be as yet unrecognised. There is significant diffuse emission from large-scale structures of the hot ISM in the LMC (Sasaki et al. 2002), which is seen in greater spatial and spectral detail by *XMM-Newton*. By looking for ejecta-enhancement, it might be possible to distinguish old SNRs with low surface brightness hiding in the diffuse emission.

Finding new SNRs is desirable. Individual objects of special interest are often found serendipitously, without prior knowledge of their exciting nature. The evolved type Ia SNRs presented in Maggi et al. (2014) and Bozzetto et al. (2014), are good examples; the discovery of the SNR around the Be/X-ray binary SXP 1062 is another one (Hénault-Brunet et al. 2012; Haberl et al. 2012c). Furthermore, as demonstrated in this work, SNRs are powerful probes of the ISM of their host galaxies. With more SNRs where metallicity can be measured, we will obtain a more accurate knowledge of the chemical composition of the hot ISM or better assess its homogeneity.

Acknowledgements. We thank the anonymous referee for carefully reading this rather long manuscript and providing us with comments and suggestions to

improve it. The *XMM-Newton* project is supported by the Bundesministerium für Wirtschaft und Technologie / Deutsches Zentrum für Luft- und Raumfahrt (BMWi/DLR, FKZ 50 OX 0001) and the Max-Planck Society. P.M. acknowledges support by the Centre National d'Études Spatiales (CNES) and from the BMWi/DLR grant FKZ 50 OR 1201. M.S. acknowledges support by the Deutsche Forschungsgemeinschaft through the Emmy Noether Research Grant SA 2131/1-1. P.K. acknowledges support from the BMWi/DLR grant FKZ 50 OR 1309. This research has made use of Aladin, SIMBAD and VizieR, operated at the CDS, Strasbourg, France.

References

Abbey, T., Carpenter, J., Read, A., et al. 2006, in The X-ray Universe 2005, ed. A. Wilson, ESA Spec. Publ., 604, 943
Arabadjis, J. S., & Bregman, J. N. 1999, ApJ, 510, 806
Arnaud, K. A. 1996, in Astronomical Data Analysis Software and Systems V, eds. G. H. Jacoby & J. Barnes, ASP Conf. Ser., 101, 17
Badenes, C., Bravo, E., Borkowski, K. J., & Domínguez, I. 2003, ApJ, 593, 358
Badenes, C., Borkowski, K. J., & Bravo, E. 2005, ApJ, 624, 198
Badenes, C., Hughes, J. P., Cassam-Chenaï, G., & Bravo, E. 2008, ApJ, 680, 1149
Badenes, C., Harris, J., Zaritsky, D., & Prieto, J. L. 2009, ApJ, 700, 727
Badenes, C., Maoz, D., & Draine, B. T. 2010, MNRAS, 407, 1301
Balucinska-Church, M., & McCammon, D. 1992, ApJ, 400, 699
Bamba, A., Ueno, M., Nakajima, H., & Koyama, K. 2004, ApJ, 602, 257
Bamba, A., Yamazaki, R., Yoshida, T., Terasawa, T., & Koyama, K. 2005, ApJ, 621, 793
Bamba, A., Ueno, M., Nakajima, H., Mori, K., & Koyama, K. 2006, A&A, 450, 585
Barret, D., den Herder, J. W., Piro, L., et al. 2013, ArXiv e-prints [arXiv:1308.6784]
Behar, E., Rasmussen, A. P., Griffiths, R. G., et al. 2001, A&A, 365, L242
Blackburn, J. K. 1995, in Astronomical Data Analysis Software and Systems IV, eds. R. A. Shaw, H. E. Payne, & J. J. E. Hayes, ASP Conf. Ser., 77, 367
Blair, W. P., Ghavamian, P., Sankrit, R., & Danforth, C. W. 2006, ApJS, 165, 480
Bojičić, I. S., Filipović, M. D., Parker, Q. A., et al. 2007, MNRAS, 378, 1237
Book, L. G., Chu, Y.-H., Gruendl, R. A., & Fukui, Y. 2009, AJ, 137, 3599
Borkowski, K. J., Hendrick, S. P., & Reynolds, S. P. 2006, ApJ, 652, 1259
Borkowski, K. J., Hendrick, S. P., & Reynolds, S. P. 2007, ApJ, 671, L45
Bozzetto, L. M., Filipović, M. D., Crawford, E. J., et al. 2012a, MNRAS, 420, 2588
Bozzetto, L. M., Filipovic, M. D., Crawford, E. J., et al. 2012b, Rev. Mex. Astron. Astrofis., 48, 41
Bozzetto, L. M., Filipović, M. D., Crawford, E. J., et al. 2013, MNRAS, 432, 2177
Bozzetto, L. M., Kavanagh, P. J., Maggi, P., et al. 2014, MNRAS, 439, 1110
Cajko, K. O., Crawford, E. J., & Filipovic, M. D. 2009, Serbian Astronomical J., 179, 55
Cash, W. 1979, ApJ, 228, 939
Chen, L.-W., Fabian, A. C., & Gendreau, K. C. 1997, MNRAS, 285, 449
Chen, Y., Wang, Q. D., Gotthelf, E. V., et al. 2006, ApJ, 651, 237
Chevalier, R. A., & Kirshner, R. P. 1979, ApJ, 233, 154
Chevalier, R. A., & Raymond, J. C. 1978, ApJ, 225, L27
Chevalier, R. A., Kirshner, R. P., & Raymond, J. C. 1980, ApJ, 235, 186
Chu, Y.-H. 2008, in IAU Symp. 250, eds. F. Bresolin, P. A. Crowther, & J. Puls, 341
Chu, Y.-H., & Kennicutt, Jr., R. C. 1988, AJ, 96, 1874
Chu, Y.-H., Mac Low, M.-M., Garcia-Segura, G., Wakker, B., & Kennicutt, Jr., R. C. 1993, ApJ, 414, 213
Chu, Y.-H., Dickel, J. R., Staveley-Smith, L., Osterberg, J., & Smith, R. C. 1995, AJ, 109, 1729
Chu, Y.-H., Kennicutt, R. C., Snowden, S. L., et al. 1997, PASP, 109, 554
Chu, Y.-H., Kim, S., Points, S. D., Petre, R., & Snowden, S. L. 2000, AJ, 119, 2242
Cole, A. A., Tolstoy, E., Gallagher, III, J. S., & Smecker-Hane, T. A. 2005, AJ, 129, 1465
Corbelli, E. 2003, MNRAS, 342, 199
Crawford, E. J., Filipović, M. D., McEntaffer, R. L., et al. 2014, AJ, 148, 99
Da Costa, G. S. 1991, in The Magellanic Clouds, eds. R. Haynes, & D. Milne, IAU Symp., 148, 183
de Grijs, R., Wicker, J. E., & Bono, G. 2014, AJ, 147, 122
de Horta, A. Y., Filipović, M. D., Bozzetto, L. M., et al. 2012, A&A, 540, A25
de Plaa, J., Werner, N., Bleeker, J. A. M., et al. 2007, A&A, 465, 345
de Vaucouleurs, G., & Freeman, K. C. 1972, Vistas Astron., 14, 163
den Herder, J. W., Brinkman, A. C., Kahn, S. M., et al. 2001, A&A, 365, L7
Dennerl, K., Haberl, F., Aschenbach, B., et al. 2001, A&A, 365, L202
Desai, K. M., Chu, Y.-H., Gruendl, R. A., et al. 2010, AJ, 140, 584
Dickey, J. M., & Lockman, F. J. 1990, ARA&A, 28, 215
Dopita, M. A., Blair, W. P., Long, K. S., et al. 2010, ApJ, 710, 964
Dunne, B. C., Points, S. D., & Chu, Y.-H. 2001, ApJS, 136, 119
Dwarkadas, V. V. 2005, ApJ, 630, 892
Dwarkadas, V. V. 2007, ApJ, 667, 226
Eisenhardt, P. R. M., Brodwin, M., Gonzalez, A. H., et al. 2008, ApJ, 684, 905
Elmegreen, B. G. 1998, in Origins, ASP Conf. Ser. 148, 150, eds. C. E. Woodward, J. M. Shull, & H. A. Thronson, Jr.
Ferrand, G., & Safi-Harb, S. 2012, Adva. Space Res., 49, 1313
Filipovic, M. D., Haynes, R. F., White, G. L., & Jones, P. A. 1998, A&AS, 130, 421
Filipović, M. D., Haberl, F., Winkler, P. F., et al. 2008, A&A, 485, 63
Flanagan, K. A., Canizares, C. R., Dewey, D., et al. 2004, ApJ, 605, 230
Freyberg, M. J., Briel, U. G., Dennerl, K., et al. 2004, in SPIE Conf. Ser. 5165, eds. K. A. Flanagan, & O. H. W. Siegmund, 112
Fukui, Y., Kawamura, A., Minamidani, T., et al. 2008, ApJS, 178, 56
Gaensler, B. M., Slane, P. O., Gotthelf, E. V., & Vasisht, G. 2001, ApJ, 559, 963
Gaensler, B. M., Hendrick, S. P., Reynolds, S. P., & Borkowski, K. J. 2003, ApJ, 594, L111
Gaustad, J. E., McCullough, P. R., Rosing, W., & Van Buren, D. 2001, PASP, 113, 1326
Ghavamian, P., Rakowski, C. E., Hughes, J. P., & Williams, T. B. 2003, ApJ, 590, 833
Green, D. A. 2014, Bull. Astron. Soc. India, 42, 47
Grondin, M.-H., Sasaki, M., Haberl, F., et al. 2012, A&A, 539, A15
Haberl, F., & Pietsch, W. 1999, A&AS, 139, 277
Haberl, F., Geppert, U., Aschenbach, B., & Hasinger, G. 2006, A&A, 460, 811
Haberl, F., Filipović, M. D., Bozzetto, L. M., et al. 2012a, A&A, 543, A154
Haberl, F., Sturm, R., Ballet, J., et al. 2012b, A&A, 545, A128
Haberl, F., Sturm, R., Filipović, M. D., Pietsch, W., & Crawford, E. J. 2012c, A&A, 537, L1
Harris, J., & Zaritsky, D. 2004, AJ, 127, 1531
Harris, J., & Zaritsky, D. 2006, AJ, 131, 2514
Harris, J., & Zaritsky, D. 2008, PASA, 25, 116
Harris, J., & Zaritsky, D. 2009, AJ, 138, 1243
Haschke, R., Grebel, E. K., & Duffau, S. 2012, AJ, 144, 106
Helder, E. A., Broos, P. S., Dewey, D., et al. 2013, ApJ, 764, 11
Hénault-Brunet, V., Oskinova, L. M., Guerrero, M. A., et al. 2012, MNRAS, 420, L13
Hendrick, S. P., Borkowski, K. J., & Reynolds, S. P. 2003, ApJ, 593, 370
Heng, K., Haberl, F., Aschenbach, B., & Hasinger, G. 2008, ApJ, 676, 361
Henley, D. B., & Shelton, R. L. 2008, ApJ, 676, 335
Hodge, P. W. 1960, ApJ, 131, 351
Hodge, P. W. 1961, ApJ, 133, 413
Holtzman, J. A., Gallagher, III, J. S., Cole, A. A., et al. 1999, AJ, 118, 2262
Hughes, J. P., Hayashi, I., Helfand, D., et al. 1995, ApJ, 444, L81
Hughes, J. P., Hayashi, I., & Koyama, K. 1998, ApJ, 505, 732
Hughes, J. P., Ghavamian, P., Rakowski, C. E., & Slane, P. O. 2003, ApJ, 582, L95
Hughes, J. P., Rafelski, M., Warren, J. S., et al. 2006, ApJ, 645, L117
Jansen, F., Lumb, D., Altieri, B., et al. 2001, A&A, 365, L1
Jaskot, A. E., Strickland, D. K., Oey, M. S., Chu, Y.-H., & García-Segura, G. 2011, ApJ, 729, 28
Jennings, Z. G., Williams, B. F., Murphy, J. W., et al. 2012, ApJ, 761, 26
Jennings, Z. G., Williams, B. F., Murphy, J. W., et al. 2014, ApJ, 795, 170
Johnson, J. A., Ivans, I. I., & Stetson, P. B. 2006, ApJ, 640, 801
Kaaret, P., Marshall, H. L., Aldcroft, T. L., et al. 2001, ApJ, 546, 1159
Kaplan, D. L., Kulkarni, S. R., van Kerkwijk, M. H., et al. 2001, ApJ, 556, 399
Kavanagh, P. J., Sasaki, M., Points, S. D., et al. 2013, A&A, 549, A99
Kavanagh, P. J., Sasaki, M., Bozzetto, L. M., et al. 2015a, A&A, 573, A73
Kavanagh, P. J., Sasaki, M., Whelan, E. T., et al. 2015b, A&A, 583, A121
Kavanagh, P. J., Sasaki, M., Bozzetto, L. M., et al. 2015c, A&A, 579, A63
Kim, S., Dopita, M. A., Staveley-Smith, L., & Bessell, M. S. 1999, AJ, 118, 2797
Kim, S., Staveley-Smith, L., Dopita, M. A., et al. 2003, ApJS, 148, 473
Klimek, M. D., Points, S. D., Smith, R. C., Shelton, R. L., & Williams, R. 2010, ApJ, 725, 2281
Koerwer, J. F. 2009, AJ, 138, 1
Kosenko, D., Vink, J., Blinnikov, S., & Rasmussen, A. 2008, A&A, 490, 223
Kosenko, D., Helder, E. A., & Vink, J. 2010, A&A, 519, A11
Koyama, K., Petre, R., Gotthelf, E. V., et al. 1995, Nature, 378, 255
Kozłowski, S., Kochanek, C. S., Jacyszyn, A. M., et al. 2012, ApJ, 746, 27
Kudritzki, R.-P., & Puls, J. 2000, ARA&A, 38, 613
Kuntz, K. D., & Snowden, S. L. 2008, A&A, 478, 575
Kuntz, K. D., & Snowden, S. L. 2010, ApJS, 188, 46
Lapenna, E., Mucciarelli, A., Origlia, L., & Ferraro, F. R. 2012, ApJ, 761, 33
Lasker, B. M. 1978, ApJ, 223, 109
Lejeune, T., & Schaerer, D. 2001, A&A, 366, 538
Lewis, K. T., Burrows, D. N., Hughes, J. P., et al. 2003, ApJ, 582, 770

Li, W., Leaman, J., Chornock, R., et al. 2011, MNRAS, 412, 1441
Long, K. S., Helfand, D. J., & Grabelsky, D. A. 1981, ApJ, 248, 925
Long, K. S., Blair, W. P., Winkler, P. F., et al. 2010, ApJS, 187, 495
Lopez, L. A., Ramirez-Ruiz, E., Badenes, C., et al. 2009, ApJ, 706, L106
Lopez, L. A., Ramirez-Ruiz, E., Huppenkothen, D., Badenes, C., & Pooley, D. A. 2011, ApJ, 732, 114
Lovisari, L., Schindler, S., & Kapferer, W. 2011, A&A, 528, A60
Lowry, J. D., Chu, Y.-H., Guerrero, M. A., et al. 2004, AJ, 127, 125
Lumb, D. H., Warwick, R. S., Page, M., & De Luca, A. 2002, A&A, 389, 93
Lumb, D. H., Schartel, N., & Jansen, F. A. 2012, Opt. Eng., 51, 011009
Mac Low, M.-M., & Klessen, R. S. 2004, Reviews of Modern Physics, 76, 125
Maggi, P., Haberl, F., Bozzetto, L. M., et al. 2012a, A&A, 546, A109
Maggi, P., Haberl, F., Sturm, R., & Dewey, D. 2012b, A&A, 548, L3
Maggi, P., Haberl, F., Kavanagh, P. J., et al. 2014, A&A, 561, A76
Maoz, D. 2008, MNRAS, 384, 267
Maoz, D., & Badenes, C. 2010, MNRAS, 407, 1314
Maoz, D., & Mannucci, F. 2012, PASA, 29, 447
Mason, K. O., Breeveld, A., Much, R., et al. 2001, A&A, 365, L36
Mathewson, D. S., & Clarke, J. N. 1973, ApJ, 180, 725
Mathewson, D. S., Healey, J. R., & Westerlund, B. E. 1963, Nature, 199, 681
Mathewson, D. S., Ford, V. L., Dopita, M. A., et al. 1983, ApJS, 51, 345
Mathewson, D. S., Ford, V. L., Dopita, M. A., et al. 1984, ApJS, 55, 189
Mathewson, D. S., Ford, V. L., Tuohy, I. R., et al. 1985, ApJS, 58, 197
Meaburn, J. 1980, MNRAS, 192, 365
Merloni, A., Predehl, P., Becker, W., et al. 2012, ArXiv e-prints [arXiv:1209.3114]
Mills, B. Y., Turtle, A. J., Little, A. G., & Durdin, J. M. 1984, Austr. J. Phys., 37, 321
Misanovic, Z., Pietsch, W., Haberl, F., et al. 2006, A&A, 448, 1247
Mokiem, M. R., de Koter, A., Vink, J. S., et al. 2007, A&A, 473, 603
Morse, J. A., Winkler, P. F., & Kirshner, R. P. 1995, AJ, 109, 2104
Nikolaev, S., Drake, A. J., Keller, S. C., et al. 2004, ApJ, 601, 260
Nishiuchi, M., Yokogawa, J., Koyama, K., & Hughes, J. P. 2001, PASJ, 53, 99
Owen, R. A., Filipović, M. D., Ballet, J., et al. 2011, A&A, 530, A132
Park, S., Burrows, D. N., Garmire, G. P., et al. 2003a, ApJ, 586, 210
Park, S., Hughes, J. P., Slane, P. O., et al. 2003b, apjl, 592, L41
Park, S., Hughes, J. P., Slane, P. O., et al. 2012, ApJ, 748, 117
Payne, J. L., White, G. L., & Filipović, M. D. 2008, MNRAS, 383, 1175
Peñarrubia, J., Ma, Y.-Z., Walker, M. G., & McConnachie, A. 2014, MNRAS, 443, 2204
Perlmutter, S., Aldering, G., Goldhaber, G., et al. 1999, ApJ, 517, 565
Peters, C. L., Lopez, L. A., Ramirez-Ruiz, E., Stassun, K. G., & Figueroa-Feliciano, E. 2013, ApJ, 771, L38
Pietrzyński, G., Graczyk, D., Gieren, W., et al. 2013, Nature, 495, 76
Pietsch, W., Misanovic, Z., Haberl, F., et al. 2004, A&A, 426, 11
Pietsch, W., Freyberg, M., & Haberl, F. 2005, A&A, 434, 483
Plucinsky, P. P., Williams, B., Long, K. S., et al. 2008, ApJS, 174, 366
Pompéia, L., Hill, V., Spite, M., et al. 2008, A&A, 480, 379
Rest, A., Suntzeff, N. B., Olsen, K., et al. 2005, Nature, 438, 1132
Rest, A., Matheson, T., Blondin, S., et al. 2008, ApJ, 680, 1137
Reyes-Iturbide, J., Rosado, M., & Velázquez, P. F. 2008, AJ, 136, 2011
Reyes-Iturbide, J., Rosado, M., Rodríguez-González, A., et al. 2014, AJ, 148, 102
Rho, J., Dyer, K. K., Borkowski, K. J., & Reynolds, S. P. 2002, ApJ, 581, 1116
Riess, A. G., Filippenko, A. V., Challis, P., et al. 1998, AJ, 116, 1009
Russell, S. C., & Dopita, M. A. 1992, ApJ, 384, 508
Sasaki, M., Haberl, F., & Pietsch, W. 2002, A&A, 392, 103
Sasaki, M., Pietsch, W., Haberl, F., et al. 2012, A&A, 544, A144
Sato, K., Tokoi, K., Matsushita, K., et al. 2007, ApJ, 667, L41
Seok, J. Y., Koo, B.-C., Onaka, T., et al. 2008, PASJ, 60, 453
Seok, J. Y., Koo, B.-C., & Onaka, T. 2013, ApJ, 779, 134
Seward, F. D., Williams, R. M., Chu, Y.-H., et al. 2006, ApJ, 640, 327
Seward, F. D., Charles, P. A., Foster, D. L., et al. 2012, ApJ, 759, 123
Sim, S. A., Röpke, F. K., Hillebrandt, W., et al. 2010, ApJ, 714, L52
Slane, P. 2014, in IAU Symp. 296, eds. A. Ray, & R. A. McCray, 226
Smecker-Hane, T. A., Cole, A. A., Gallagher, III, J. S., & Stetson, P. B. 2002, ApJ, 566, 239
Smith, R. C., Chu, Y.-H., Mac Low, M.-M., Oey, M. S., & Klein, U. 1994, AJ, 108, 1266
Smith, C., Leiton, R., & Pizarro, S. 2000, in Stars, Gas and Dust in Galaxies: Exploring the Links, eds. D. Alloin, K. Olsen, & G. Galaz, ASP Conf. Ser., 221, 83
Snowden, S. L., Mushotzky, R. F., Kuntz, K. D., & Davis, D. S. 2008, A&A, 478, 615
Stanimirović, S., Staveley-Smith, L., & Jones, P. A. 2004, ApJ, 604, 176
Staveley-Smith, L., Kim, S., Calabretta, M. R., Haynes, R. F., & Kesteven, M. J. 2003, MNRAS, 339, 87
Stiele, H., Pietsch, W., Haberl, F., et al. 2011, A&A, 534, A55
Strüder, L., Briel, U., Dennerl, K., et al. 2001, A&A, 365, L18
Sturm, R. K. N. 2012, PhD thesis, Fakultät für Physik, Technische Universität München, Germany
Sturm, R., Haberl, F., Aschenbach, B., & Hasinger, G. 2010, A&A, 515, A5
Sturm, R., Haberl, F., Pietsch, W., et al. 2013, A&A, 558, A3
Subramaniam, A., & Subramanian, S. 2009, ApJ, 703, L37
Subramanian, S., & Subramaniam, A. 2013, A&A, 552, A144
Tabatabaei, F. S., & Berkhuijsen, E. M. 2010, A&A, 517, A77
Takahashi, T., Mitsuda, K., Kelley, R., et al. 2012, in SPIE Conf. Ser., 8443
Tsujimoto, T., Nomoto, K., Yoshii, Y., et al. 1995, MNRAS, 277, 945
Tüllmann, R., Gaetz, T. J., Plucinsky, P. P., et al. 2011, ApJS, 193, 31
Tuohy, I. R., Dopita, M. A., Mathewson, D. S., Long, K. S., & Helfand, D. J. 1982, ApJ, 261, 473
Turner, M. J. L., Abbey, A., Arnaud, M., et al. 2001, A&A, 365, L27
Turtle, A. J., & Mills, B. Y. 1984, PASA, 5, 537
van der Heyden, K. J., Behar, E., Vink, J., et al. 2002, A&A, 392, 955
van der Heyden, K. J., Bleeker, J. A. M., Kaastra, J. S., & Vink, J. 2003, A&A, 406, 141
van der Heyden, K. J., Bleeker, J. A. M., & Kaastra, J. S. 2004, A&A, 421, 1031
van der Marel, R. P. 2001, AJ, 122, 1827
van der Marel, R. P., & Kallivayalil, N. 2014, ApJ, 781, 121
van der Marel, R. P., Alves, D. R., Hardy, E., & Suntzeff, N. B. 2002, AJ, 124, 2639
Van der Swaelmen, M., Hill, V., Primas, F., & Cole, A. A. 2013, A&A, 560, A44
van Kerkwijk, M. H., Chang, P., & Justham, S. 2010, ApJ, 722, L157
Verley, S., Corbelli, E., Giovanardi, C., & Hunt, L. K. 2009, A&A, 493, 453
Vink, J. 2012, A&ARv, 20, 49
Vink, J. S., de Koter, A., & Lamers, H. J. G. L. M. 2001, A&A, 369, 574
Vogt, F. P. A., Besel, M.-A., Krause, O., & Dullemond, C. P. 2012, ApJ, 750, 155
Wang, Q., & Helfand, D. J. 1991, ApJ, 373, 497
Warren, J. S., & Hughes, J. P. 2004, ApJ, 608, 261
Warren, J. S., Hughes, J. P., & Slane, P. O. 2003, ApJ, 583, 260
Warth, G., Sasaki, M., Kavanagh, P. J., et al. 2014, A&A, 567, A136
Watson, M. G., Schröder, A. C., Fyfe, D., et al. 2009, A&A, 493, 339
Westerlund, B. E. 1997, The Magellanic Clouds (Cambridge University Press)
Westerlund, B. E., & Mathewson, D. S. 1966, MNRAS, 131, 371
Williams, R. M., & Chu, Y.-H. 2005, ApJ, 635, 1077
Williams, R. M., Chu, Y.-H., Dickel, J. R., et al. 1999a, ApJS, 123, 467
Williams, R. M., Chu, Y.-H., Dickel, J. R., et al. 1999b, ApJ, 514, 798
Williams, R. M., Chu, Y.-H., Dickel, J. R., et al. 2005, ApJ, 628, 704
Williams, B. F., Wold, B., Haberl, F., et al. 2015, ApJS, 218, 9
Wilms, J., Allen, A., & McCray, R. 2000, ApJ, 542, 914
Wong, T., Hughes, A., Ott, J., et al. 2011, ApJS, 197, 16
Woosley, S. E., & Kasen, D. 2011, ApJ, 734, 38
Yamaguchi, R., Mizuno, N., Onishi, T., Mizuno, A., & Fukui, Y. 2001a, ApJ, 553, L185
Yamaguchi, R., Mizuno, N., Onishi, T., Mizuno, A., & Fukui, Y. 2001b, PASJ, 53, 959
Yamaguchi, H., Badenes, C., Petre, R., et al. 2014, ApJ, 785, L27
Zaritsky, D. 2004, ApJ, 614, L37
Zaritsky, D., Harris, J., Thompson, I. B., & Grebel, E. K. 2004, AJ, 128, 1606
Zhang, N.-X., Chu, Y.-H., Williams, R. M., et al. 2014, ApJ, 792, 58
Zhao, H., & Evans, N. W. 2000, ApJ, 545, L35

Appendix A: The EPIC background

The signal recorded in an *XMM-Newton* observation comprises many components, which can be separated into three main groups: the X-ray emission of the target of the observation, an astrophysical X-ray background (hereafter AXB, i.e. X-rays from any source located *in projection* near the target), and an instrumental background. In this Appendix we describe the last two components.

The instrumental background of EPIC: it consists of three components. The first is an *electronic noise*, in the form of hot pixels/columns or read-out noise. In the case of EPIC-pn, the read-out noise increases dramatically below energies of $\lesssim$300 eV, especially if double-pixel events are used.

The second component is the *particle-induced background*, the spectrum of which includes both a continuum and many lines. The continuum part is due to the quiescent particle background (QPB). Cosmic rays deposit a large amount of energy ($\gg$10 keV) in many adjacent pixels and are easy to distinguish from valid X-ray events. However, the unrejected fraction of direct and Compton-scattered cosmic rays produces a remaining continuum with a rather flat spectrum and a rate of 0.021 ± 0.0022 events cm^{-2} s^{-1} for the MOS cameras, and about twice as much for pn (Lumb et al. 2002). The continuum is both chip-, position-, and time-dependent (at least for MOS where it has been extensively studied, see Kuntz & Snowden 2008). These variations have to be taken into account in the spectral analysis. The line part of the particle background is composed of many X-ray fluorescence lines produced by the interaction of high-energy particles with the material surrounding the detectors (Al, Ni, Cu, etc.). Due to this origin the fluorescence line component varies with time. This component is highly position-dependent, mirroring the distribution of the camera material around the detectors (Lumb et al. 2002; Freyberg et al. 2004; Kuntz & Snowden 2008).

The third component is the so-called *soft proton contamination* (SPC). Low-energy protons, accelerated in the Earth magnetosphere and focused by the X-ray telescopes onto the detectors, produce events that cannot be distinguished from genuine X-ray events. The soft proton flux has a highly time-variable, "flaring" nature. At times of the strongest flares, most of the data are unusable anyway (except in the case of a very bright target). But soft proton flares can occur on longer time scales, at lower amplitudes. These time intervals are typically used for science, though they include a small but potentially important contamination by soft protons (hence the term "SPC"). The flaring spectrum was found by Kuntz & Snowden (2008) to be rather flat, with a small roll-off at high energy. The same authors showed that the stronger the flare, the flatter (i.e. harder) the SPC spectrum.

The contribution of the instrumental background will be relatively higher in spectra of sources with low surface brightness and must be taken into account, i.e. modelled. To do so, we use the FWC data (Sect. 2.2). Several hundred kiloseconds worth of data are now available, providing a good knowledge of the spectrum of the instrumental background. As part of his PhD thesis, Richard Sturm (2012) developed an empirical model of the EPIC-pn FWC data. This includes an exponential decay (modified by a spline function), a power law, and a combination of Gaussian lines to account for the electronic noise, QPB, and instrumental lines, respectively. In addition, two smeared absorption edges to the continuum are included.

We extended his work and developed a similar model for the EPIC-MOS FWC spectra. This allows joint analyses of the pn and MOS spectra of LMC SNRs and take advantage of the better spectral resolution of MOS. There is no low-energy noise as for EPIC-pn, so no exponential decay function is needed. Satisfactory results were obtained with a broken power law for the continuum, leaving the slope of the two segments as well as the energy of the break free. A smeared absorption edge around $E \approx 0.53$ keV (K edge of oxygen) improved the fit and was included. A set of Gaussian are used to model the fluorescence lines. The materials of the MOS and pn cameras are different, and so is the observed fluorescence line pattern. Both have a strong Al K line at 1.49 keV. MOS background also features a strong Si K line at 1.74 keV, as opposed to pn, where the strongest line is Cu K at 8.05 keV. Other lines from Au, Cr, Mn, Zn, Cu, Fe, and Ni are detected (Lumb et al. 2002; Kuntz & Snowden 2008) and included in the MOS detector background model.

Note that the same screening and filtering criteria used for the science data are applied to the FWC data, including the vignetting correction with `evigweight` (Sect. 4.2.2). Formally, the instrumental background is *not* subjected to vignetting, which is an effect of the telescope on *photons*. However, by applying a vignetting correction to the science data, one assigns weights to genuine X-ray events as well as to particle background events, since one cannot a priori distinguish the two type of events. Therefore, one needs to vignetting-correct the FWC data to make sure that the FWC spectra, used for the modelling of the instrumental background contribution to the science data, have been processed in the same way as the latter. At a given position on the detector, `evigweight` will assign heavier weights to photons with higher energies, an effect that can be easily accounted for in the background model. To do so, we added a spline function to the pn and MOS instrumental background models. This reproduces the effect of the vignetting correction, which "overweights" events above 5 keV, if they have been recorded at significant off-axis angles.

The astrophysical X-ray background: the AXB can usually be modelled with four or less components (Snowden et al. 2008; Kuntz & Snowden 2010). The soft part of the AXB ($E \lesssim 2$ keV) has mostly a thermal emission spectrum and originates from various regions/hot plasmas. The Local Hot Bubble (LHB) is a region in the solar neighbourhood filled with million-degree plasma ($kT \approx 85$ eV, Henley & Shelton 2008). This component was modelled with an unabsorbed APEC model. Emission from the Galactic halo comprises a cool ($kT \sim 0.1$ keV) and warm ($kT \sim 0.25$ keV) thermal component. Since the cool component is mostly absorbed by the foreground Galactic absorbing column, we did not include it in the AXB model to keep it as simple as possible. For the warm component we used an absorbed APEC model.

Above 2 keV, the background is mostly from the cosmic X-ray background (CXB), a superposition of unresolved distant objects, in other words AGN. This component has an absorbed power-law spectrum, with a photon index fixed at $\Gamma = 1.46$ (Chen et al. 1997). To account for the non-uniformity of this component, the normalisation is a free parameter in our background model.

Note: Cases with a problematic background Several situations can occur where the instrumental and X-ray backgrounds cannot be properly accounted for at first, hindering the analysis of the SNR emission.

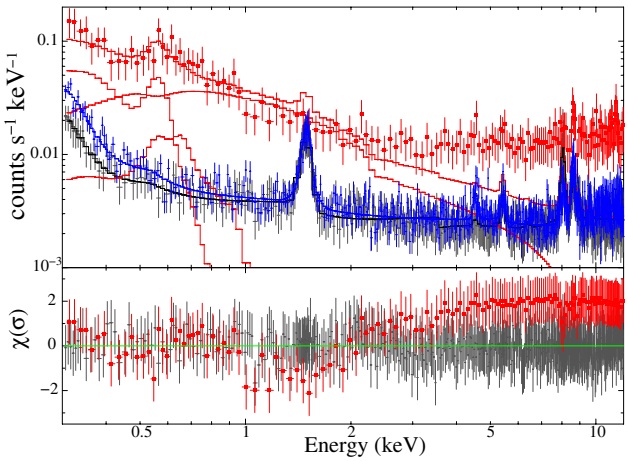

Fig. A.1. Example of a strong soft proton contamination (SPC) affecting the spectral analysis of MCSNR J0529−6653 (ObsID 0700381101). The instrumental background, extracted from FWC data, is shown in the *top panel* in grey and blue. The spectrum extracted from the BG region is shown in red. The strong flat tail above 2 keV is the SPC, which the instrumental + AXB model cannot account for.

- Bad extraction region: if the SNR is very bright, a background spectrum extracted too close to the SNR will include contamination from the telescope PSF wings. Alternatively, a nearby bright X-ray source can produce artefacts such as singly reflected photons up to large angular distances (∼1°). When this happens, we selected the background in another region better suited.
- Anomalous MOS states: the model for the instrumental background of the MOS detectors was developed for data obtained in the normal state; Kuntz & Snowden (2008) identified periods of "anomalous" background of EPIC-MOS. The instrumental background spectrum of this anomalous state is markedly stronger below 1 keV, which complicates the analysis of observations obtained during these epochs. If the SNR affected was faint, including the MOS data usually does not add much information, and only the pn spectrum was used. Conversely, if the SNR is bright, the error induced by fitting the anomalous spectra with the standard model is unimportant, because the source count rate is much higher than the instrumental background, and this issue can be discarded.
- Soft proton contamination: observations affected by a strong SPC are easily identified by fitting the FWC and astrophysical backgrounds spectra together. Indeed, the background above 2 keV is almost purely instrumental. Therefore, a residual component at high energy in the background spectrum (extracted from science observation) that is not present in the FWC spectrum betrays the SPC. An extreme example is shown in Fig. A.1. An extra component needs to be added to the X-ray background and SNR models to account for the SPC.

Appendix B: Selection of SNRs with secured classifications

The list of LMC remants with secured CC and type Ia classifications is given in Table A.1.

B.1. Type Ia SNRs

The spectacular case of MCSNR J0509−6731: one of the few SNRs less than a thousand years old, this object was first typed as a type Ia remnant by Tuohy et al. (1982) based on the Balmer-dominated optical spectrum. This classification was confirmed by the analysis of the *ASCA* spectrum, revealing ejecta emission rich in nucleosynthesis products of thermonuclear SNe (Hughes et al. 1995). Finally, light echoes from the SN, scattered off interstellar dust, were detected around four LMC SNRs (Rest et al. 2005). Optical spectroscopy of the light echoes of MCSNR J0509−6731 allowed Rest et al. (2008) to determine the SN spectral type as an overluminous 1991T-like SN Ia.

Balmer-dominated SNRs with X-ray-detected ejecta: Tuohy et al. (1982) also detected Balmer-dominated emission from MCSNR J0519−6902, J0505−6753 (DEM L71), and J0547−7025, concluding that they were produced by type Ia events. In the two former cases, the X-ray spectra clearly showed emission from the ejecta of thermonuclear SNe (Hughes et al. 1995, 2003; van der Heyden et al. 2003). For J0547−7025, the *Chandra* spectra revealed ejecta but the O/Fe ratio was not as decisive (Hendrick et al. 2003). Furthermore, this remnant was an outlier in Lopez et al. (2009, 2011), with a morphology more consistent with the sample of CC-SNRs. The observations of the *XMM-Newton* survey confirm the iron-rich nature of J0547−7025 (Table E.1), and therefore secure a type Ia classification consistent with the optical data.

Middle-aged to evolved iron-rich SNRs: several remnants with ages exceeding 10^4 yr revealed iron-rich X-ray spectra (observed with *XMM-Newton* and *Chandra*) that betrayed their type Ia nature. MCSNR J0534−6955 was first identified as such with *Chandra* (Hendrick et al. 2003) and *XMM-Newton* observations give similar results (Table E.1). Slightly more evolved, MCSNR J0534−7033 and J0536−7039 (DEM L238 and L249, respectively) have a more pronounced separation of the shell and central iron-rich plasma (Borkowski et al. 2006). The shell A of DEM L316 (MCSNR J0547−6941) has striking spectral differences to the very close neighbour MCSNR J0547−6943 (DEM L316B): the former is also mostly exhibiting Fe L-shell emission, which leads to the interpretation that it is another type Ia remnant (Nishiuchi et al. 2001; Williams & Chu 2005).

Then come three more evolved (age $\gtrsim$15 kyr) iron-rich SNRs that were presented in Maggi et al. (2014) and Bozzetto et al. (2014). Finally, since these publications, we obtained *XMM-Newton* follow-up observations of two remnants, which we classified as type Ia: i) MCSNR J0506−7026 was a ROSAT-selected candidate ([HP99] 1139), which revealed a remnant similar to DEM L238 and L249, about 17−21 kyr old and holding about 0.9 $M_\odot$−1 $M_\odot$ in the central region (Kavanagh et al., in prep., Table E.1); ii) MCSNR J0527−7104 was confirmed by our group in a multi-wavelength study (Kavanagh et al. 2013). A subsequent observation (performed 2014 May 31) revealed yet another iron-rich core (with an unusual morphology, see Kavanagh et al., in prep.), so that this source completes the (currently known) sample of LMC SNRs with a secured type Ia origin.

B.2. Core-collapse SNRs

Remnants hosting a compact object: several neutron stars have been detected inside LMC SNRs, mostly powering a pulsar wind nebula (PWN). MCSNR J0540−6920 is the prototypical example: It hosts the pulsar PSR B0540−69 and is known as a twin of the Crab nebula (Kaaret et al. 2001). MCSNR J0537−6910 (N157B) is also dominated by a PWN around PSR J0537−6910 (Chen et al. 2006). Fainter, less obvious PWNe

Table A.1. LMC remnants with a secured SN classification.

MCSNR	Other name	Age (yr)	Evidence[a]	References[b]
		Core-collapse SNRs		
J0536−6916	SNR 1987A	28	Historical	Maggi et al. (2012b)
J0540−6920	B0540−693	∼1600	Pulsar	Kaaret et al. (2001)
J0525−6938	N132D	∼3150	Ejecta, morphology	Borkowski et al. (2007)
J0535−6602	N63A	2000−5000	Ejecta, Fe K	Warren et al. (2003)
J0536−6913	–	2200−4900	Ejecta	Kavanagh et al. (2015a)
J0505−6802	N23	∼4600	Ejecta, CCO, morphology	Hughes et al. (2006)
J0526−6605	N49	∼4800	Ejecta, SGR, Fe K	Park et al. (2012)
J0537−6910	N157B	∼5000 [c]	PWN	Chen et al. (2006)
J0525−6559	N49B	∼10000	Ejecta, morphology	Park et al. (2003b)
J0536−6735	DEM L241	$>10^4$ [c]	HMXB	Seward et al. (2012)
J0453−6829	B0453−685	12 000−1 5000	PWN, morphology	Haberl et al. (2012a)
J0531−7100	N206	∼25 000	PWN candidate, morphology	Williams et al. (2005)
		Type Ia SNRs		
J0509−6731	B0509−675	400±120	Light echo, ejecta Fe K, morphology	Rest et al. (2008)
J0509−6844	N103B	860	Ejecta, Fe K	Hughes et al. (1995)
J0519−6902	B0519−690	600 ± 200	Ejecta, Fe K, morphology	Hughes et al. (1995)
J0505−6753	DEM L71	∼4700	Ejecta. Fe K, morphology	Hughes et al. (1998, 2003)
J0547−7025	B0548−704	∼7100	Ejecta	Hendrick et al. (2003), this work
J0534−6955	B0534−699	∼10000	Ejecta, morphology	Hendrick et al. (2003)
J0534−7033	DEM L238	∼13500	Ejecta	Borkowski et al. (2006)
J0536−7039	DEM L249	∼15000 [c]	Ejecta	Borkowski et al. (2006)
J0506−7026	[HP99] 1139	17 000−21 000	Ejecta	Kavanagh et al. (in prep.), this work
J0508−6902	[HP99] 791	20 000−25 000	Ejecta	Bozzetto et al. (2014)
J0527−7104	[HP99] 1234	∼25 000	Ejecta	Kavanagh et al. (2013), this work
J0547−6941	DEM L316A	∼27 000 [c]	Ejecta	Williams & Chu (2005)
J0511−6759	–	≳20 000 [c]	Ejecta	Maggi et al. (2014)
J0508−6830	–	≳20 000 [c]	Ejecta	Maggi et al. (2014)

Notes. Ages for the first three type Ia SNRs are from light echo measurements (Rest et al. 2005). [(a)] Morphology: Typed from X-ray morphology by Lopez et al. (2009, 2011). Fe K: Typed from the properties of the Fe K emission by Yamaguchi et al. (2014, see also Sect. 5.4). CCO: Central compact object. PWN: Pulsar wind nebula. SGR: Soft gamma-ray repeater. [(b)] Because of the multiple studies on most remnants, the given references are "see [...] and references therein". [(c)] Uncertain age.

have been found in MCSNR J0453−6829 (Gaensler et al. 2003; Haberl et al. 2012a) and in MCSNR J0535−6602 (Williams et al. 2005). In the latter, the case for a PWN is not as strong; however, analysis of the X-ray morphology using a power-ratio method (Lopez et al. 2009) confirm the classification as CC-SNR.

Chandra observations (Hughes et al. 2006) of MCSNR J0505−6802 (N23) revealed, in addition to regions with enhanced O-group elements, a point source in the centre of the remnant that shows properties similar to compact central objects (CCOs) seen in other CC-SNRs, such as Cas A. Finally, a point source was detected in the "Head" of MCSNR J0536−6735 (DEM L241, see Bamba et al. 2006) using *XMM-Newton* observations and first classified as candidate PWN. With *Chandra* observations, Seward et al. (2012) could show that the source was not extended and identified the optical counterpart as an O5III(f) star. Based on this and the X-ray variability and spectrum, they concluded that the SNR was hosting an HMXB, akin to SXP1062 in the SMC (Hénault-Brunet et al. 2012).

Detection of the remains of massive star nucleosynthesis: MCSNR J0525−6938 (N132D), the brightest SNR in the LMC, belongs to the class of oxygen-rich remnants. Many clumps of X-ray emitting O-ejecta are detected in X-ray observations (Borkowski et al. 2007) and match the optical ejecta morphology seen by *Hubble*. Park et al. (2003b) have revealed a highly enhanced Mg abundance and derived a high mass of Mg ejecta from MCSNR J0525−6559 (N49B), strongly suggesting a massive stellar progenitor. This classification is supported by the X-ray morphology of the remnant (Lopez et al. 2009).

The nearby MCSNR J0526−6605 (N49) is a more puzzling case. No compelling evidence for overabundant O or Fe is found, but Si- and S-rich ejecta features are detected by *Chandra* (Park et al. 2003a, 2012). These can be interpreted as explosive O-burning or incomplete Si-burning deep inside a CC SN explosion; however, the Si/S ejecta mass ratio favour a type Ia origin (Park et al. 2003a, 2012). The soft gamma-ray repeater SGR 0526-66 lies in projection in the remnant, favouring the CC-SNR scenario, although the physical association between the remnant and the SGR is uncertain (Gaensler et al. 2001; Kaplan et al. 2001). The best evidence to terminate the debate over the nature of N49 comes from the properties of its Fe K emission, which is clearly in the region occupied by CC-SNRs (Yamaguchi et al. 2014, Sect. 5.4). MCSNR J0535−6916 (N63A) is another case where ejecta features are detected but cannot yield a definite classification (Warren et al. 2003). As for N49, however, the Fe K emission allows N63A to be included in the sample of secured CC-SNRs.

SNR 1987A: last but not least comes the remnant with the most secured core-collapse classification of all, as the SN itself was observed in detail and its progenitor identified in pre-explosion images.

Appendix C: Sample of SNRs in the LMC

Table C.1. SNRs in the LMC.

MCSNR	RA (J2000)	Dec (J2000)	Other name	X-ray data	L_X	X-ray size	N_H fraction	N_{OB}	r	Hint-spec	Ref.
(1)	(2)	(3)	(4)	(5)	(6)	(7)	(8)	(9)	(10)	(11)	(12)
J0448−6700	04:48:22	−66:59:52	[HP99] 460	R	0.46	220	–	3	$1.67^{+0.92}_{-0.20}$	3	BGS06
J0449−6920	04:49:20	−69:20:20		X	0.07	162 (85)	$2.33^{+0.93}_{-0.70}$	26	$6.29^{+2.33}_{-2.66}$	3	KPS10
J0450−7050	04:50:27	−70:50:15	B0450-709	X	0.59	340 (85)	$0.93^{+0.68}_{-0.56}$	2	$1.89^{+0.29}_{-0.39}$	3	MFT85
J0453−6655	04:53:14	−66:55:13	N4	X	1.17	256 (122)	$0.60^{+0.33}_{-0.29}$	83	$6.36^{+7.24}_{-2.85}$	3	SCM94
J0453−6829	04:53:38	−68:29:27	B0453-685	X	13.85	120	$0.54^{+0.08}_{-0.25}$	5	$2.42^{+0.46}_{-0.39}$	5	LHG81
J0454−6713	04:54:33	−67:13:13	N9	C	1.58	216 (5)	1.32	72	$9.69^{+5.26}_{-5.34}$	3	SCM94
J0454−6626	04:54:49	−66:25:32	N11L	X	0.63	106 (50)	$0.35^{+0.23}_{-0.22}$	33	$5.84^{+0.58}_{-2.39}$	3	MC73
J0455−6839	04:55:37	−68:38:47	N86	R	1.42	366	–	16	$2.66^{+0.23}_{-0.51}$	3	MC73
J0459−7008	04:59:55	−70:07:52	N186D	C	1.09	114	$0.93^{+0.42}_{-0.25}$	51	$3.73^{+0.87}_{-0.98}$	3	MC73
J0505−6753	05:05:42	−67:52:39	DEM L71	X	44.59	76 (5)	0.22 ± 0.01	13	$2.38^{+0.53}_{-0.52}$	1	LHG81
J0505−6802	05:05:55	−68:01:47	N23	MX	26.25	96	$0.81^{+0.25}_{-0.06}$	26	$2.7^{+0.47}_{-0.76}$	3	MC73
J0506−6541	05:06:05	−65:41:08	DEM L72	X	0.53	410 (170)	$0.39^{+0.50}_{-0.39}$	12	$1.00^{+0.08}_{-0.40}$	4	KPS10
J0506−7026	05:06:50	−70:25:53	[HP99] 1139	X	1.44	262 (10)	0(<0.11)	82	$3.08^{+0.57}_{-0.83}$	1	in prep.
J0508−6902	05:08:37	−69:02:54	[HP99] 791	X	0.37	304 (33)	0(<0.48)	22	$1.27^{+0.04}_{-0.11}$	1	BKM14
J0508−6830	05:08:50	−68:30:50	J0508-6830	X	0.09	138 (160)	0(<0.7)	27	$3.09^{+0.69}_{-0.51}$	1	MHK14
J0509−6844	05:08:59	−68:43:35	N103B	X	51.7	30	$1.16^{+0.08}_{-0.04}$	99	$6.18^{+0.63}_{-1.31}$	2	MC73
J0509−6731	05:09:31	−67:31:17	B0509-67.5	X	16.51	31.8	$1.42^{+0.06}_{-0.06}$	2	$1.86^{+0.26}_{-0.41}$	1	LHG81
J0511−6759	05:11:11	−67:59:08		MX	0.16	112	0(<1.08)	3	$1.23^{+0.04}_{-0.43}$	1	MHK14
J0512−6707	05:12:27	−67:07:18	[HP99] 483	X	0.09	120 (45)	$0.28^{+0.38}_{-0.23}$	25	$5.56^{+1.2}_{-2.66}$	3	KSB15b
J0513−6912	05:13:14	−69:12:20	DEM L109	X	0.51	240 (155)	$0.56^{+0.25}_{-0.43}$	16	$1.64^{+0.23}_{-0.30}$	3	MFT85
J0514−6840	05:14:16	−68:40:22		MX	0.4	220	0(<0.05)	7	$1.05^{+0.16}_{-0.27}$	3	MHK14
J0517−6759	05:17:08	−67:59:29		X	0.24	324 (30)	$1.44^{+1.98}_{-1.19}$	12	$6.37^{+2.01}_{-3.23}$	3	MHK14

Notes. Sample of SNRs in the LMC. The columns are the following: (1) MCSNR identifier, in the form "JHHMM−DDMM". (2) Right ascension of the remnant, in J2000 equinox. (3) Declination in J2000 equinox. (4) Old "common" name used in the literature. (5) Flag coding the type of X-ray data available and used in this work. "X" indicates that *XMM-Newton* data are present, and "MX" that multiple *XMM-Newton* observation of the remnant exist. "C" or "R" are used when no *XMM-Newton* observations are available but *Chandra* or ROSAT observations were used, respectively. "N" means that no X-ray information was found. (6) L_X, the X-ray luminosity in the 0.3 keV−8 keV band, in units of 10^{35} erg s^{-1}, obtained as described in Sect. 7. (7) X-ray size in arcsec. Only the *maximal* extent is given (corresponding to the diametre in a circularly symmetric case). The number in brackets gives the position angle (PA) of the maximal extent in the non-symmetric case. The PA is measured in degrees, eastwards of north. Size was measured from *XMM-Newton* images whenever applicable ("X" and "MX" flags). For "C" SNRs, the quoted value is taken from the entry in the *Chandra* SNR catalogue. For the ROSAT-only SNRs (J0448−6700 and J0455−6839), we used the value quoted in Badenes et al. (2010) and Williams et al. (1999a), respectively. (8) N_H fraction, as defined in Sect. 8. Uncertainties are given at the 90 % C.L. (9) N_{OB}, the number of blue early-type stars within 100 pc of the remnant (see Sect. 6.2). (10) r, the ratio of CC SNe to thermonuclear SNe expected from the observed distribution of stellar ages in the neighbourhood of the remnant, as obtained by Eq. (2) (see Sect. 6 for details). (11) "Hint-spec", the number attributed to SNRs as function of spectral results, as described in Sect. 6.3 and Table 7.

References. In which the SNR was first published: WM66: Westerlund & Mathewson (1966); MC73: Mathewson & Clarke (1973); LHG81: Long et al. (1981); MFD83: Mathewson et al. (1983); TM84: Turtle & Mills (1984); MFD84: Mathewson et al. (1984); MFT85: Mathewson et al. (1985); CMG83: Chu et al. (1993); SCM94: Smith et al. (1994); CDS95: Chu et al. (1995); CKS97: Chu et al. (1997); BGS06: Blair et al. (2006); KPS10: Klimek et al. (2010); GSH12: Grondin et al. (2012); BFC12a: Bozzetto et al. (2012a); BFC12b: Bozzetto et al. (2012b); DFB12: de Horta et al. (2012); MHB12: Maggi et al. (2012a); KSP13: Kavanagh et al. (2013); BFC13: Bozzetto et al. (2013); MHK14: Maggi et al. (2014); BKM14: Bozzetto et al. (2014); KSB15a: Kavanagh et al. (2015a); KSB15b: Kavanagh et al. (2015c).

Table C.1. continued.

MCSNR	RA (J2000)	Dec (J2000)	Other name	X-ray data	L_X	X-ray size	N_H fraction	N_{OB}	r	Hint-spec	Ref.
(1)	(2)	(3)	(4)	(5)	(6)	(7)	(8)	(9)	(10)	(11)	(12)
J0518−6939	05:18:41	−69:39:12	N120	MX	0.88	148 (110)	0(<0.75)	133	$4.57^{+0.52}_{-0.96}$	3	MC73
J0519−6902	05:19:35	−69:02:09	B0519-690	MX	34.94	33.6	$0.63^{+0.03}_{-0.03}$	13	$1.71^{+0.26}_{-0.34}$	1	LHG81
J0519−6926	05:19:44	−69:26:08	B0520-694	X	2.69	190 (140)	0(<0.05)	114	$3.41^{+0.09}_{-0.51}$	5	MFD83
J0521−6543	05:21:39	−65:43:07	DEM L142	N	–	168	–	36	$5.97^{+0.30}_{-3.07}$	3	BGS06
J0523−6753	05:23:07	−67:53:12	N44	X	0.9	255 (90)	$0.21^{+0.13}_{-0.10}$	99	$6.17^{+2.61}_{-3.15}$	5	CMG93
J0524−6624	05:24:20	−66:24:23	DEM L175a	N	–	240	–	39	$6.88^{+13.1}_{-3.34}$	3	MFT85
J0525−6938	05:25:04	−69:38:24	N132D	X	315.04	126 (60)	$0.45^{+0.02}_{-0.02}$	56	$2.72^{+0.13}_{-0.35}$	5	WM66
J0525−6559	05:25:25	−65:59:19	N49B	X	38.03	170	$0.95^{+0.09}_{-0.08}$	33	$4.42^{+1.43}_{-1.76}$	5	MC73
J0526−6605	05:26:00	−66:04:57	N49	X	64.37	84	$0.64^{+0.04}_{-0.04}$	37	$6.33^{+3.99}_{-2.72}$	5	WM66
J0527−6912	05:27:39	−69:12:04	B0528-692	MX	1.99	198 (142)	0(<0.05)	224	$7.59^{+0.29}_{-2.74}$	4.5	MFD84
J0527−6550	05:27:54	−65:49:38	DEM L204	N	–	282	–	9	$1.54^{+0.40}_{-0.50}$	3	LHG81
J0527−6714	05:27:56	−67:13:40	B0528-6716	X	0.25	270 (40)	2.28	97	$11.12^{+4.37}_{-6.42}$	3	TM84
J0527−7104	05:27:57	−71:04:30	[HP99] 1234	X	0.21	369 (155)	$0.66^{+0.48}_{-0.16}$	6	$2.4^{+0.52}_{-0.52}$	1.5	KSP13
J0528−6727	05:28:05	−67:27:20	DEM L205	X	0.58	324 (40)	0(<0.18)	142	$8.97^{+1.91}_{-4.9}$	3	MHB12
J0529−6653	05:29:51	−66:53:28	DEM L214	X	1.04	145 (140)	$0.96^{+0.74}_{-0.79}$	222	$14.12^{+13.7}_{-8.61}$	4.5	BFC12a
J0530−7008	05:30:40	−70:07:30	DEM L218	X	0.72	325 (50)	$0.29^{+0.36}_{-0.22}$	19	$1.97^{+0.16}_{-0.12}$	3	DFB12
J0531−7100	05:31:56	−71:00:19	N206	X	2.55	180 (90)	$0.20^{+0.25}_{-0.16}$	49	$5.36^{+0.79}_{-1.95}$	4.5	MC73
J0532−6732	05:32:30	−67:31:33	B0532-675	X	2.48	285 (145)	$0.54^{+0.43}_{-0.32}$	173	$8.07^{+3.56}_{-3.83}$	3	MFT85
J0533−7202	05:33:46	−72:02:59	1RXSJ053353.6-7204	X	0.57	205 (85)	$0.26^{+0.24}_{-0.23}$	1	$0.8^{+0.17}_{-0.37}$	2	BFC13
J0534−6955	05:34:02	−69:55:03	B0534-699	X	6.33	135 (35)	$0.92^{+0.07}_{-0.11}$	8	$1.18^{+0.05}_{-0.13}$	1	LHG81
J0534−7033	05:34:18	−70:33:26	DEM L238	X	1.55	186 (110)	0(<0.02)	4	$2.07^{+0.2}_{-0.24}$	1	LHG81
J0535−6916	05:35:28	−69:16:11	SNR1987A	MX	27.39	1.62	$1.16^{+0.03}_{-0.05}$	84	$5.85^{+1.28}_{-1.87}$	4	historical
J0535−6602	05:35:44	−66:02:14	N63A	X	185.68	84	$0.46^{+0.05}_{-0.03}$	45	$3.95^{+0.73}_{-1.47}$	5	WM66
J0535−6918	05:35:46	−69:18:02	Honeycomb	MX	0.4	105 (155)	0.90 ± 0.12	108	$8.32^{+2.40}_{-3.05}$	3.5	CDS95
J0536−6735	05:36:03	−67:34:36	DEM L241	X	3.84	310 (155)	$0.66^{+0.06}_{-0.06}$	39	$2.71^{+0.55}_{-0.53}$	5	MFT85
J0536−7039	05:36:07	−70:38:37	DEM L249	MX	1.43	200 (35)	0(<0.03)	2	$1.56^{+0.10}_{-0.10}$	1	LHG81
J0536−6913	05:36:17	−69:13:28	B0536-6914	MX	0.22	66 (90)	$1.11^{+0.11}_{-0.75}$	92	$5.85^{+1.28}_{-1.87}$	4.5	KSB15a
J0537−6628	05:37:27	−66:27:50	DEM L256	X	0.32	227 (42)	$0.25^{+0.50}_{-0.25}$	48	$1.62^{+0.07}_{-0.17}$	2	KPS10
J0537−6910	05:37:46	−69:10:28	N157B	MX	15.0	120	$1.73^{+0.06}_{-0.06}$	83	$19.56^{+8.02}_{-11.0}$	5	MC73
J0540−6944	05:39:59	−69:44:02	N159	X	0.43	92 (110)	$1.92^{+0.20}_{-0.15}$	60	$3.53^{+0.62}_{-0.85}$	3	CKS97
J0540−6920	05:40:11	−69:19:55	B0540-693	X	87.35	72	$1.58^{+0.04}_{-0.04}$	119	$24.41^{+19.1}_{-15.8}$	5	MC73
J0541−6659	05:41:51	−66:59:04	[HP99] 456	X	0.77	300	0(<0.06)	10	$2.08^{+0.04}_{-0.29}$	3	GSH12
J0543−6858	05:43:08	−68:58:18	DEM L299	X	1.68	330 (55)	$0.4^{+0.13}_{-0.05}$	38	$4.98^{+2.88}_{-1.95}$	3	LHG81
J0547−6943	05:46:59	−69:42:50	DEM L316B	X	1.47	190 (95)	$0.63^{+0.19}_{-0.12}$	0	$1.03^{+0.26}_{-0.56}$	3	MC73
J0547−6941	05:47:22	−69:41:26	DEM L316A	X	1.26	190 (170)	$0.92^{+0.24}_{-0.20}$	0	$1.03^{+0.26}_{-0.56}$	1	MC73
J0547−7025	05:47:49	−70:24:54	B0548-704	X	2.94	118 (75)	$0.88^{+0.11}_{-0.10}$	3	$0.72^{+0.20}_{-0.26}$	1	MFD83
J0550−6823	05:50:30	−68:22:40		C	1.22	312 (90)	1.22	4	$2.04^{+0.20}_{-0.39}$	3	BFC12b

Appendix D: Spectra of SNRs observed with *XMM-Newton* for the first time

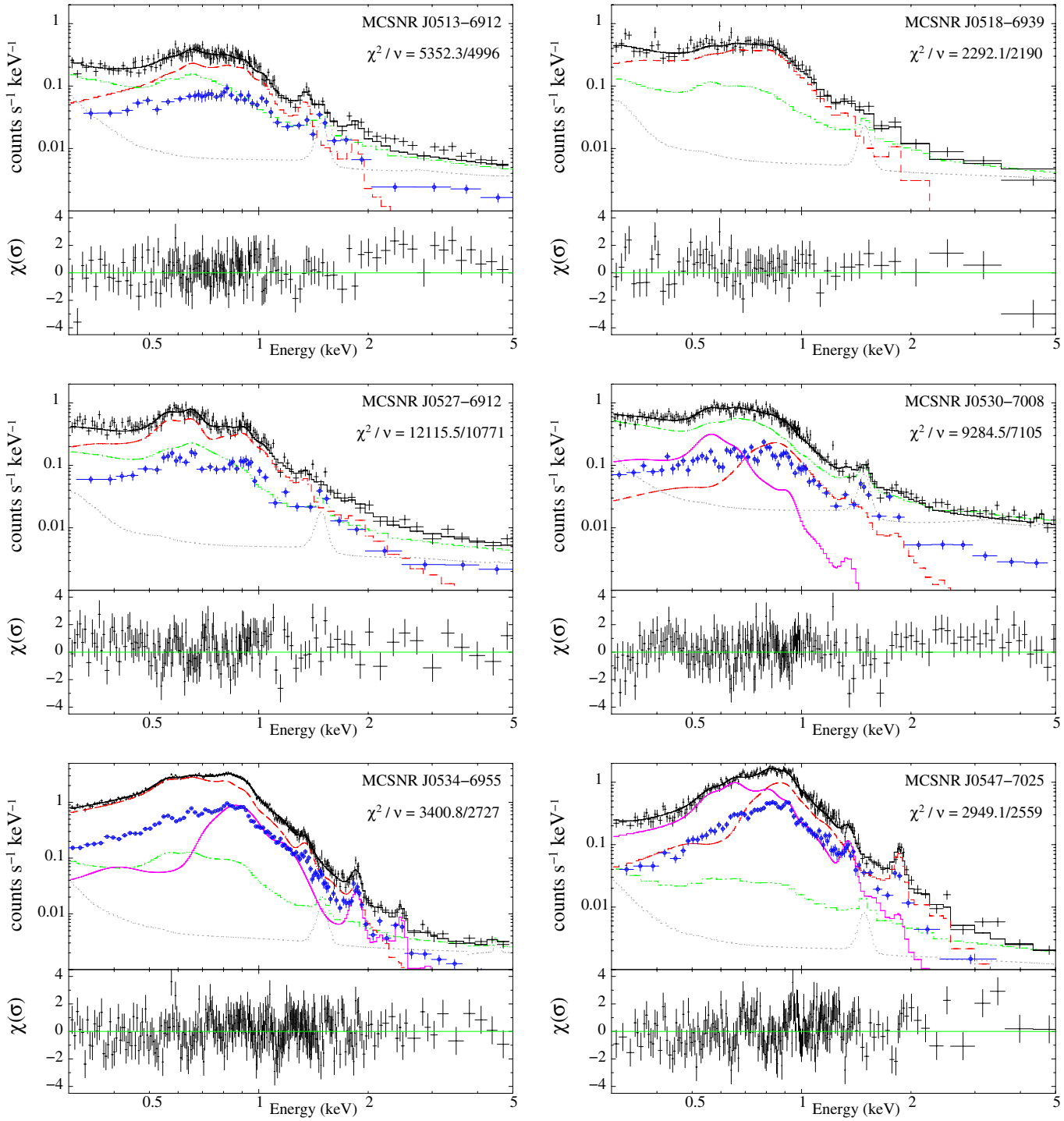

Fig. D.1. *XMM-Newton* EPIC spectrum of SNRs for which none have been published yet (see Sect. 5.1). The SNR names are labelled on each plot. The pn and MOS1 data are shown in black and blue points, respectively. MOS2 data are not shown for clarity. The total best-fit model (see parameters in Table E.1), convolved with the pn response, is shown as the solid black line. It includes: i) the instrumental background component with a dotted grey line (only pn shown); ii) the total AXB model (see Appendix A) with a dot-dashed green line; and iii) the SNR emission with a dashed red line. When a second component is used (Table E.1), it is shown with a solid magenta line. The lower panels show the pn residuals (in terms of σ) for the total best-fit model. For MCSNR J0527−6712 data from two observations were used, though only one spectra is shown for clarity.

Appendix E: SNR X-ray spectral results

Table E.1. X-ray spectral results of LMC SNRs.

	Component 1					Component 2					χ^2/ν $(\chi^2_{\rm red})$
MCSNR	$N_{\rm H\ LMC}$ (10^{21} cm^{-2})	kT (keV)	τ (10^{11} s cm^{-3})	EM (10^{58} cm^{-3})	Abundances	$N_{\rm H\ LMC}$ (10^{21} cm^{-2})	kT (keV)	τ (10^{11} s cm^{-3})	EM (10^{58} cm^{-3})	Abundances	
(1)	(2)	(3)	(4)	(5)	(6)	(7)	(8)	(9)	(10)	(11)	(12)
J0449−6920	$6.97^{+2.77}_{-2.08}$	$0.20^{+0.05}_{-0.12}$	CIE	$18.3^{+359}_{-16.3}$	RD92			–			1985.3/1863 (1.07)
J0450−7050[a]	$1.31^{+0.95}_{-0.79}$	0.24 ± 0.02	CIE	$33.6^{+36.8}_{-24.1}$	O: $0.20^{+0.14}_{-0.08}$ Ne: $0.40^{+0.33}_{-0.07}$ Mg: 0.20 (<0.48)			–			4669.4/3294 (1.42)
J0453−6655	$1.10^{+0.61}_{-0.54}$	$0.36^{+0.10}_{-0.08}$	$1.38^{+2.07}_{-0.63}$	$30.7^{+36.9}_{-15.6}$	O: $0.13^{+0.05}_{-0.04}$ Ne: $0.12^{+0.07}_{-0.05}$ Mg: $0.15^{+0.20}_{-0.01}$ Fe: $0.29^{+0.12}_{-0.08}$			–			4460.9/4214 (1.06)
J0453−6829[b]	$0.93^{+0.13}_{-0.43}$	$0.37^{+0.03}_{-0.05}$	$1.58^{+0.51}_{-0.24}$	$27.2^{+16.28}_{-3.56}$	O: 0.17 ± 0.01 Ne: $0.25^{+0.03}_{-0.01}$ Mg: 0.37 ± 0.05 Si: $0.61^{+0.24}_{-0.23}$ Fe: $0.28^{+0.03}_{-0.02}$			–			2156.2/1860 (1.16)
J0454−6626	$1.15^{+0.76}_{-0.71}$	$0.34^{+0.09}_{-0.07}$	$1.17^{+1.48}_{-0.70}$	$1.67^{+1.38}_{-0.99}$	O: $0.14^{+0.07}_{-0.05}$ Mg: 0.15(<0.39) Fe: $0.26^{+0.10}_{-0.08}$			–			2136.8/1811 (1.18)
J0505−6802[c]	$1.58^{+0.49}_{-0.11}$	$0.32^{+0.02}_{-0.03}$	$3.40^{+2.26}_{-1.62}$	$107.4^{+76.1}_{-16.3}$	O: $0.11^{+0.03}_{-0.04}$ Ne: 0.16 ± 0.02 Mg: 0.18 ± 0.03 Si: $0.37^{+0.05}_{-0.06}$ Fe: $0.20^{+0.06}_{-0.03}$	1.58	$1.09^{+0.07}_{-0.09}$	$2.46^{+0.96}_{-0.48}$	$6.50^{+12.0}_{-0.60}$	–	454.4/407 (1.12)
J0506−6541	0.59(<1.34)	0.18 ± 0.01	CIE	$2.27^{+1.35}_{-0.71}$	Ne: $1.26^{+0.41}_{-0.28}$			–			8549.4/7232 (1.18)
J0506−7026	<0.12	$0.70^{+0.09}_{-0.02}$	$1.99^{+0.79}_{-0.90}$ (1.08)	0.61±0.09	O: $0.33^{+0.07}_{-0.05}$ Ne: $0.42^{+0.19}_{-0.17}$ Mg: $0.22^{+0.14}_{-0.13}$ Fe: $1.49^{+0.17}_{-0.23}$			–			9026.4/8365 (1.08)

Notes. Columns are described in Sect. 5.1. [(a)] Only MOS data available. [(b)] Fit includes a power-law component for the central PWN. [(c)] Same absorption column and abundances in the two components; nitrogen abundance is also fitted to 0.07 solar. [(d)] Results from MHK14. [(e)] Results from BKM14. The first component is a Sedov model. The second is split into two pure-metal components (O and Fe) with the corresponding emission measures given as $\mathrm{EM_X} \times (n_{\rm X}/n_{\rm H})$. [(f)] Same absorption column and abundances in the two components; fit includes a power-law component for SGR 0526−66 (Park et al. 2012). [(g)] $N_{\rm H\ LMC}$ fixed to the value from the H I map of the LMC. [(h)] Abundances from RD92 are scaled by a common factor. [(i)] Affected by strong background flare. [(j)] The second component comprises three pure-metals NEI models with a common temperature and distinct τ and EM, for each Si, S, and Fe. [(k)] C, N, O, and Ne abundances of the iron-rich component (Component 1) are fixed to 0. [(l)] Abundance of Ca fixed at 0 in the second component; fit includes an Fe K (Gaussian) line, see Sect. 5.4. [(m)] Fit includes a power-law component for the interior HMXB (Seward et al. 2012). [(n)] Elements other than O, Ne, Mg, and Si in the second component are set to 0. [(o)] C, N, and O abundances of the iron-rich component (Component 2) are fixed to 0. [(p)] Fit includes a power-law component for the interior PWN. [(q)] Strongly affected by the emission from PSR 0540−69.3 (modeled by a power law). [(r)] Dominated by the contamination from LMC X-1 (modeled by a power law). [(s)] Same absorption column and abundances in the two components. † These SNRs were observed with *XMM-Newton* EPIC instruments for the first time over the course of this work. Their spectra are shown in Fig. D.1.

Table E.1. continued.

	Component 1					Component 2					χ^2/ν $(\chi^2_{\rm red})$
MCSNR	$N_{\rm H\ LMC}$ (10^{21} cm^{-2})	kT (keV)	τ (10^{11} s cm^{-3})	EM (10^{58} cm^{-3})	Abundances	$N_{\rm H\ LMC}$ (10^{21} cm^{-2})	kT (keV)	τ (10^{11} s cm^{-3})	EM (10^{58} cm^{-3})	Abundances	
(1)	(2)	(3)	(4)	(5)	(6)	(7)	(8)	(9)	(10)	(11)	(12)
J0508−6830[d]	<1.80	$0.71^{+0.06}_{-0.07}$	CIE	$1.0(^{+700}_{-0.4})\times10^{-4}$	O: 0 Fe: 792.9(>1.1)			–			1488.3/1554 (0.96)
J0508−6902[e]	<0.8	$0.41^{+0.05}_{-0.06}$	$27.0^{+42.2}_{-9.7}$	$0.48^{+0.25}_{-0.22}$	RD92	0	0.78 ± 0.03	CIE	<48.8 0.16 ± 0.01	pure O pure Fe	267.1/219 (1.22)
J0511−6759[d]	<2.10	$0.65^{+0.05}_{-0.04}$	CIE	$1.2(^{+8.0}_{-1.0})\times10^{-2}$	O: 0 Fe: 11.4(>4.7)			–			707.5/692 (1.02)
J0512−6707	$0.82^{+1.09}_{-0.68}$	0.24 ± 0.01	CIE	$0.15^{+0.17}_{-0.08}$	RD92			–			3059.4/2083 (1.47)
J0513−6912 †	$1.34^{+0.59}_{-1.02}$	0.43±0.08	$10.9^{+37.3}_{-6.66}$	$1.28^{+1.67}_{-0.89}$	O: $0.27^{+0.23}_{-0.08}$ Ne: $0.46^{+0.57}_{-0.13}$ Mg: $0.75^{+0.34}_{-0.22}$ Si: $1.33^{+0.79}_{-0.50}$ Fe: $0.20^{+0.23}_{-0.04}$			–			5352.3/4996 (1.07)
J0514−6840[d]	<0.09	0.30 ± 0.01	$2.60^{+0.60}_{-0.50}$	0.51 ± 0.03	O: 0.28 ± 0.03 Fe: $0.38^{+0.13}_{-0.11}$			–			8005.3/7957 (1.01)
J0517−6759[d]	$3.5^{+4.8}_{-2.9}$	$0.1^{+0.04}_{-0.02}$	CIE	$11.2^{+7.2}_{-9.0}$	RD92	<1.7	$0.59^{+0.05}_{-0.04}$	CIE	$0.19^{+0.002}_{-0.02}$	RD92	2558.9/2547 (1.00)
J0518−6939 †	<1.16	$0.44^{+0.30}_{-0.09}$	$4.91^{+15.0}_{-3.62}$	$1.53^{+1.43}_{-1.08}$	O: $0.14^{+0.06}_{-0.07}$ Ne: 0.23 ± 0.15 Mg: $0.31^{+0.42}_{-0.26}$ Si: $0.96^{+1.63}_{-0.90}$ Fe: $0.27^{+0.34}_{-0.10}$			–			2292.1/2190 (1.05)
J0519−6926	<0.09	$0.39^{+0.06}_{-0.04}$	$3.58^{+1.65}_{-1.62}$	$4.53^{+1.65}_{-0.86}$	O: $0.15^{+0.01}_{-0.02}$ Ne: $0.36^{+0.04}_{-0.05}$ Mg: 0.34 ± 0.10 Si: $1.21^{+0.32}_{-0.36}$ Fe: 0.21 ± 0.03			–			3602.5/3033 (1.19)
J0523−6753	$0.75^{+0.45}_{-0.35}$	0.62 ± 0.04	$22.7^{+11.0}_{-10.2}$	$0.66^{+0.02}_{-0.09}$	O: $1.49^{+0.86}_{-0.80}$ Ne: $3.08^{+2.03}_{-1.63}$ Mg: $1.57^{+0.79}_{-0.76}$ Si: 1.13 ± 0.43 Fe: 0.48 ± 0.16			–			5075.9/4532 (1.12)
J0525−6559	$2.17^{+0.20}_{-0.19}$	$0.60^{+0.06}_{-0.04}$	$2.34^{+0.69}_{-0.56}$	$50.3^{+11.3}_{-11.4}$	O: 0.07 ± 0.05 Ne: 0.27 ± 0.04 Mg: 0.43 ± 0.09 Si: 0.33 ± 0.07 Fe: $0.10^{+0.05}_{-0.06}$	2.17	0.32 ± 0.07	$4.34^{+17.7}_{-2.04}$	$43.6^{+45.58}_{-14.0}$	RD92	3981.8/2884 (1.38)

Table E.1. continued.

	Component 1					Component 2					χ^2/ν $\left(\chi^2_{\rm red}\right)$
MCSNR	$N_{\rm H\ LMC}$ (10^{21} cm^{-2})	kT (keV)	τ (10^{11} s cm^{-3})	EM (10^{58} cm^{-3})	Abundances	$N_{\rm H\ LMC}$ (10^{21} cm^{-2})	kT (keV)	τ (10^{11} s cm^{-3})	EM (10^{58} cm^{-3})	Abundances	
(1)	(2)	(3)	(4)	(5)	(6)	(7)	(8)	(9)	(10)	(11)	(12)
J0526−6605[f]	$2.64^{+0.15}_{-0.18}$	0.42 ± 0.02	$5.26^{+0.75}_{-0.41}$	$112.3^{+2.85}_{-3.36}$	O: 0.30 ± 0.03 Ne: $0.42^{+0.02}_{-0.05}$ Mg: $0.52^{+0.08}_{-0.05}$ Si: 1.0 ± 0.11 Fe: $0.41^{+0.02}_{-0.05}$	2.64	$1.04^{+0.04}_{0.05}$	>35.0	$27.4^{+3.03}_{-1.77}$	–	3509.3/2038 (1.72)
J0527−6714[g]	2.0	0.18 ± 0.01	CIE	1.31 ± 0.23	RD92			–			5999.0/5237 (1.15)
J0527−6912[h] †	2.0	0.18 ± 0.01	CIE	1.31 ± 0.23	$0.35^{+0.12}_{-0.06}\times$ RD92			–			12115.5/10771(1.12)
J0527−7104	$1.33^{+0.97}_{-0.32}$	$0.37\ ^{+0.08}_{-0.04}$	$1.33^{+4.57}_{-0.55}$	$0.30^{+0.07}_{-0.13}$	O: $0.05^{+0.04}_{-0.01}$ Ne: $0.86^{+0.29}_{-0.27}$ Fe: $1.43^{+0.71}_{-0.32}$			–			6801.8/5788 (1.18)
J0528−6727	<0.39	0.22±0.02	CIE	$1.70^{+1.80}_{-0.52}$	0: $0.30^{+0.15}_{-0.19}$ Ne: $0.66^{+0.43}_{-0.25}$ Fe: $0.66^{+0.68}_{-0.34}$			–			5510.0/5265 (1.05)
J0529−6653[i]	$0.48^{+0.37}_{-0.40}$	1.51 ± 0.28	$0.30^{+0.24}_{-0.10}$	$0.83^{+0.22}_{-0.18}$	O: 0.09 ± 0.02 Ne: 0.03(<0.05) Mg: 0.07 ± 0.06 Si: 0.21(<0.49) Fe: $0.07^{+0.03}_{-0.02}$			–			1961.3/2987 (0.66)
J0530−7008 †	$0.37^{+0.45}_{-0.28}$	$0.18^{+0.02}_{-0.03}$	CIE	$1.34^{+0.45}_{-0.34}$	RD92	0.37	0.74 ± 0.06	CIE	0.36 ± 0.06	RD92	9284.5/7105 (1.31)
J0531−7100	<0.12	$0.52^{+0.05}_{-0.04}$	$2.50^{+1.70}_{-0.52}$	$1.63^{+0.21}_{-0.16}$	RD92			–			2864.9/2361 (1.20)
J0532−6732	$0.94^{+0.68}_{-0.51}$	$0.53^{+0.29}_{-0.11}$	$0.83^{+0.46}_{-0.24}$	$2.30^{+3.53}_{-1.34}$	O: $0.25^{+0.06}_{-0.05}$ Ne: $0.24^{+0.12}_{-0.07}$ Mg: $0.17^{+0.20}_{-0.14}$ Si: $1.44^{+1.23}_{-0.83}$ Fe: $0.34^{+0.14}_{-0.09}$			–			3824.0/3562 (1.10)
J0533−7202	$0.47^{+0.44}_{-0.41}$	$0.31^{+0.06}_{-0.09}$	$1.39^{+1.16}_{-0.54}$	$1.13^{+0.87}_{-0.63}$	O: $0.27^{+0.03}_{-0.05}$ Ne: $0.37^{+0.07}_{-0.09}$ Mg: <0.18 Fe: $0.37^{+0.17}_{-0.10}$			–			4128.0/3265 (1.26)
J0534−6955[j] †	$2.27^{+0.18}_{-0.26}$	$0.31^{+0.03}_{-0.02}$	$3.04^{+0.66}_{-1.06}$	$26.1^{+10.83}_{-4.81}$	O: 0.14 ± 0.01 Ne: $0.23^{+0.02}_{-0.03}$ Mg: $0.27^{+0.04}_{-0.03}$ Fe: $0.34^{+0.04}_{-0.03}$	2.27	$1.32^{+0.09}_{-0.20}$	pure Si: $\tau = 0.05 \pm 0.01$; EM = $130.6^{+133.3}_{-94.6}$ pure S: $\tau = 0.75^{+4.44}_{-0.51}$; EM = $1.04^{+4.69}_{-0.51}$ pure Fe: $\tau = 0.57^{+0.06}_{-0.04}$; EM = $1.26^{+0.25}_{-0.17}$			3400.8/2727 (1.25)

Table E.1. continued.

	Component 1					Component 2					χ^2/ν $\left(\chi^2_{\rm red}\right)$
MCSNR	$N_{\rm H\ LMC}$ (10^{21} cm^{-2})	kT (keV)	τ (10^{11} s cm^{-3})	EM (10^{58} cm^{-3})	Abundances	$N_{\rm H\ LMC}$ (10^{21} cm^{-2})	kT (keV)	τ (10^{11} s cm^{-3})	EM (10^{58} cm^{-3})	Abundances	
(1)	(2)	(3)	(4)	(5)	(6)	(7)	(8)	(9)	(10)	(11)	(12)
J0534−7033[k]	<0.03)	0.78 ± 0.01	208(>63.1)	$0.87^{+0.14}_{-0.16}$	Mg: 0.30 ± 0.18 Si: 0.08(<0.27) Fe: $1.26^{+0.29}_{-0.24}$	0	$0.27^{+0.07}_{-0.04}$	$2.65^{+35.3}_{-1.35}$	$0.46^{+0.58}_{-0.15}$	RD92	3496.61/2922 (1.20)
J0535−6602[l]	$0.68^{+0.08}_{-0.04}$	0.52 ± 0.01	$7.49^{+2.34}_{-0.90}$	$251.1^{+31.0}_{-10.6}$	O: $0.23^{+0.04}_{-0.05}$ Ne: $0.57^{+0.02}_{-0.05}$ Mg: $0.12^{+0.04}_{-0.03}$ Si: <0.13 Fe: 0.28 ± 0.01	$2.48^{+1.10}_{-0.81}$	$1.10^{+0.04}_{-0.01}$	$10.4^{+3.80}_{-0.90}$	$99.1^{+6.05}_{-8.63}$	O: $0.71^{+0.23}_{-0.31}$ Ne: <0.12 Mg: $0.85^{+0.05}_{-0.07}$ Si: $0.76^{+0.05}_{-0.07}$ S: 0.48 ± 0.05 Fe: <0.02 Ar: 0.14(<0.34)	1962.4/1634 (1.20)
J0535−6918	2.31 ± 0.03	$0.31^{+0.05}_{-0.03}$	$1.71^{+1.09}_{-0.71}$	$1.85^{+0.92}_{-0.71}$	O: $0.15^{+0.04}_{-0.03}$ Ne: $0.34^{+0.09}_{-0.07}$ Mg: $0.34^{+0.18}_{-0.14}$ Si: $1.60^{+1.13}_{-0.86}$ Fe: $0.30^{+0.10}_{-0.07}$			–			1999.9/1589 (1.26)
J0536−6735[m]	2.26 ± 0.20	$0.56^{+0.04}_{-0.03}$	$7.59^{+1.12}_{-1.00}$	$2.00^{+0.67}_{-0.24}$	O: $1.57^{+0.61}_{-0.19}$ Ne: $2.52^{+0.87}_{-0.18}$ Mg: $1.35^{+0.27}_{-0.11}$ Fe: $0.04^{+0.09}_{-0.05}$			–			6015.7/4816 (1.25)
J0536−6913[n]	$4.89^{+0.50}_{-3.30}$	$0.75^{+0.27}_{-0.07}$	$10.5^{+2.34}_{-8.19}$	$0.11^{+0.02}_{-0.34}$	RD92	4.89	$4.22^{+0.40}_{-2.06}$	$0.08^{+0.03}_{-0.02}$	0.06 ± 0.02	O: $1.68^{+0.92}_{-0.39}$ Ne: $0.59^{+0.31}_{-0.26}$ Mg: $1.51^{+2.35}_{-1.1}$ Si: $7.9^{+17.83}_{-5.20}$	1107.4/1139 (0.97)
J0536−7039[o]	<0.07	$0.27^{+0.14}_{-0.08}$	$3.85^{+52.9}_{-2.60}$	$0.56^{+0.26}_{-0.26}$	RD92	0	$0.73^{+0.07}_{-0.05}$	$7.26^{+500}_{-4.00}$	$0.50^{+0.18}_{-0.08}$	Ne: 0.12(<1.12) Mg: $0.37^{+0.57}_{-0.21}$ Si: 0.37(<0.77) Fe: $1.89^{+0.69}_{-0.79}$	3555.7/3441 (1.03)
J0537−6628	0.56(<1.13)	$0.42^{+0.11}_{-0.09}$	$10.2^{+23.4}_{-6.7}$	$0.60^{+1.30}_{-0.55}$	O: $0.32^{+0.75}_{-0.13}$ Ne: $0.34^{+0.46}_{-0.19}$ Mg: 0.07(<0.31) Fe: $0.26^{+0.23}_{-0.10}$			–			3489.1/2983 (1.17)
J0537−6910[p]	$9.11^{+0.33}_{-0.29}$	4.92 ± 0.35	$0.19^{+0.07}_{-0.06}$	$0.53^{+0.18}_{-0.14}$	RD92			–			3866.8/3452 (1.12)
J0540−6920[q]	$6.85^{+0.18}_{-0.16}$	0.49 ± 0.06	$1.87^{+1.06}_{-0.71}$	$6.03^{+1.32}_{-1.08}$	RD92			–			5528.0/4763 (1.16)
J0540−6944[r]	$11.4^{+1.21}_{-0.90}$	0.20 ± 0.02	CIE	$30.64^{+18.70}_{-16.04}$	RD92			–			1323.4/770 (1.72)
J0541−6659	<0.07	$0.40^{+0.15}_{-0.07}$	$0.36^{+0.19}_{-0.16}$	$0.38^{+0.10}_{-0.16}$	RD92			–			6933.5/5886 (1.18)

Table E.1. continued.

	Component 1					Component 2					χ^2/ν $\left(\chi^2_{\rm red}\right)$
MCSNR	$N_{\rm H\ LMC}$ (10^{21} cm^{-2})	kT (keV)	τ (10^{11} s cm^{-3})	EM (10^{58} cm^{-3})	Abundances	$N_{\rm H\ LMC}$ (10^{21} cm^{-2})	kT (keV)	τ (10^{11} s cm^{-3})	EM (10^{58} cm^{-3})	Abundances	
(1)	(2)	(3)	(4)	(5)	(6)	(7)	(8)	(9)	(10)	(11)	(12)
J0543−6858	$2.09^{+0.65}_{-0.24}$	$1.12^{+0.25}_{-0.51}$	$0.35^{+0.11}_{-0.08}$	$1.14^{+0.76}_{-0.59}$	O: 0.37 ± 0.10 Ne: $0.36^{+0.15}_{-0.12}$ Mg: $0.29^{+0.23}_{-0.16}$ Si: 0.36(<0.98) Fe: $0.32^{+0.16}_{-0.13}$			–			7211.4/6717 (1.07)
J0547−6941	$4.91^{+1.31}_{-1.08}$	1.25 ± 0.18	$2.38^{+0.67}_{-0.30}$	$0.83^{+0.24}_{-0.25}$	O: $0.26^{+0.28}_{-0.15}$ Ne: <0.37 Mg: $0.39^{+0.21}_{-0.14}$ Si: $0.71^{+0.33}_{-0.27}$ Fe: 2.30 ± 0.70			–			3451.2/3196 (1.08)
J0547−6943[s]	$3.73^{+1.15}_{-0.72}$	$0.27^{+0.26}_{-0.05}$	493(>5.32)	$3.67^{+4.78}_{-2.72}$	O: $0.22^{+0.40}_{-0.09}$ Ne: $0.27^{+0.33}_{-0.22}$ Mg: $0.76^{+0.45}_{-0.28}$ Si: $0.58^{+0.35}_{-0.24}$ S: $0.33^{+0.34}_{-0.31}$ Fe: $0.58^{+0.26}_{-0.19}$	3.73	$2.16^{+0.45}_{-0.27}$	$2.33^{+1.23}_{-0.66}$	$0.89^{+0.22}_{-0.25}$	–	4468.2/4356 (1.03)
J0547−7025 †	$3.04^{+0.37}_{-0.35}$	$0.31^{+0.01}_{-0.05}$	$3.12^{+11.7}_{-3.66}$	$4.72^{+3.14}_{-1.81}$	RD92	3.04	$0.80^{+0.13}_{-0.10}$	$1.18^{+0.90}_{-0.18}$	$1.65^{+0.35}_{-0.52}$	O: <0.08 Ne: 0.32 ± 0.01 Mg: 0.07(<0.12) Si: 0.28 ± 0.25 S: $1.10^{+0.50}_{-0.57}$ Fe: $0.92^{+0.23}_{-0.19}$	2949.1/2559 (1.15)

Table E.2. X-ray spectral results for bright LMC SNRs.

Component	$N_{\rm H\ LMC}$ (10^{21} cm^{-2})	kT (keV)	τ (10^{11} s cm^{-3})	EM (10^{58} cm^{-3})	O	Ne	Mg	Si	S	Ar	Ca	Fe
DEM L71 – MCSNR J0505−6753: χ^2/ν = 3300.5/1784 (1.85)												
CSM/ISM	0.28 ± 0.001	0.46 ± 0.01	$2.59^{+0.03}_{-0.02}$	$38.2^{+2.88}_{-0.17}$	0.26 ± 0.001	0.40 ± 0.001	$0.49^{+0.01}_{-0.02}$	0	0	–	–	0
Ejecta $_{\rm cool}$		$0.42^{+0.004}_{-0.009}$	$3.56^{+0.98}_{-0.40}$	$11.3^{+0.12}_{-0.14}$	0	0	0	$1.03^{+0.05}_{-0.03}$	$1.27^{+0.09}_{-0.07}$	0	0	1.21± 0.001
Ejecta $_{\rm hot}$		$0.88^{+0.007}_{-0.001}$	$1.83^{+0.06}_{-0.04}$	$7.30^{+0.36}_{-0.63}$	0	0	0			0	0	
N103B – MCSNR J0509−6844: χ^2/ν = 694.2/583 (1.19)												
CSM/ISM	$3.09^{+0.20}_{-0.11}$	$0.33^{+0.03}_{-0.10}$	$34.9^{+137.5}_{-19.7}$	$40.73^{+4.27}_{-4.68}$	–	–	–	–	–	–	–	–
Ejecta $_{\rm cool}$		0.71 ± 0.02	>41.4	$25.9^{+1.47}_{-2.84}$	<0.25	$1.71^{+0.49}_{-0.32}$	$0.33^{+0.10}_{-0.14}$	$2.84^{+0.56}_{-0.30}$	$3.48^{+0.33}_{-0.28}$	$5.26^{+1.0}_{-0.59}$	$9.51^{+2.43}_{-2.05}$	$1.10^{+0.36}_{-0.14}$
Ejecta $_{\rm hot}$		$1.62^{+0.10}_{-0.16}$	$8.59^{+4.27}_{-2.64}$	$9.95^{+1.50}_{-0.57}$								
N132D – MCSNR J0525−6938: χ^2/ν = 1288.4/1116 (1.15)												
CSM/ISM	0.74 ± 0.03	$0.64^{+0.02}_{-0.01}$	$5.97^{+0.44}_{-0.35}$	$358.6^{+4.78}_{-3.33}$	$0.05^{+0.02}_{-0.01}$	0.46 ± 0.02	0.19±0.01	0.39 ± 0.03	–	–	–	0.28± 0.01
O-rich		$1.46^{+0.04}_{-0.02}$	$10.0^{+1.13}_{-4.030}$	$33.2^{+10.1}_{-1.81}$	$9.03^{+1.44}_{-3.48}$	<0.25	$2.59^{+0.19}_{-0.17}$	$1.37^{+0.19}_{-0.15}$	$1.03^{+0.11}_{-0.10}$	–	–	$0.15^{+0.05}_{-0.02}$
Si-S-Fe		$5.12^{+0.93}_{-0.72}$	500	$7.84^{+1.33}_{-0.86}$	0	0	0	0	0	$5.29^{+4.05}_{-3.26}$	2.20(< 4.86)	1.0
0509−67.5 – MCSNR J0509−6731: χ^2/ν = 871.1/419 (2.08)												
CSM/ISM	1.64 ± 0.07	$0.27^{+0.09}_{-0.01}$	$9.44^{+1.69}_{-3.02}$	$6.26^{+4.42}_{-2.70}$	$1.14^{+1.58}_{-0.03}$	$2.37^{+0.06}_{-0.05}$	$2.45^{+0.29}_{-0.56}$	0	0	0	0	$2.84^{+5.78}_{-0.15}$
Fe $_{\rm cool}$		$1.42^{+0.09}_{-0.05}$	0.08 ± 0.01	$10.5^{+2.20}_{-4.46}$	0	0	0	0	0	0	0	pure
Fe $_{\rm hot}$-Ca		$11.7^{+9.9}_{-1.5}$	$11.4^{+7.6}_{-4.4}$	$1.75^{+0.29}_{-0.24}$	0	0	0	0	0	0	$4.51^{+2.05}_{-1.64}$	1.0
Si-S-Ar		$1.18^{+0.11}_{-0.12}$	$0.23^{+0.014}_{-0.003}$	$57.3^{+3.5}_{-3.0}$	0	0	0	1.0	$3.28^{+0.19}_{-0.11}$	$3.38^{+0.25}_{-0.10}$	0	0
0519−69.0 – MCSNR J0519−6902: χ^2/ν = 5971.7/2438 (2.45)												
CSM/ISM	0.96 ± 0.04	$0.60^{+0.02}_{-0.01}$	$29.4^{+29.6}_{-8.9}$	$22.5^{+0.53}_{-0.90}$	–	–	$0.35^{+0.03}_{-0.01}$	–	–	–	–	–
Fe $_{\rm cool}$		$1.37^{+0.01}_{-0.02}$	0.88±0.02	$10.0^{+0.30}_{-0.23}$	0	0	0	0	0	0	0	pure
Fe $_{\rm hot}$		8.12	3.60	8.61	0	0	0	0	0	0	0	pure
Si-S		$3.43^{+0.50}_{-0.45}$	$1.12^{+0.12}_{-0.06}$	$10.6^{+0.67}_{-30}$	0	0	0	1.0	1.26 ± 0.06	0	0	0
Ar-Ca		4.42 ± 1.20	$2.03^{+0.51}_{-0.46}$	$15.8^{+4.6}_{-5.5}$	0	0	0	0	0	1.0	$1.33^{+0.25}_{-0.18}$	0
O		$4.32^{+1.47}_{-4.03}$	$0.04^{+0.17}_{-0.02}$	$0.10^{+0.08}_{-0.03}$	pure	0	0	0	0	0	0	0

Notes. Details of the spectral models used are given in Sect. 5.2.

Table E.3. Spectral results, abundances, fluxes, and Fe K line properties of SNR 1987A.

Epoch	Age	low-kT component		1.15 keV component	high-kT component		ionisation age
		kT	EM	EM	kT	EM	
	(days)	keV	(10^{58} cm^{-3})	(10^{58} cm^{-3})	(keV)	(10^{58} cm^{-3})	(10^{11} s cm^{-3})
2007 Jan.	7267	0.35 ± 0.01	$35.69^{+2.34}_{-2.07}$	$7.31^{+0.17}_{-0.27}$	$13.89^{+7.11}_{-4.80}$	$0.55^{+0.05}_{-0.03}$	$4.42^{+0.41}_{-0.56}$
2008 Jan.	7626	$0.36^{+0.02}_{-0.01}$	$42.63^{+4.09}_{-3.51}$	$7.80^{+0.75}_{-0.37}$	$5.82^{+4.69}_{-0.52}$	$1.06^{+0.15}_{-0.20}$	$4.60^{+0.57}_{-0.53}$
2009 Jan.	8013	0.37 ± 0.01	$49.66^{+3.82}_{-4.57}$	$11.89^{+0.42}_{-1.24}$	$10.86^{+3.64}_{-4.71}$	$0.90^{+0.02}_{-0.05}$	$5.27^{+0.39}_{-0.67}$
2009 Dec.	8328	0.40 ± 0.01	$47.29^{+2.64}_{-4.37}$	$12.97^{+0.40}_{-1.14}$	$5.98^{+1.47}_{-1.14}$	$1.40^{+0.34}_{-0.19}$	$4.77^{+0.26}_{-0.25}$
2010 Dec.	8693	$0.42^{+0.02}_{-0.01}$	$48.13^{+2.03}_{-1.73}$	$13.40^{+1.28}_{-0.90}$	$3.80^{+0.99}_{-0.49}$	$2.43^{+0.34}_{-0.53}$	$4.98^{+0.71}_{-0.43}$
2011 Dec.	9048	$0.44^{+0.02}_{-0.01}$	$45.72^{+1.66}_{-1.38}$	$15.92^{1.10+}_{-0.63}$	$5.66^{+0.41}_{-0.70}$	$2.20^{+0.27}_{-0.34}$	$4.84^{+0.33}_{-0.37}$
2012 Dec.	9423	$0.44^{+0.02}_{-0.01}$	$44.56^{+0.99}_{-2.41}$	$19.90^{+0.44}_{-1.26}$	$7.66^{+1.81}_{-0.86}$	$1.95^{+0.15}_{-0.07}$	$5.76^{+0.54}_{-0.26}$

	N	O	Ne	Mg	Si	S	Fe
	1.35 ± 0.06	0.08 ± 0.01	0.29 ± 0.01	0.26 ± 0.01	0.51±0.01	0.48 ± 0.02	0.24 ± 0.01

Epoch	Age	Flux (0.5–2 keV)	Flux (3–10 keV)	ΔF_X	E_{line}	σ-width	Flux	EW
	(days)	(10^{-13} erg s^{-1} cm^{-2})		(%)	(keV)	(eV)	(10^{-6} ph cm^{-2} s^{-1})	(eV)
2007 Jan.	7267	$33.51^{+0.46}_{-0.49}$	$4.09^{+0.86}_{-1.71}$	–	–	–	–	–
2008 Jan.	7626	$43.34^{+0.56}_{-0.57}$	$5.22^{+0.67}_{-1.54}$	29.8	$6.58^{+0.05}_{-0.07}$	46 (<146)	$1.07^{+0.57}_{-0.46}$	174
2009 Jan.	8013	$52.77^{+0.71}_{-0.64}$	$6.31^{+0.76}_{-1.86}$	20.5	$6.55^{+0.15}_{-0.14}$	125 (<433)	$0.94^{+1.50}_{-0.65}$	169
2009 Dec.	8328	$59.04^{+0.66}_{-0.69}$	$7.42^{+0.89}_{-2.37}$	13.8	$6.63^{+0.11}_{-0.09}$	229 (<424)	$2.64^{+1.69}_{-1.78}$	432
2010 Dec.	8693	$65.90^{+1.08}_{-1.17}$	$8.16^{+0.96}_{-2.24}$	11.6	$6.61^{+0.06}_{-0.06}$	105 (<227)	$2.51^{+1.39}_{-0.99}$	344
2011 Dec.	9048	$70.69^{+0.71}_{-0.76}$	$11.31^{+1.08}_{-2.16}$	7.5	$6.61^{+0.06}_{-0.06}$	83 (<178)	$2.08^{+1.01}_{-0.86}$	238
2012 Dec.	9423	$74.60^{+0.79}_{-0.87}$	$11.65^{+1.22}_{-2.33}$	5.4	$6.78^{+0.06}_{-0.05}$	84 (<155)	$2.11^{+0.97}_{-0.85}$	230

Notes. *Top panel*: best-fit values and 90% C. L. uncertainties for the parameters of the three-components spectral model described in Sect. 5.3, in spectra obtained from 2007 to 2012. *Middle panel*: best-fit abundances relative to the solar values as listed in Wilms et al. (2000). *Bottom panel*: fluxes and Fe K line properties. Columns (3) and (4) list the soft and hard X-ray fluxes with 3σ errors (99.73% C.L.). Column (5) gives the increase rate of the flux (in %) since previous measurement, normalised to one year. Columns (6) to (9) give the central energy, σ-width, total photon flux and equivalent width (EW) of the Gaussian used to characterise the Fe K feature in the spectra of SNR 1987A (with 90% C. L. uncertainties).

Appendix F: X-ray images, spectral extraction regions, and SFH for all LMC SNRs

This Appendix presents, for each SNR, an X-ray image (top), the regions used for spectral analysis (middle), and the SFH of the cell including the remnant (bottom panel). The images are using the (0.3–0.7 keV), medium (0.7–1.1 keV), and hard (1.1–4.2 keV) bands as red, green, and blue components, respectively, and have been adaptively smoothed (see Sect. 2.2. The white bars indicate the scale of 1′. North is up and east is left. A linear scale is used to display the pixel values, but the cut levels are adapted for each SNR. The extraction regions used for spectral analysis are shown for pn, MOS1, and MOS2 detectors (left to right), as in Fig. 3. The star formation history plots are shown as in Fig. 8. For MCSNR J0509−6844, J0509−6731, and J0509−6902, which are highly unresolved with *XMM-Newton*, we show *Chandra* images, using processed data obtained from the *Chandra* SNR catalogue.

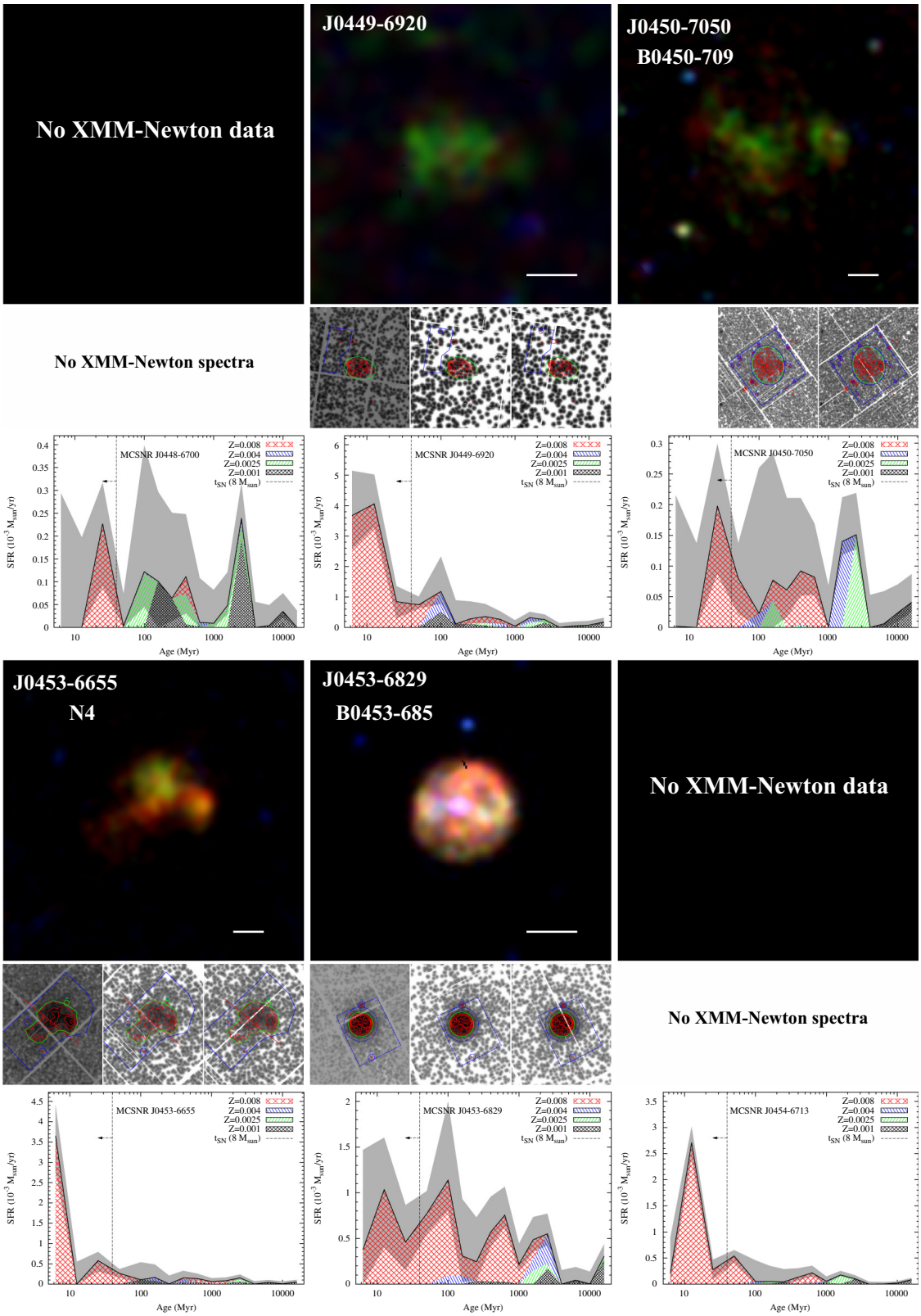

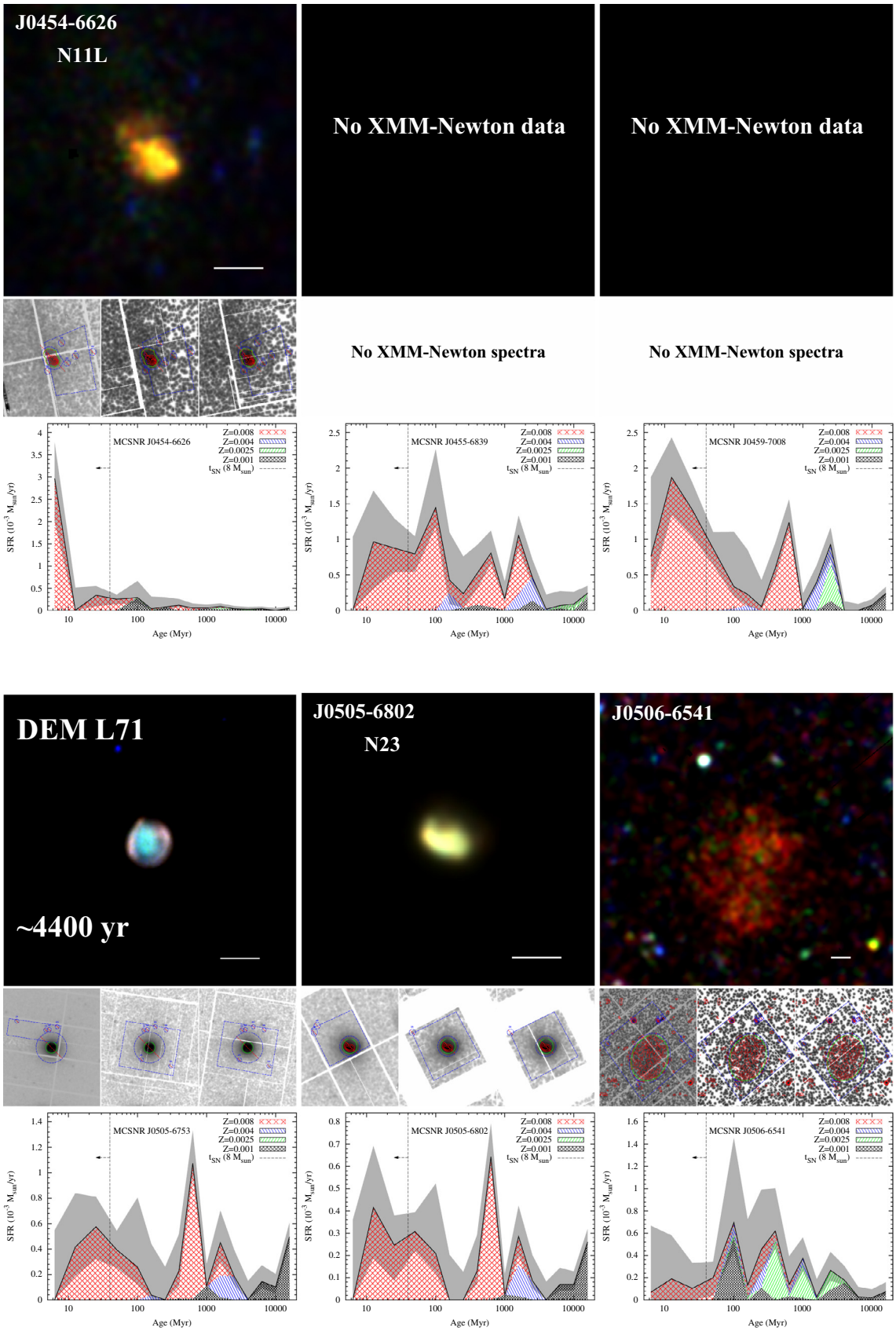
J0454-6626
N11L
No XMM-Newton data
No XMM-Newton data
No XMM-Newton spectra
No XMM-Newton spectra
MCSNR J0454-6626
MCSNR J0455-6839
MCSNR J0459-7008
DEM L71
~4400 yr
J0505-6802
N23
J0506-6541
MCSNR J0505-6753
MCSNR J0505-6802
MCSNR J0506-6541
Z=0.008
Z=0.004
Z=0.0025
Z=0.001
t_SN (8 M_sun)
SFR (10^-3 M_sun/yr)
Age (Myr)

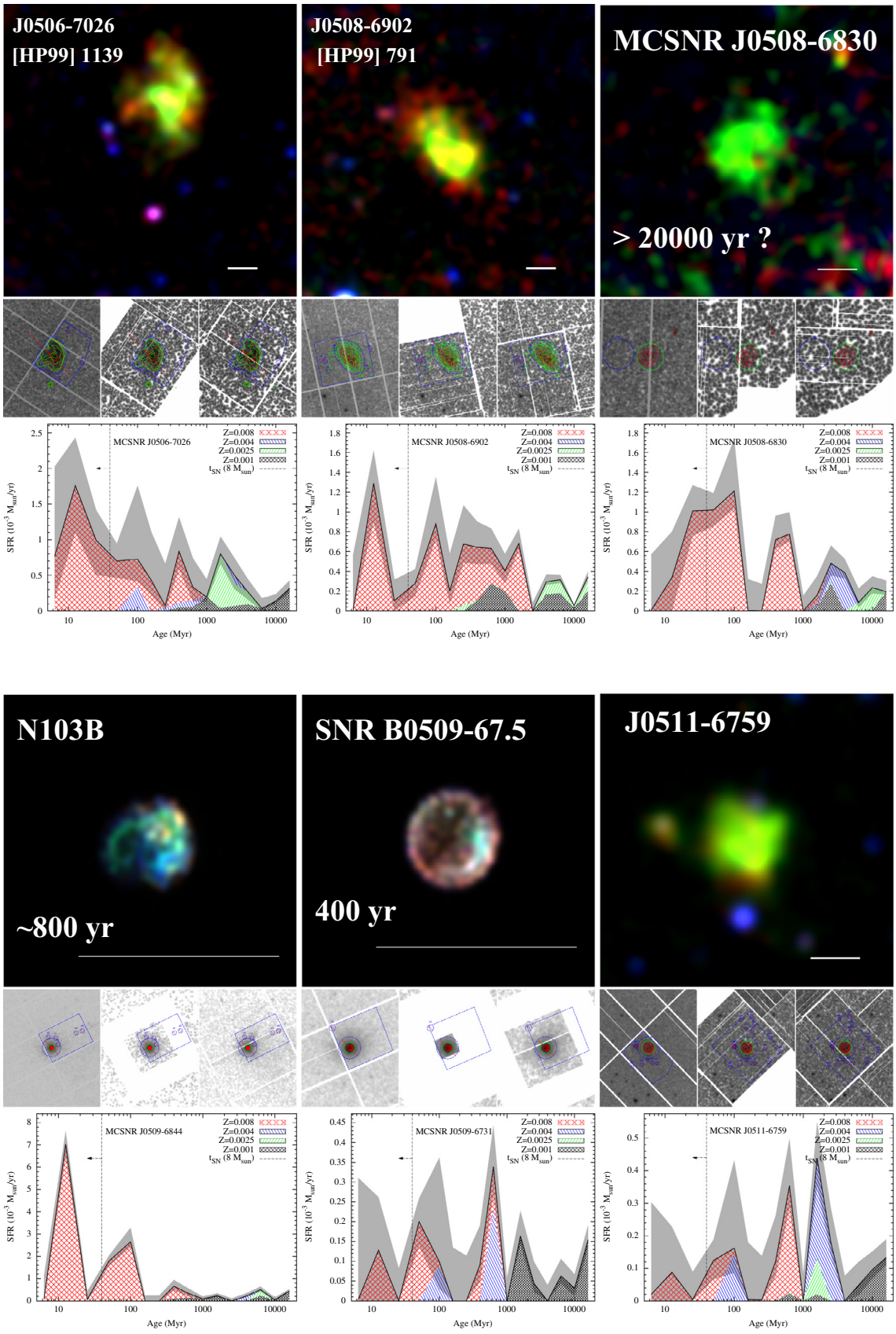
J0506-7026
[HP99] 1139
J0508-6902
[HP99] 791
MCSNR J0508-6830
> 20000 yr ?
MCSNR J0506-7026
MCSNR J0508-6902
MCSNR J0508-6830
N103B
~800 yr
SNR B0509-67.5
400 yr
J0511-6759
MCSNR J0509-6844
MCSNR J0509-6731
MCSNR J0511-6759
Z=0.008
Z=0.004
Z=0.0025
Z=0.001
t_SN (8 M_sun)
SFR (10^-3 M_sun/yr)
Age (Myr)

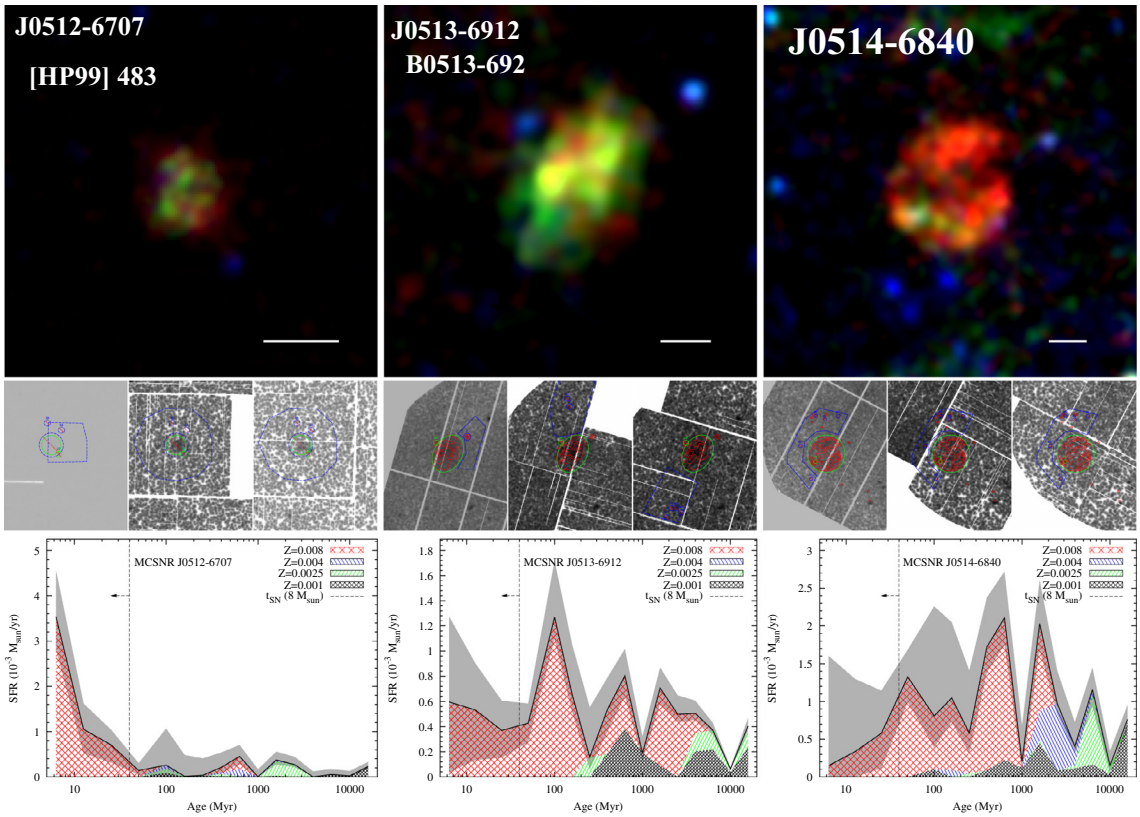
J0512-6707
[HP99] 483
J0513-6912
B0513-692
J0514-6840
MCSNR J0512-6707
MCSNR J0513-6912
MCSNR J0514-6840
Z=0.008
Z=0.004
Z=0.0025
Z=0.001
SFR (10^{-3} M_{sun}/yr)
Age (Myr)

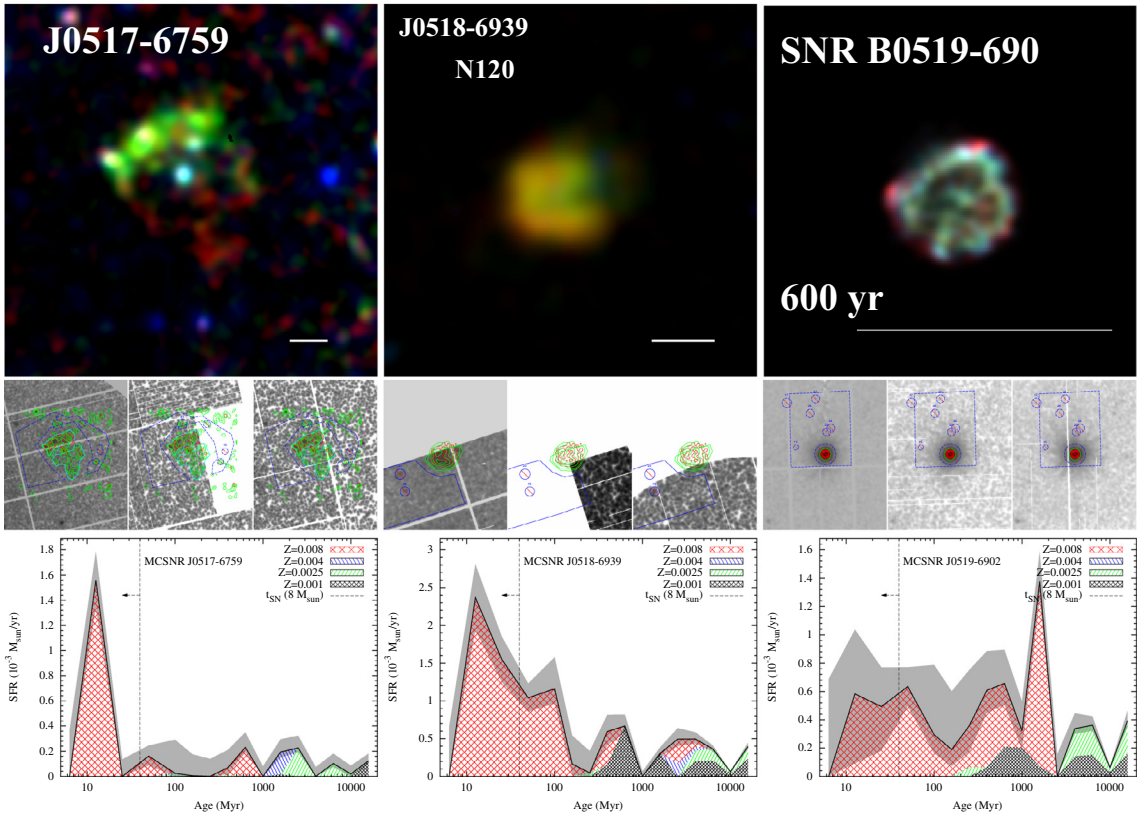
J0517-6759
J0518-6939
N120
SNR B0519-690
600 yr
MCSNR J0517-6759
MCSNR J0518-6939
MCSNR J0519-6902
Z=0.008
Z=0.004
Z=0.0025
Z=0.001
SFR (10^{-3} M_{sun}/yr)
Age (Myr)

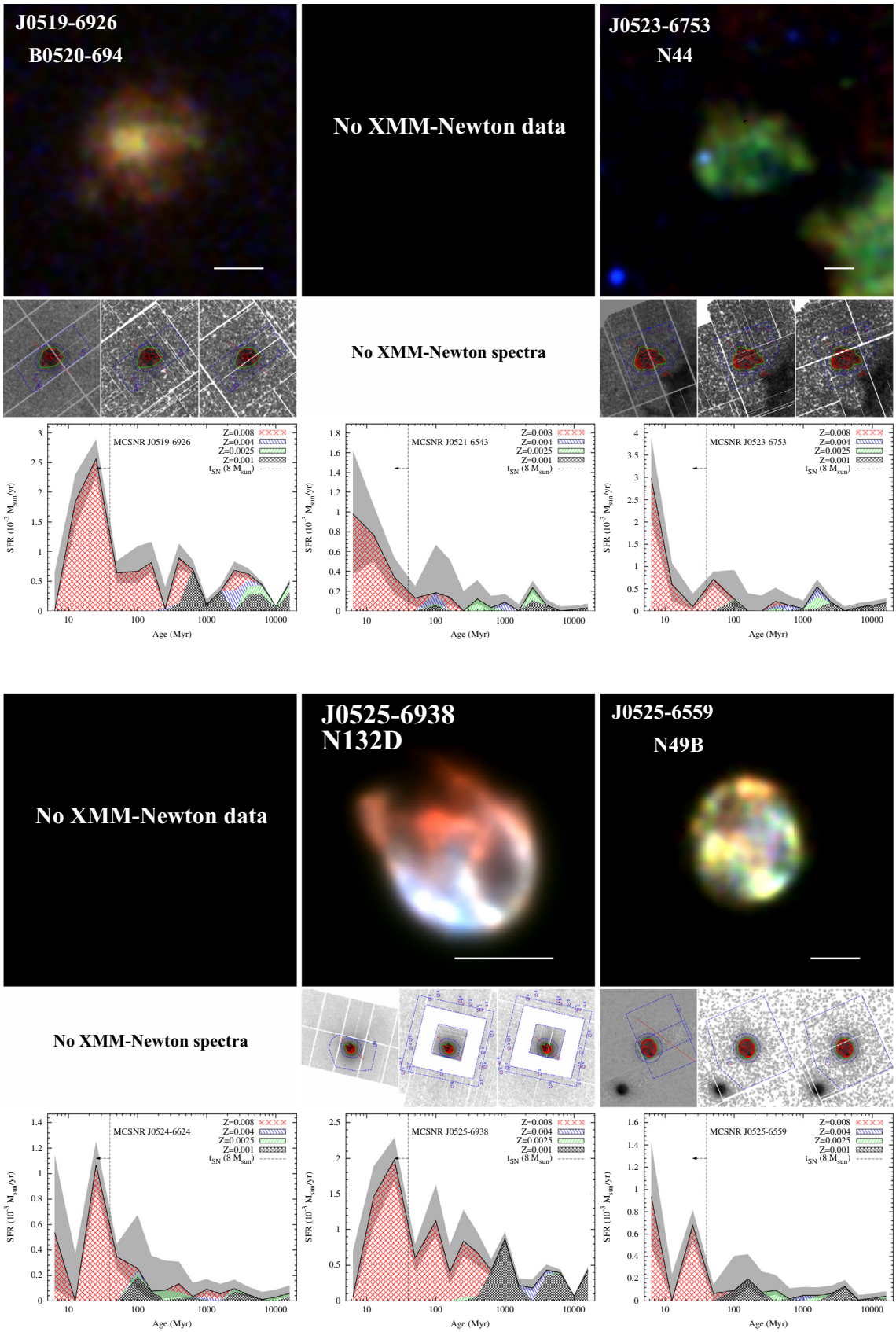
J0519-6926
B0520-694
No XMM-Newton data
J0523-6753
N44
No XMM-Newton spectra
MCSNR J0519-6926
MCSNR J0521-6543
MCSNR J0523-6753
Z=0.008
Z=0.004
Z=0.0025
Z=0.001
t_SN (8 M_sun)
SFR (10^-3 M_sun/yr)
Age (Myr)
No XMM-Newton data
J0525-6938
N132D
J0525-6559
N49B
No XMM-Newton spectra
MCSNR J0524-6624
MCSNR J0525-6938
MCSNR J0525-6559

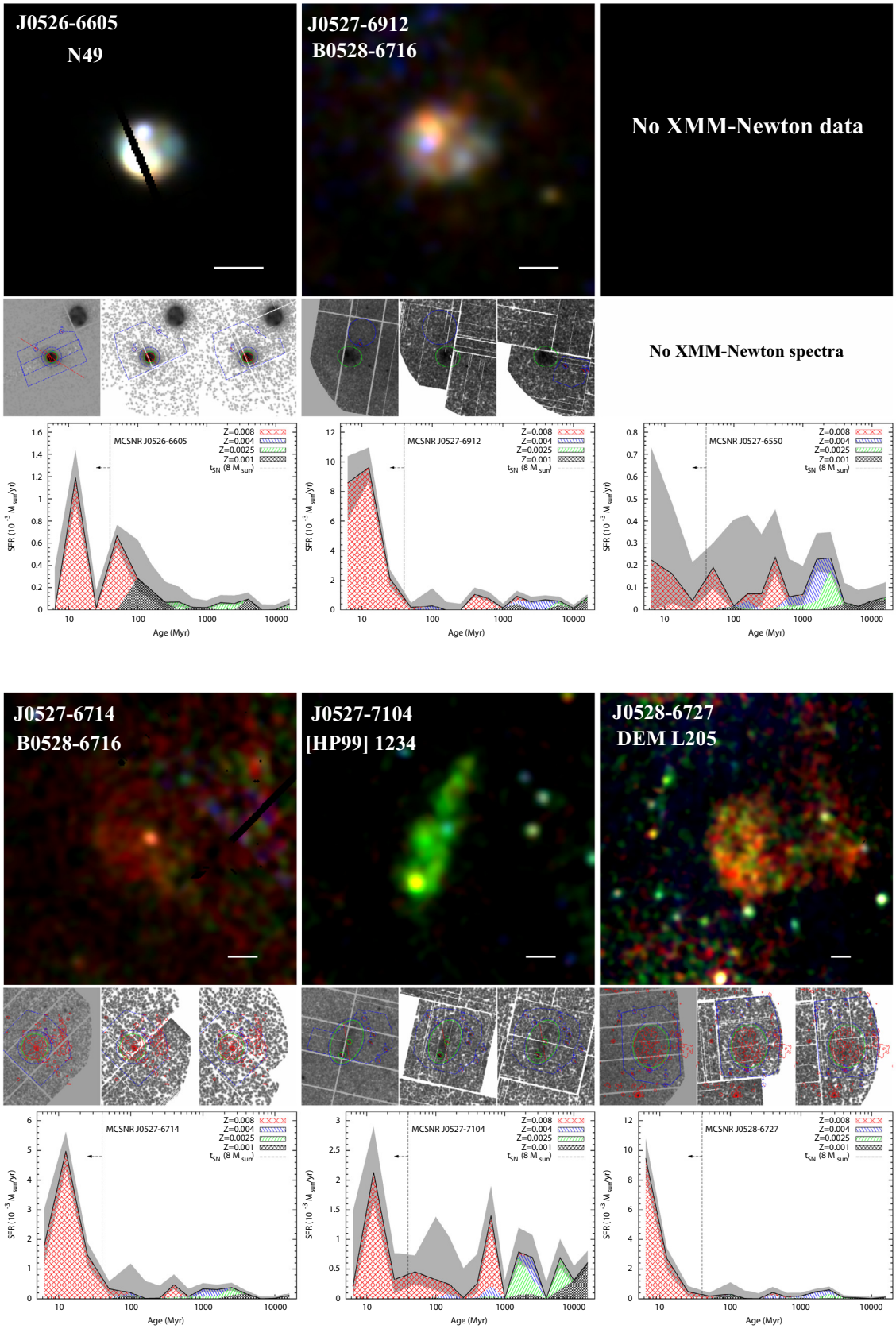
J0526-6605
N49
J0527-6912
B0528-6716
No XMM-Newton data
No XMM-Newton spectra
MCSNR J0526-6605
MCSNR J0527-6912
MCSNR J0527-6550
J0527-6714
B0528-6716
J0527-7104
[HP99] 1234
J0528-6727
DEM L205
MCSNR J0527-6714
MCSNR J0527-7104
MCSNR J0528-6727
Z=0.008
Z=0.004
Z=0.0025
Z=0.001
t_SN (8 M_sun)
SFR (10^-3 M_sun/yr)
Age (Myr)

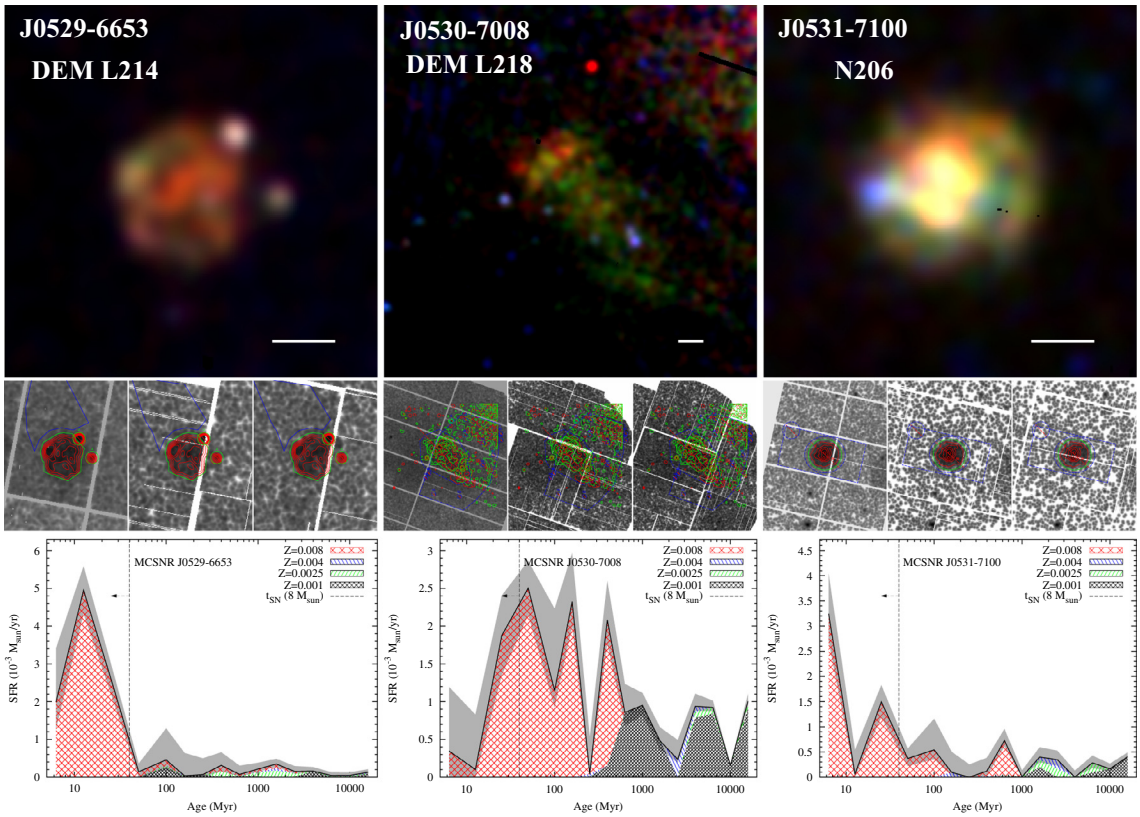
J0529-6653
DEM L214
J0530-7008
DEM L218
J0531-7100
N206
MCSNR J0529-6653
MCSNR J0530-7008
MCSNR J0531-7100
Z=0.008
Z=0.004
Z=0.0025
Z=0.001
t_SN (8 M_sun)
SFR (10^-3 M_sun/yr)
Age (Myr)

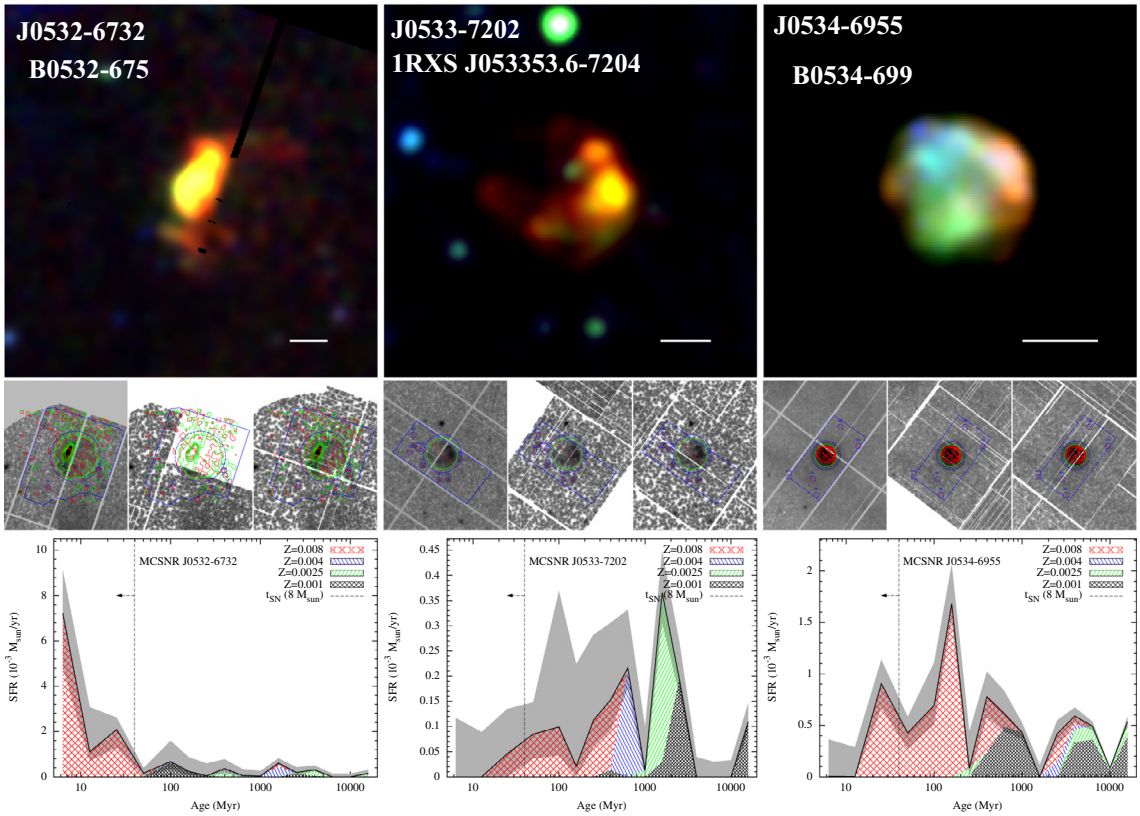
J0532-6732
B0532-675
J0533-7202
1RXS J053353.6-7204
J0534-6955
B0534-699
MCSNR J0532-6732
MCSNR J0533-7202
MCSNR J0534-6955
Z=0.008
Z=0.004
Z=0.0025
Z=0.001
t_SN (8 M_sun)
SFR (10^-3 M_sun/yr)
Age (Myr)

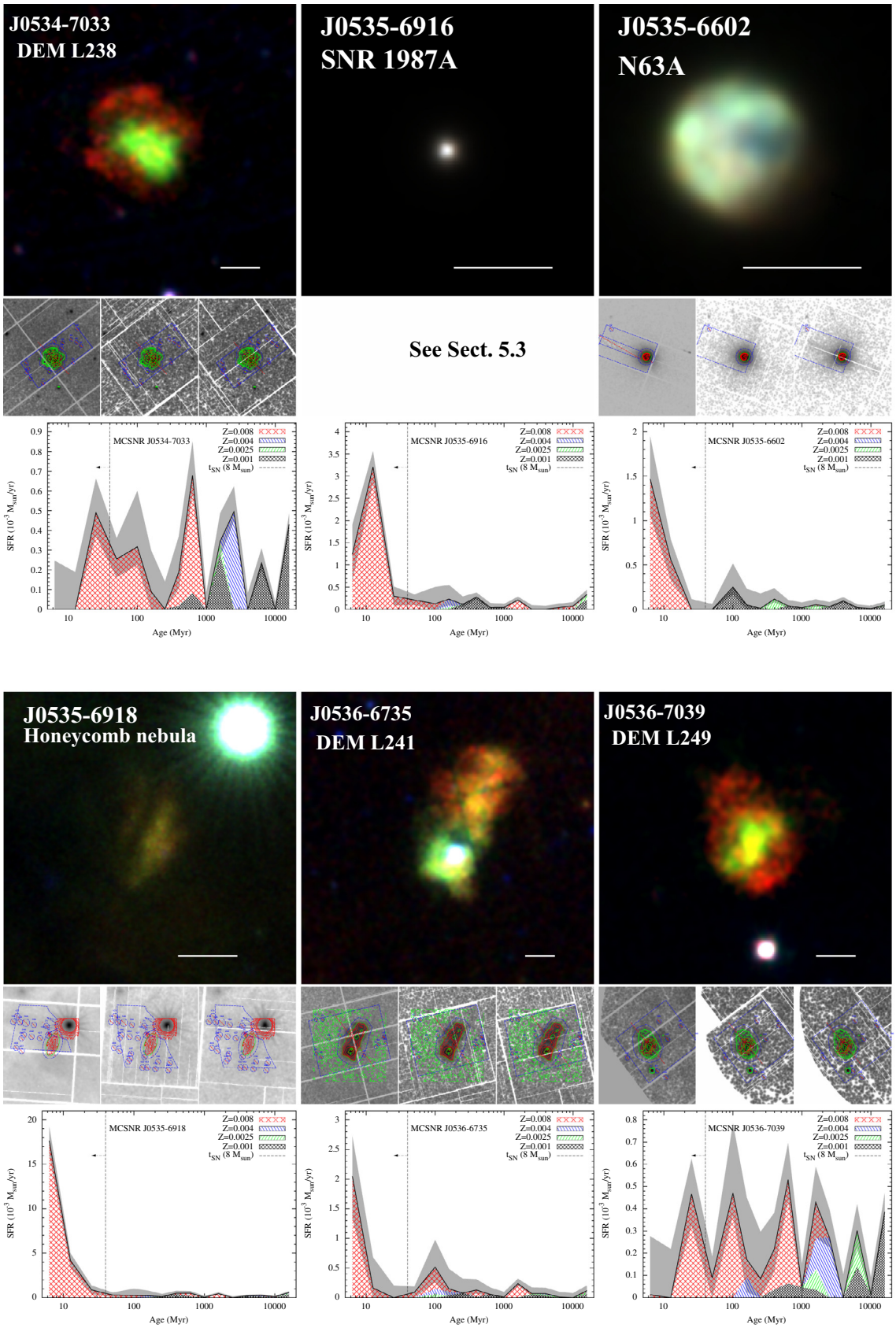
J0534-7033
DEM L238
J0535-6916
SNR 1987A
J0535-6602
N63A
See Sect. 5.3
MCSNR J0534-7033
MCSNR J0535-6916
MCSNR J0535-6602
Z=0.008
Z=0.004
Z=0.0025
Z=0.001
t_SN (8 M_sun)
SFR (10^-3 M_sun/yr)
Age (Myr)
J0535-6918
Honeycomb nebula
J0536-6735
DEM L241
J0536-7039
DEM L249
MCSNR J0535-6918
MCSNR J0536-6735
MCSNR J0536-7039

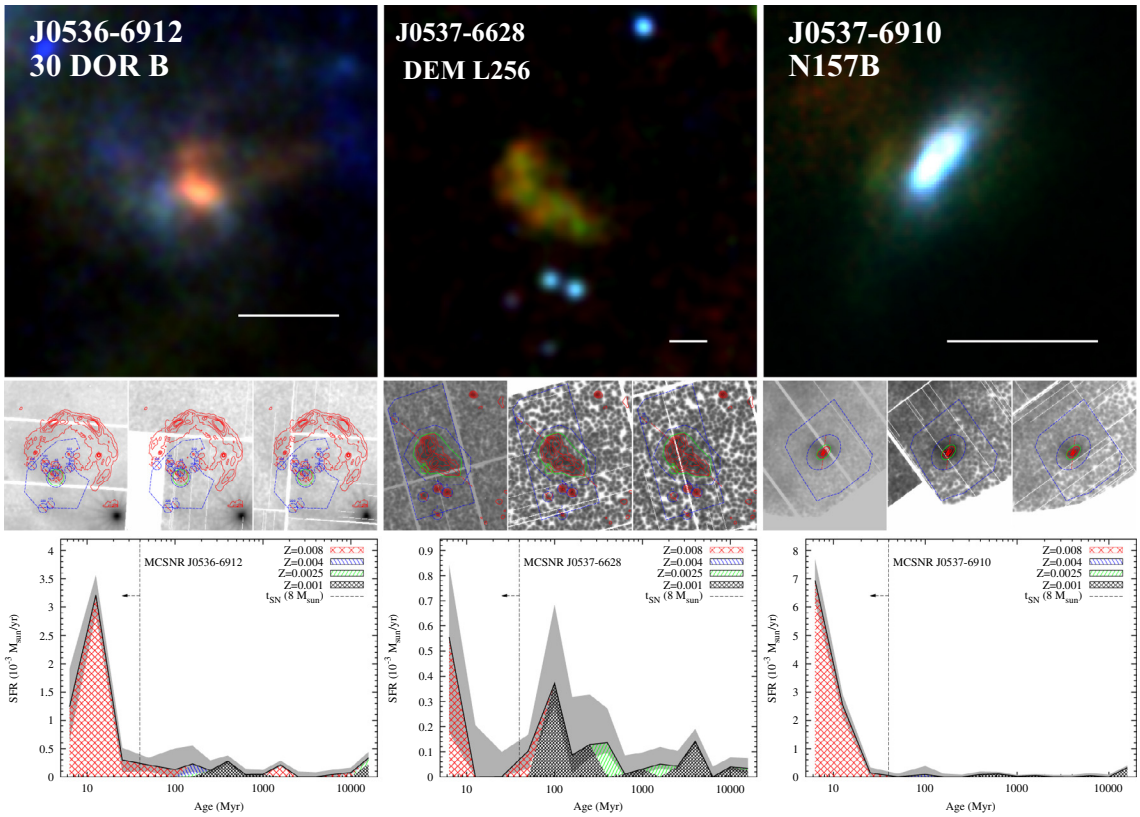
J0536-6912
30 DOR B
J0537-6628
DEM L256
J0537-6910
N157B
MCSNR J0536-6912
MCSNR J0537-6628
MCSNR J0537-6910
Z=0.008
Z=0.004
Z=0.0025
Z=0.001
t_SN (8 M_sun)
SFR (10^-3 M_sun/yr)
Age (Myr)

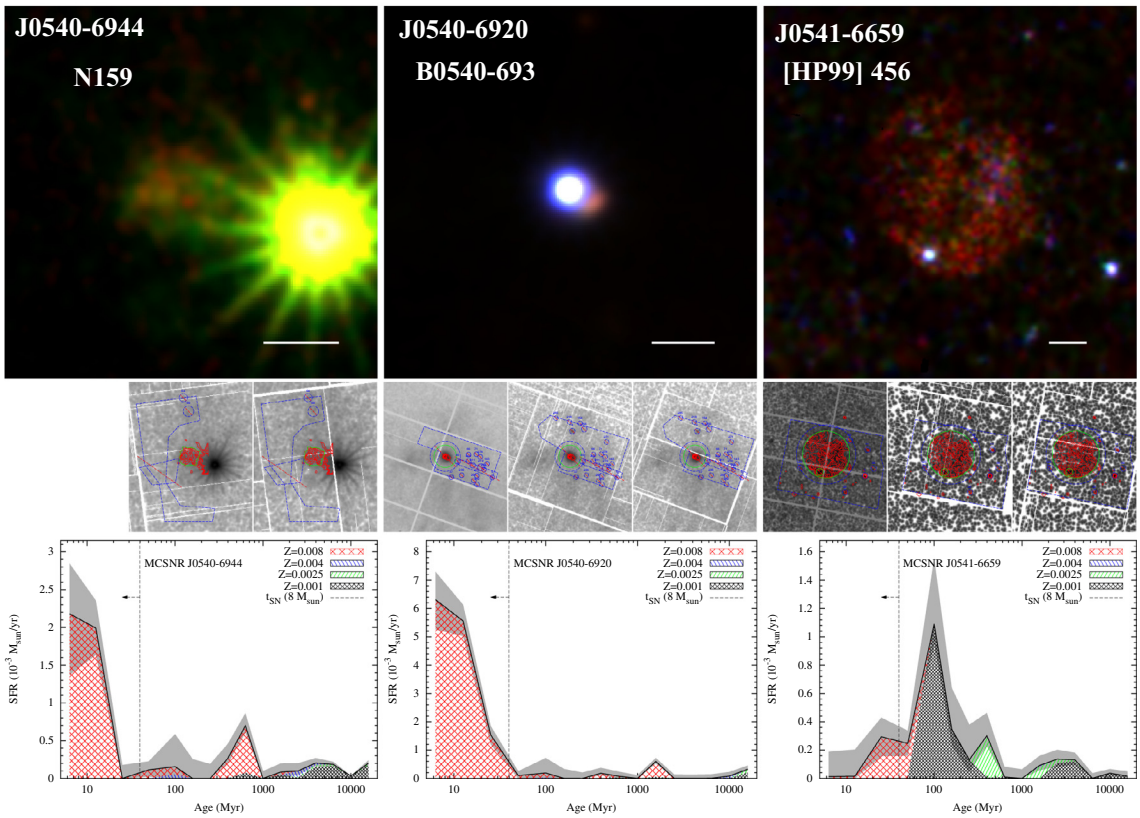
J0540-6944
N159
J0540-6920
B0540-693
J0541-6659
[HP99] 456
MCSNR J0540-6944
MCSNR J0540-6920
MCSNR J0541-6659
Z=0.008
Z=0.004
Z=0.0025
Z=0.001
t_SN (8 M_sun)
SFR (10^-3 M_sun/yr)
Age (Myr)

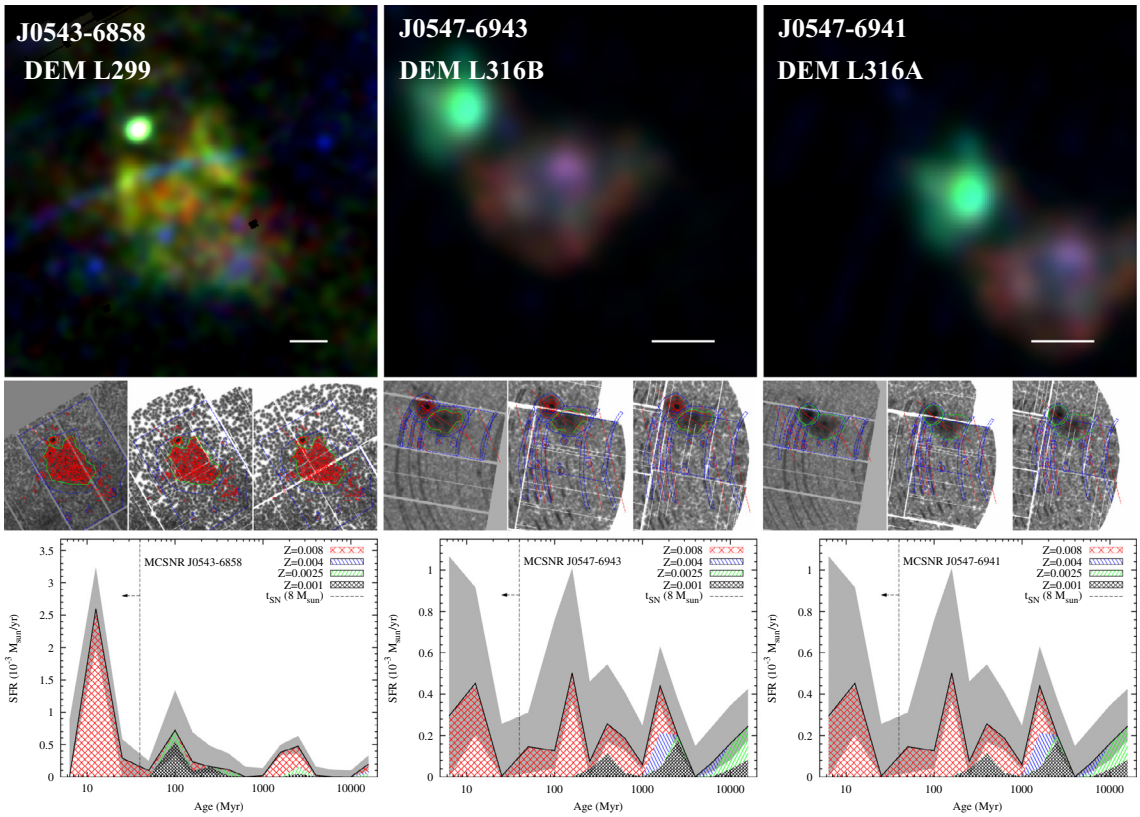
J0543-6858
DEM L299
J0547-6943
DEM L316B
J0547-6941
DEM L316A
MCSNR J0543-6858
MCSNR J0547-6943
MCSNR J0547-6941
Z=0.008
Z=0.004
Z=0.0025
Z=0.001
t_SN (8 M_sun)
SFR (10^-3 M_sun/yr)
Age (Myr)

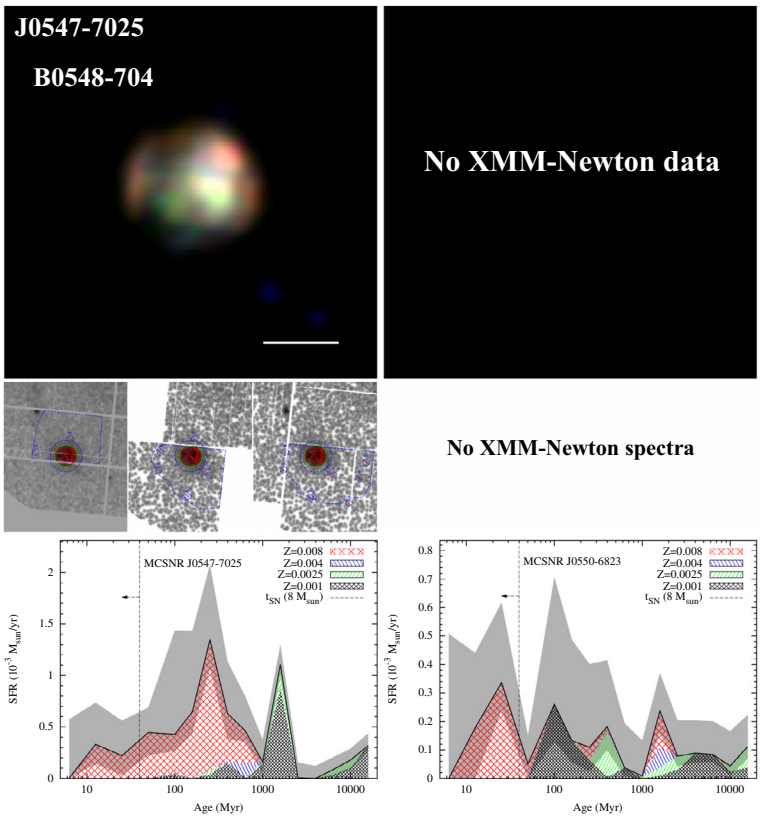
J0547-7025
B0548-704
No XMM-Newton data
No XMM-Newton spectra
MCSNR J0547-7025
MCSNR J0550-6823
Z=0.008
Z=0.004
Z=0.0025
Z=0.001
t_SN (8 M_sun)
SFR (10^-3 M_sun/yr)
Age (Myr)